REPORT DOCUMENTATION PAGE

AFRL-SR-AR-TR-04-

0387

1. REPORT DATE *(DD-MM-YYYY)* 072004	2. REPORT TYPE RINAL REPORT	3. DATES COVERED *(From - To)* 15 Feb 2000 - 14 Feb 2003

4. TITLE AND SUBTITLE
High Temperature Studies of La-Monazite

5a. CONTRACT NUMBER

5b. GRANT NUMBER
F49620-00-C-0010

5c. PROGRAM ELEMENT NUMBER

6. AUTHOR(S)
David Marshall, Janet B. Davis

5d. PROJECT NUMBER

5e. TASK NUMBER

5f. WORK UNIT NUMBER

7. PERFORMING ORGANIZATION NAME(S) AND ADDRESS(ES)
Rockwell Scientific Company
1049 Camino Dos Rios
Thousand Oaks CA 91360

8. PERFORMING ORGANIZATION REPORT NUMBER

9. SPONSORING/MONITORING AGENCY NAME(S) AND ADDRESS(ES)
USAF/AFRL
AFOSR
801 N. Randolph Street
Arlington VA 22203

10. SPONSOR/MONITOR'S ACRONYM(S)
AFOSR

11. SPONSOR/MONITOR'S REPORT NUMBER(S)

12. DISTRIBUTION/AVAILABILITY STATEMENT

Distribution Statement A. Approved for public release; distribution is unlimited

20040804 055

13. SUPPLEMENTARY NOTES

14. ABSTRACT
This report summarizes results from a 3-year research effort aimed at gaining a basic understanding of high-temperature properties of LaPO4, with a view to its application in high-temperature structural composites. Previous studies at Rockwell and the Air Force established that LaPO4 has a unique set of properties that make it suitable as a weakly bonded interphase material that enables damage tolerance by decoupling damage in the matrix and the reinforcing fibers. However, there was previously very little information on the fundamental high temperature properties of LaPO4, such as environmental stability, sintering, grain growth, mechanical and dielectric properties. Such studies require high purity powders that have only recently been produced at Rockwell. Using these materials, measurements have been made of the following properties: stability in various high temperature environments required for Air Force application, including water-containing environments typical of combustion, vacuum, and reducing environments; high-temperature creep, hardness, toughness, and sliding; low-temperature debonding, deformation, and sliding mechanisms; and dielectric properties. A preliminary assessment is made of the potential for developing directionally solidified eutectic oxide systems containing LaPO4 for toughening.

15. SUBJECT TERMS

16. SECURITY CLASSIFICATION OF:			17. LIMITATION OF ABSTRACT	18. NUMBER OF PAGES	19a. NAME OF RESPONSIBLE PERSON
a. REPORT	b. ABSTRACT	c. THIS PAGE			
U	U	U	UU	102	19b. TELEPHONE NUMBER *(Include area code)*

Standard Form 298 (Rev. 8/98)
Prescribed by ANSI Std. Z39.18

7-29-04

HIGH TEMPERATURE STUDIES of La-MONAZITE

Contract Number: F49620-00-C-0010
Final Report

prepared for

Dr. J. Fuller
Air Force Office of Scientific Research

Prepared by

David B. Marshall
Janet B. Davis

Rockwell Scientific Company
1049 Camino Dos Rios
Thousand Oaks, CA 91360

July 2004

ABSTRACT

This report summarizes results from a 3-year research effort aimed at gaining a basic understanding of high-temperature properties of $LaPO_4$, with a view to its application in high-temperature structural composites. Previous studies at Rockwell and the Air Force established that $LaPO_4$ has a unique set of properties that make it suitable as a weakly bonded interphase material that enables damage tolerance by decoupling damage in the matrix and the reinforcing fibers. However, there was previously very little information on the fundamental high temperature properties of $LaPO_4$, such as environmental stability, sintering, grain growth, mechanical and dielectric properties. Such studies require high purity powders that have only recently been produced at Rockwell. Using these materials, measurements have been made of the following properties: stability in various high temperature environments required for Air Force applications, including water-containing environments typical of combustion, vacuum, and reducing environments; high-temperature creep, hardness, toughness, and sliding; low-temperature debonding, deformation, and sliding mechanisms; and dielectric properties. A preliminary assessment is made of the potential for developing directionally solidified eutectic oxide systems containing $LaPO_4$ for toughening.

1

Table of Contents

1.0 SUMMARY

There is a need in the Air Force for ceramic composites with long-term stability in severe high temperature environments containing oxygen, water vapor, and fuel impurities typical of turbine engines. Until recently, the development of thermodynamically stable oxide composites was prevented by the lack of a key ingredient; a suitable weakly bonded interphase material, to impart some degree of damage tolerance by decoupling damage in the matrix and the reinforcing fibers or other phases. During the last five years several suitable interphase materials have been identified, the most refractory being $LaPO_4$ (La-monazite) with a melting point higher than alumina (2070°C).[1-8] Composites of $LaPO_4$ and alumina have been produced with promising high temperature properties.[9-11]

Our aim in this contract is to gain a basic understanding of high temperature properties of $LaPO_4$, with a view to its application in high temperature structural composite materials. $LaPO_4$ (and more generally the rare-earth orthophosphates) have historically been overlooked as high temperature materials for use in corrosive and demanding environments. Previously contemplated and/or realized uses are limited to radioactive waste containment (the monazites are the ideal crystal hosts for actinide or transuranic elements), luminescent materials, scintillators, catalyst substrates and electrochemical electrodes. There is presently very little information on the fundamental high temperature properties such as sintering, grain growth, mechanical and dielectric properties. Such studies require high purity powders that previously have not been available.

Results from the work are described in sections 4 to 13. Some of the key results are as follows:

(1) Methods have been improved for synthesizing high purity stoichiometric $LaPO_4$ powder slurries and for developing uniform controlled microstructures in colloidally processed sintered bodies. This is a critical requirement for studies of intrinsic high-temperature properties of

3

LaPO$_4$; normal synthesis methods invariably lead to phosphorous-rich compositions, in which the high-temperature properties are dominated by amorphous grain boundary phases.

(2) The stability of LaPO$_4$ systems in high-temperature water-containing environments typical of combustion gases was demonstrated (collaboration with E. Opila, NASA Glenn). Reactions were found from volatile species originating from silica and alumina furnace tubes; in the case of alumina, a very thin protective layer of lanthanum aluminate was formed on the surface. However, no reactions were detected between water vapor and LaPO$_4$.

(3) The stability of LaPO$_4$ in high-temperature vacuum and reducing environments was demonstrated. Previous observations of reaction of LaPO$_4$ in direct contact with graphite, along with some incorrect thermodynamic data in the literature, had led others to speculate that LaPO$_4$ would not be stable in these environments.

(4) Debonding and sliding mechanisms were studied in model composites consisting of fully dense Al$_2$O$_3$ matrices with LaPO$_4$-coated single crystal and eutectic oxide fibers with varied interface topologies and residual stresses. These studies showed that LaPO$_4$ is compatible with, and enables debonding at all of the fibers (Al$_2$O$_3$, YAG, ZrO$_2$, and mullite). They also revealed that sliding of these fibers causes intense plastic deformation of the LaPO$_4$ coating by deformation twinning and dislocation motion at low temperatures, as well as dynamic recovery, and that these plastic deformation mechanisms could be critical for preventing the development of very high stresses during constrained sliding of rough interfaces in oxide composites.

(5) Detailed analysis was carried out of deformation twining mechanisms in LaPO$_4$ deformed at room temperature (collaboration with Randy Hay, WPAFB). Crystal structure considerations suggest that the relative abundance of twinning modes may correlate with low shear modulus on the twin plane in the direction of twinning shear, and with a possible low-energy interface structure consisting of a layer of xenotime of one half unit cell thickness at (100) and (001) twins.

(6) Studies of high temperature deformation and sliding of $LaPO_4$, including measurements of hardness and fracture toughness at temperatures up to $1000°C$ (in vacuum and air) and measurements of sliding of a sapphire pyramid over surfaces of $LaPO_4$ at temperatures up to $1000°C$ (in air), have shown that the reduction in mechanical properties with increasing temperature is less than other oxide compounds.

(7) Studies of high-temperature deformation and creep of $LaPO_4$ at temperatures in the range $1100°C$ to $1500°C$ (in air), using both stoichiometric compositions and compositions with a slight excess of P, have shown a strong effect of excess P on creep properties. The creep rates for stoichiometric $LaPO_4$ are similar to those of zirconia and alumina, a result that is perhaps surprising given the much easier room temperature deformation observed in $LaPO_4$. The implications for the behavior of $LaPO_4$ interphases in oxide composites are assessed in Sect. 9.

(8) The dielectric properties of stoichiometric $LaPO_4$ have been measured at room temperature at 8.2 GHz. The dielectric constant was similar to that of alumina, while the dielectric loss factor was very low, indicative of clean grain boundaries. In material containing excess P, the dielectric constant was not altered, but the loss was higher. The results indicate that, for use in oxide composites based on alumina, the presence of $LaPO_4$ will not significantly alter the dielectric response.

(9) Studies of directionally solidified eutectic structures (collaboration with A. Sayir, NASA) have shown the potential feasibility of an extremely high temperature oxide composite consisting of a 2-phase $Al_2O_3/LaPO_4$ structure toughened by debonding between the two phases. However, the results indicate that production of controlled microstructures will most likely require control of the atmosphere above the melt to prevent changes in composition due to preferred evaporation of P.

2.0 PUBLICATIONS, PERSONNEL AND TECHNICAL PRESENTATIONS

2.1 Personnel

The principal investigator was Dr. D. B. Marshall. Co-investigators from Rockwell Scientific were Dr. J. Davis, Dr. O. Sudre. Dr. P. E. D. Morgan and Dr. R. Housley. The program benefited greatly from several collaborations at government laboratories: Dr. R. Hay at WPAFB, Dr. B. Opila, Dr. A. Sayir and Dr. J. Eldridge at NASA Glenn.

2.2 Awards/Recognition

D. B. Marshall, ISI Original Member, Highly Cited Researchers Database, 2002

2.3 Publications

(a) published

Hay, R. S. and Marshall, D. B., "Deformation Twinning in Monazite," Acta Mat. 51[18] 5235-5254 (2003)

Davis, J. B., Hay, R. S., Marshall, D. B., Morgan, P.E.D., and Sayir, A., "The Influence of Interfacial Roughness on Fiber Sliding in Oxide Composites with La-Monazite Interphases," J. Am. Ceram. Soc., 86[2] 305-316 (2003)

Marshall, D. B., and Hannink, R. H. J., "Transformation Toughening of Ceramics," in Encyclopedia of Materials: Science and Technology, Elsevier, 2001

Marshall, D. B., Davis, J. B. "Ceramics for Future Power Generation Technology: Fiber Reinforced Oxide Composites," *Current Opinion in Solid State and Materials Science,* 5 283-289 (2001).

(b) in preparation

Davis, J. B., Sudre, O., Marshall, D. B., Morgan, P.E.D., and Housley, R, "The synthesis and processing of La-monazite," in preparation for publication in the Journal of the American Ceramic Society.

J. B. Davis, D. B. Marshall, O. Sudre, and E. Opila, "High temperature stability of $LaPO_4$ in Water Vapor, Vacuum, and CO environments," in preparation for publication in the Journal of the American Ceramic Society.

Davis, J. B., Marshall, D. B., "Hardness, Toughness, and Sliding Properties of La-Monazite at High Temperatures," *in preparation for* J. Am. Ceram. Soc

Berbon, M. Z., Davis, J. B., and Marshall, D. B., "High Temperature Creep of La-Monazite," *in preparation for* J. Am. Ceram. Soc.

J. B. Davis, W. Ho, and D. B. Marshall, "Dielectric Properties of La-Monazite," in preparation for publication as a Communication to J. Am. Ceram. Soc.

J. B. Davis, A. Sayir, and D. B. Marshall, "Directionally Solidified Structures of $LaPO_4/Al_2O_3$," in preparation for J. Am. Ceram. Soc

2.4 Technical Presentations

a. Invited

"Oxide Composites for Gas Turbine Applications," D. B. Marshall, J. Davis, O. Sudre, B. Cox and P. E. D. Morgan, invited presentation for special symposium on gas turbine materials at the American Ceramic Society Annual Meeting, April 2004.

"High Temperature Composites for Aerospace Applications," D. B. Marshall, J. B. Davis, O. Sudre, and B. N. Cox, invited presentation at International Conference: Composites at Lake Louise, Canada, Oct. 2003

"Alumina-monazite composites with interface-controlled toughness," J.B. Davis and D.B. Marshall, invited presentation, AeroMat. June, 2003

"Materials and Structures for Extreme Environments," D. B. Marshall, invited presentation at Symposium, Multifunctional Materials and Structures: a look into the future, Max-Planck Institute, Germany, March 2003.

"Damage-Tolerant Thermal Protection Systems," J. B. Davis, O. Sudre and D. B. Marshall, K. S. Oka, B. Eilertson and R. French, invited prsentation at American Ceramic Society Annual Meeting, April 2003.

"Oxide composites for thermal protection and combustion systems." D. B. Marshall, J. B. Davis, M. Z. Berbon and P. E. D. Morgan, invited presentation at International Conference: Composites at Lake Louise, Canada, Oct. 2001

b. Contributed

"Properties of Oxide Composites Containing La-Monazite," J. B, Davis, D. B. Marshall and P. E. D. Morgan, 26th Annual Conference on Composites, Materials & Structures, Cocoa Beach, Jan. 2002

"Alumina-monazite composites with interface-controlled toughness," J.B. Davis and D.B. Marshall, American Ceramic Society annual meeting, April 2003.
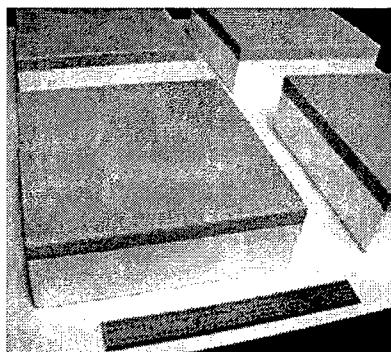
3.0 TRANSITIONS

Summary:

Basic research conducted by Rockwell Scientific Company and AFRL during the past six years has established that $LaPO_4$ has a unique set of properties needed for producing oxide ceramic composites for use in a variety of high temperature aerospace components. Methods were developed for synthesizing high purity precursors and powders necessary to study intrinsic properties and produce composites. Based on the results of this work, composites for use in thermal protection systems for space vehicles have been produced and successfully tested by the Air Force, NASA and Boeing in several 6.2 development programs, under conditions representative of re-entry (arc-jet, rain erosion, acoustic environment - technology readiness level, TRL 5). Another AFRL 6.2 program is underway to test monazite-based composites for use in a new generation of high-performance turbine-engine combustors.

What Was Accomplished:

High-temperature ceramic composites derive their damage tolerance from the presence of a relatively weak interface between the reinforcing fibers and the matrix (or a fiber coating). In the case of carbon and SiC based composites, graphite or BN coatings serve this purpose. However, these composites are not suitable for use in oxidizing environments. Until the recent discovery at Rockwell Scientific that La-monazite provides a suitable interface for oxide composites, there were no materials available for analogous oxidation-resistant composites. In this program we established the basic mechanics of interface debonding between $LaPO_4$ and several oxide fiber materials; developed methods for synthesizing $LaPO_4$ materials with well controlled chemistry (not previously available because $LaPO_4$ has been generally overlooked as a potentially useful refractory ceramic); demonstrated stability and compatibility with fibers in high temperature oxidizing and reducing environments; discovered low temperature deformation mechanisms that

enhance its performance as a constituent of the composite, and measured a variety of high temperature deformation properties.

Composites based on monazite have been transitioned to two types of thermal protection materials for re-entry vehicles: (i) the outer skin of flexible insulating blankets under the NASA SLI program led by Boeing, giving an increase in operating temperature of 1000°C over materials presently used on the space shuttle; and (ii) a protective outer skin on rigid tiles, under an AFRL DUS&T (Dual Use Science & Technology) program, also led by Boeing.

Thermal protection tiles with thin monazite-matrix composite face sheet that provides protection against impact damage

Composites based on monazite have also been transitioned to a 6.2 AFRL program for use in a new generation of high-performance turbine-engine combustors. This program combines the monazite-based composites with integral weaving techniques to enable new concepts for thin wall combustors. Testing of sub-components in the trapped vortex test rig in the propulsion division at WPAFB is planned for early 2005.
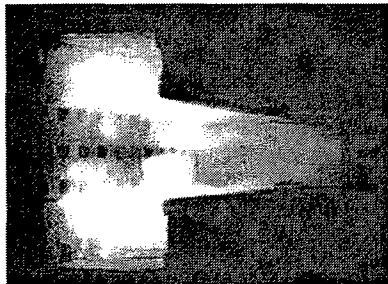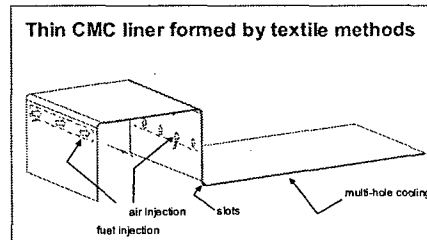
(a)   (b)

(a) TVC combustor test rig, WPAFB
(b) Schematic, thin CMC combustor wall
(c) Oxide composite wall with integrally woven coprocessed
superalloy attachment struts: Nextel 720 fibers, $Al_2O_3/LaPO_4$
matrix
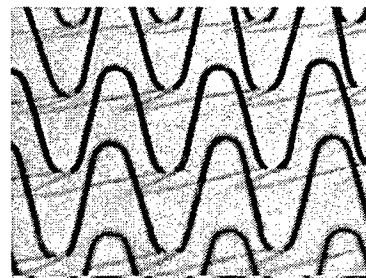
(c)

Why It Is Important:

The goal of this program is to provide the basic understanding of properties and synthesis processes for La-monazite to enable development of high-temperature, oxidation-resistant composites. The use of such composites will be key to the next generation of higher performance turbine engines and space vehicles. In the specific examples mentioned above, the higher temperature capability of monazite-based thermal protection blankets will allow the use of blankets instead of tiles over a larger fraction of a vehicle surface, resulting in large cost reductions (factor of 10), while the use of monazite-based composite surfaces on rigid tiles will protect against foreign object damage, thus leading to increased reliability, reduced maintenance, and faster turnaround.

11

Section 6

The Influence of Interfacial Roughness on Fiber Sliding In Oxide Composites with La-Monazite Interphases

by Davis, J. B., Hay, R. S., Marshall, D. B., Morgan, P.E.D., and Sayir, A.

journal

Influence of Interfacial Roughness on Fiber Sliding in Oxide Composites with La-Monazite Interphases

Janet B. Davis,[†] Randall S. Hay,[*,‡] David B. Marshall,[*,†] Peter E. D. Morgan,[†] and Ali Sayir[*,§]

Rockwell Scientific, Thousand Oaks, California 91360

Air Force Research Laboratory, Materials Directorate, Wright-Patterson AFB, Ohio 45433

NASA–Glenn Research Center/Case Western Reserve University, Cleveland, Ohio 44135

Room-temperature debonding and sliding of fibers coated with La-monazite is assessed using a composite with a polycrystalline alumina matrix and fibers of several different single crystal (mullite and sapphire) and directionally solidified eutectic ($Al_2O_3/Y_3Al_5O_{12}$ and Al_2O_3/Y-ZrO_2) compositions. These fibers provide a range of residual stresses and interfacial roughnesses. Sliding occurred over a debond crack at the fiber-coating interface when the sliding displacement and surface roughness were relatively small. At large sliding displacements with relatively rough interfaces, the monazite coatings were deformed extensively by fracture, dislocations, and occasional twinning, whereas the fibers were undamaged. Dense, fine-grained areas (10 nm grain size) resembling recrystallized microstructures were also observed in the most heavily deformed regions of the coatings. Frictional heating during sliding is assessed. Potential mechanisms for forming such microstructures at low temperature are discussed, and a parallel is drawn with the known resistance of monazite to radiation damage. The ability of La-monazite to undergo both debonding and plastic deformation relatively easily at low temperatures may enable its use as a composite interface.

I. Introduction

RARE-EARTH orthophosphates (monazite and xenotime) are of interest for fiber-matrix interphases that enable interfacial debonding and damage tolerance in oxide composites.[1–11] They are refractory materials ($LaPO_4$ melting point, 2070°C),[12] compatible in high-temperature oxidizing environments with many oxides that are either currently available as reinforcing fibers or of interest for future development as fibers and matrixes. They are also relatively soft for such refractory materials ($LaPO_4$ hardness, 5GPa).[1] Studies of several combinations of oxides and rare-earth phosphates ($LaPO_4$–Al_2O_3, $LaPO_4$–ZrO_2, $CePO_4$–ZrO_2, YPO_4–Al_2O_3, and $NdPO_4$–Al_2O_3) have shown that the oxide-phosphate interfacial bond is sufficiently weak that debonding occurs whenever a crack approaches an interface from within the phosphate.[1,13–15] The most detailed studies have involved the $LaPO_4$–Al_2O_3 system. Other studies have shown that debonding and

sliding occur in fiber pushout tests with model composites consisting of $LaPO_4$-coated single crystal fibers of Al_2O_3 and $Y_3Al_5O_{12}$ (YAG) in polycrystalline Al_2O_3 matrices.[1,16]

Damage-tolerant behavior in ceramic composites requires sliding and pullout of fibers in addition to interfacial debonding. Recent calculations suggest that such pullout would be strongly suppressed in fully dense oxide composites by misfit stresses generated during sliding of fibers with rough interfaces or with minor fluctuations in diameter.[17] For given strain mismatch, these misfit stresses are expected (assuming elastic accommodation) to be larger in composites with oxide interphases than in composites with turbostratic carbon or boron nitride interphases, which have low transverse elastic modulus. However, the misfit stresses could potentially be reduced by plastic deformation of the interphase. The higher elastic modulus in oxide interphases also causes larger residual thermal stresses in systems with matrix and fibers of different thermal expansion coefficients.

In this study, we investigate the debonding and sliding behavior of four La-monazite coated fibers (single-crystal alumina and mullite, directionally solidified eutectics of Al_2O_3/YAG, and Al_2O_3/Y-ZrO_2), chosen to provide different residual stress states and interface morphology. The coated fibers were surrounded with a matrix of polycrystalline Al_2O_3. Debonding and sliding were assessed using indentation fracture and pushout techniques. Damage in the coating, including plastic deformation, was identified by scanning and transmission electron microscopy (SEM and TEM).

II. Experimental Procedure

Four different single crystal or directionally solidified eutectic oxide fibers, grown at NASA Glenn by a laser-heated float zone technique,[18,19] were coated with $LaPO_4$ by dipping in a slurry of rhabdophane (hydrated $LaPO_4$). The coated fibers were embedded in α-alumina powder (AKP50, Sumitomo Chemicals, Tokyo, Japan) and hot pressed in graphite dies for 1 h at 1400°C. Uncoated fibers were included in the same specimen for reference. The fibers were arranged in rows within the one hot-pressed disk, with separation between fibers ~2 mm, thus ensuring identical processing conditions for all fibers. In an earlier study,[3] the same rhabdophane slurry yielded pure La-monazite, with no excess lanthanum or phosphorus being detectable either by energy dispersive spectroscopy (EDS) analysis of the monazite or by reaction of the monazite with sapphire fibers after long-term heat treatment (200 h at 1600°C).

The fibers had different surface textures and thermal expansion coefficients, thus allowing assessment of the effects of interfacial morphology and residual stress on debonding and sliding mechanisms. The fibers were as follows:

(1) Directionally solidified Al_2O_3/ZrO_2 eutectic fibers with a two-phase microstructure of alumina and cubic zirconia (stabilized with Y_2O_3).[20] Dimensions of the individual phases were ~0.5 μm. The starting composition of the feed rod was 60.8 mol% Al_2O_3; 39.2 mol% ZrO_2 (9.5 mol% Y_2O_3) with purity levels 99.995% or better. X-ray diffractometry (XRD) and SEM/TEM analysis did

not show any evidence for a third phase, indicating that all the Y_2O_3 was in solid solution in the ZrO_2. The surfaces of the fibers were rough on the scale of the microstructure (Fig. 1(a)). The fiber diameters were $\sim$100 μm with fluctuations of $\sim$2 μm over lengths

of $\sim$200 μm. Thermal mismatch during cooling of the composite caused tensile radial stresses normal to the fiber surface (Table I).

(2) Directionally solidified Al_2O_3/YAG eutectic fibers,[21] with a two-phase microstructure of dimensions $\sim$0.5 μm and surface roughness on the scale of the microstructure (Fig. 1(b)). The fiber diameters were $\sim$100 μm, with fluctuations of <1 μm over lengths of $\sim$1 mm. Thermal mismatch stresses were of the same sign as for the Al_2O_3/ZrO_2 fibers, but were smaller in magnitude (Table I).

(3) Mullite single-crystal fibers formed from a source rod of high-purity (99.99%) polycrystalline alumina powder (CERAC, Milwaukee, WI) and 99.99% pure SiO_2 (Alfa Products, Ward Hill, MA), which gave 2:1 mullite as described in Ref. 19. In the as-grown condition, the fibers had smooth surfaces but relatively large fluctuations in diameter (50 ± 5 μm, Fig. 1(c)) with period $\sim$100 μm. Thermal mismatch caused large compressive radial stress in the coating and at the fiber-coating and coating-matrix interfaces, with tensile circumferential stress in the coating and matrix (Table I).

(4) Sapphire fibers, which had smooth surfaces (as-grown) and relatively uniform diameter (100 ± 1 μm). These were included for comparison with previous studies of this system.[1,3] All residual stresses except the circumferential (and axial) tension in the coating are small.

The hot-pressed disk was cut into slices (thickness $\sim$0.3–2 mm) normal to the fibers. The surfaces of the slices were polished using diamond paste and some of the polished slices were thermally etched. The thicker slices were used for indentation cracking experiments, which involved placing Vickers indentations (10 kg load) in the polycrystalline alumina matrix near the fibers. The indenter was oriented so that one of the median/radial cracks grew toward the fiber to test for interfacial debonding. The thinner slices were used for fiber pushout experiments, which involved loading a flat punch (truncated Vickers indenter) onto the end of each fiber, while the slice was supported in a fixture with a gap beneath the fiber. Some specimens were fractured after the pushout test to separate the debonded interface. The indented and pushed out specimens were examined by optical microscopy and SEM.

Specimens used for fiber pushout were also sectioned parallel and perpendicular to the fiber axes and examined by TEM (Model CM20 FEG operating at 200 kV, Phillips, Eindhoven, Netherlands) to allow identification of damage within the $LaPO_4$ coating caused by debonding and sliding. Four Al_2O_3/YAG fibers were examined in the parallel section; one mullite and one Al_2O_3/ZrO_2 were examined in the axial section. The TEM foils were prepared by impregnating the specimens with epoxy, tripod polishing to a thickness of 10 μm, followed by ion milling (Model 691 operating at 4.5 kV, Gatan, Pleasanton, CA).[26]

III. Results

(1) Microstructural Observations

All the coated fibers were surrounded with a continuous layer of $LaPO_4$ and a fully dense matrix of polycrystalline Al_2O_3. Deformation during hot pressing caused the coating thickness to be larger along the sides of the fibers ($\sim$5 μm) than at the top and bottom ($\sim$1 μm). No reactions were observed between the $LaPO_4$ and any of the fibers, although a few isolated elongated La-magnetoplumbite ($LaAl_{11}O_{19}$) grains were observed along the coating-matrix interface (perhaps the result of alkali or divalent impurities in the matrix, which are known to assist formation of rare-earth magetoplumbite-like structures[3]). Despite the presence of substantial tensile residual stresses in all the $LaPO_4$ coatings ($\sim$300–400 MPa, Table I), no evidence of cracking was detected by SEM examination of polished or thermally etched cross sections (although fine-scale through-thickness coating cracks were observed in thin TEM foils of other similar composites). The grain sizes were $\sim$0.5–1 μm in the monazite and $\sim$2–10 μm in the alumina matrix.
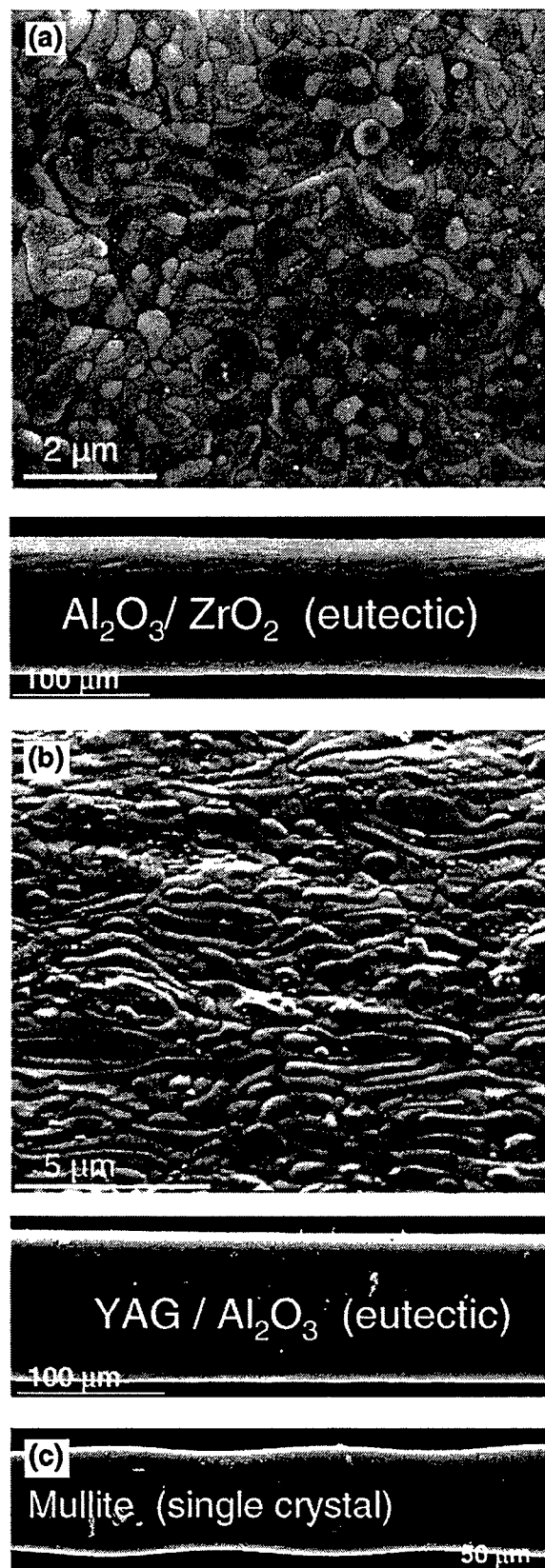
Fig. 1. SEM micrographs of fiber surfaces: (a) Al_2O_3/ZrO_2 eutectic fiber, (b) Al_2O_3/YAG eutectic fiber, and (c) mullite single crystal fiber.

Table I. Representative[†] Residual Stresses in Composites of Monazite-Coated Fibers in a Polycrystalline Al_2O_3 Matrix

Stress component	Residual stress (MPa)			
	Sapphire	Mullite	Al_2O_3/YAG	Al_2O_3/ZrO_2
Radial (coating/fiber)	15	−720	130	240
Radial (matrix/coating)	25	−630	140	240
Circumferential (coating)	300	420	290	280
Axial (fiber)	7	−1160	240	420

[†]Values in this table are intended only as rough guide for relative stresses. They were calculated using a coaxial cylinder analysis,[22] assuming a temperature change of $\Delta T = 1000°C$, coating thickness of 2 μm, zero volume fraction of fibers, and the following Young's moduli and thermal expansion coefficients (nominal isotropic, temperature-independent values): polycrystalline Al_2O_3 (400 GPa, 8×10^{-6} °C^{-1}); sapphire (400 GPa, 8×10^{-6} °C^{-1}); mullite (200 GPa, 4×10^{-6} °C^{-1}); Al_2O_3/ZrO_2 (300 GPa, 9×10^{-6} °C^{-1}); and Al_2O_3/YAG (350 GPa, 8.5×10^{-6} °C^{-1}).[23–25]

Fig. 2. SEM micrographs showing interactions of indentation cracks with Al_2O_3/YAG eutectic fibers: (a) uncoated fiber in alumina matrix (indentation located below region shown); (b) fiber coated with $LaPO_4$ (indentation located out of field of views, as indicated in (d)); (c) same fiber as in (b) but showing region further along the debonded interface (arrows indicate magnitude of sliding displacement across debond crack); (d) schematic showing locations of (b) and (c).

(2) Interfacial Debonding

The LaPO$_4$ coatings protected all the fibers from penetration of indentation cracks, whereas uncoated fibers were always penetrated. Examples are shown for the Al$_2$O$_3$/YAG, Al$_2$O$_3$/ZrO$_2$ and mullite fibers in Figs. 2–4. The indentation cracks generally extended from the matrix into the LaPO$_4$ coatings then arrested and caused debonding at the coating/fiber interface. In a few cases with the Al$_2$O$_3$/ZrO$_2$ fibers, debonding occurred at both interfaces (matrix/coating and coating/fiber). The former response was observed previously with coated sapphire fibers and was shown to be consistent with the debond criterion of He and Hutchinson[27] and the measured fracture toughnesses of the fibers, coating, and interface.[1] Although the fracture toughnesses of the YAG/LaPO$_4$ and mullite/LaPO$_4$ interfaces have not been measured, the present observations suggest that they are similar to that of the alumina/LaPO$_4$ interface (~4.5 J/m^2). It is noteworthy that the fibers were protected from cracking even when the contact area of the Vickers indentation was close enough to the fiber to overlap the coating (Fig. 3(b)). In that case, the residual stress from the indentation (compressive normal to the interface, tensile on the prospective crack plane into the fiber) would tend to inhibit debonding and favor fiber penetration.

The interfacial roughnesses for both of the eutectic fibers were similar to the surface roughnesses of the as-formed fibers, with amplitude ~100–300 nm and period ~500 nm (Figs. 2(a) and 3(a)). This roughness amplitude is greater than that of the interfaces at the single-crystal mullite and sapphire fibers. The initially smooth single crystal fibers developed cusps during hot pressing where grain boundaries of the monazite coating intersected the fiber surface. Measurements of the cusp profiles on sapphire fibers
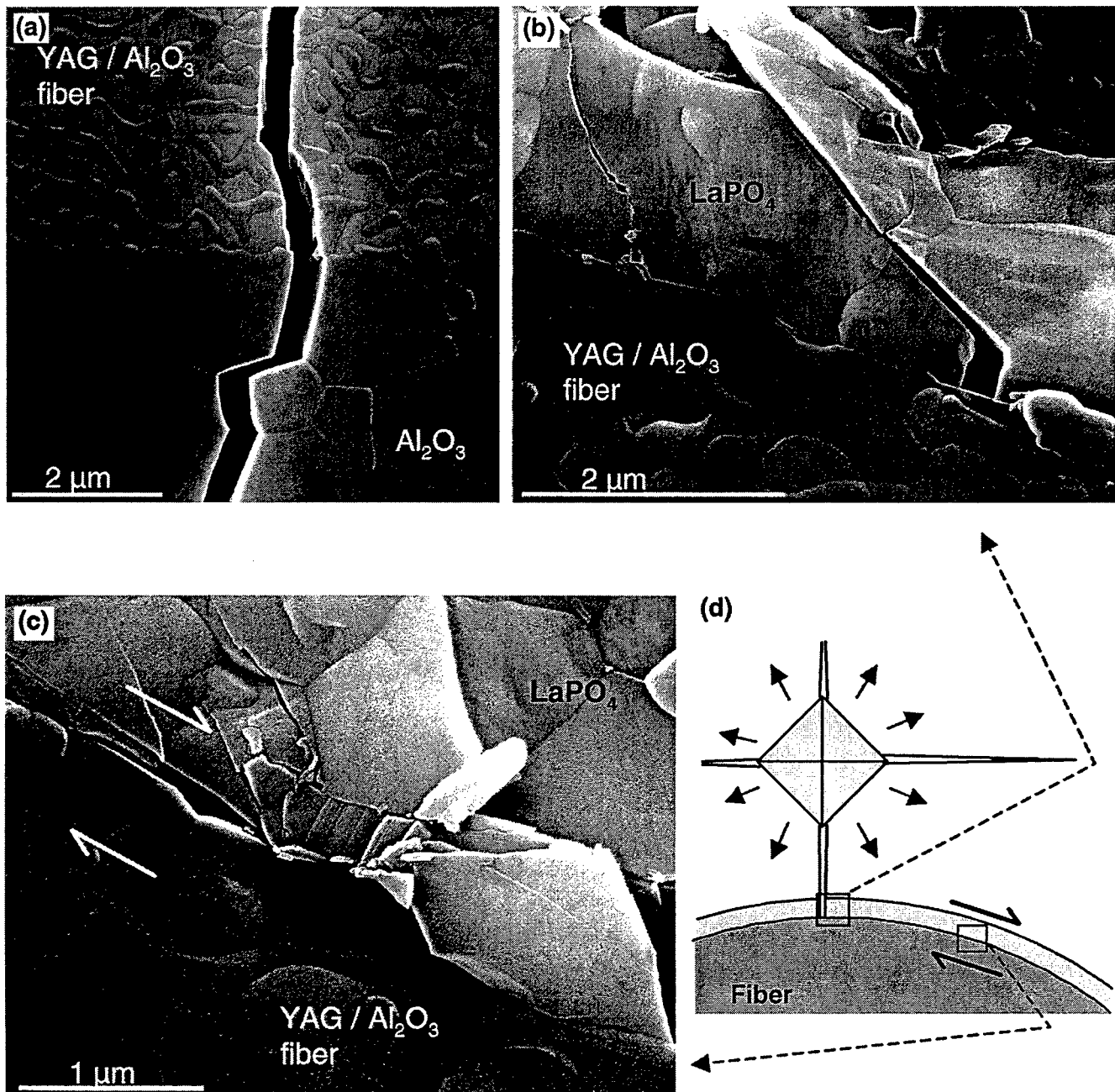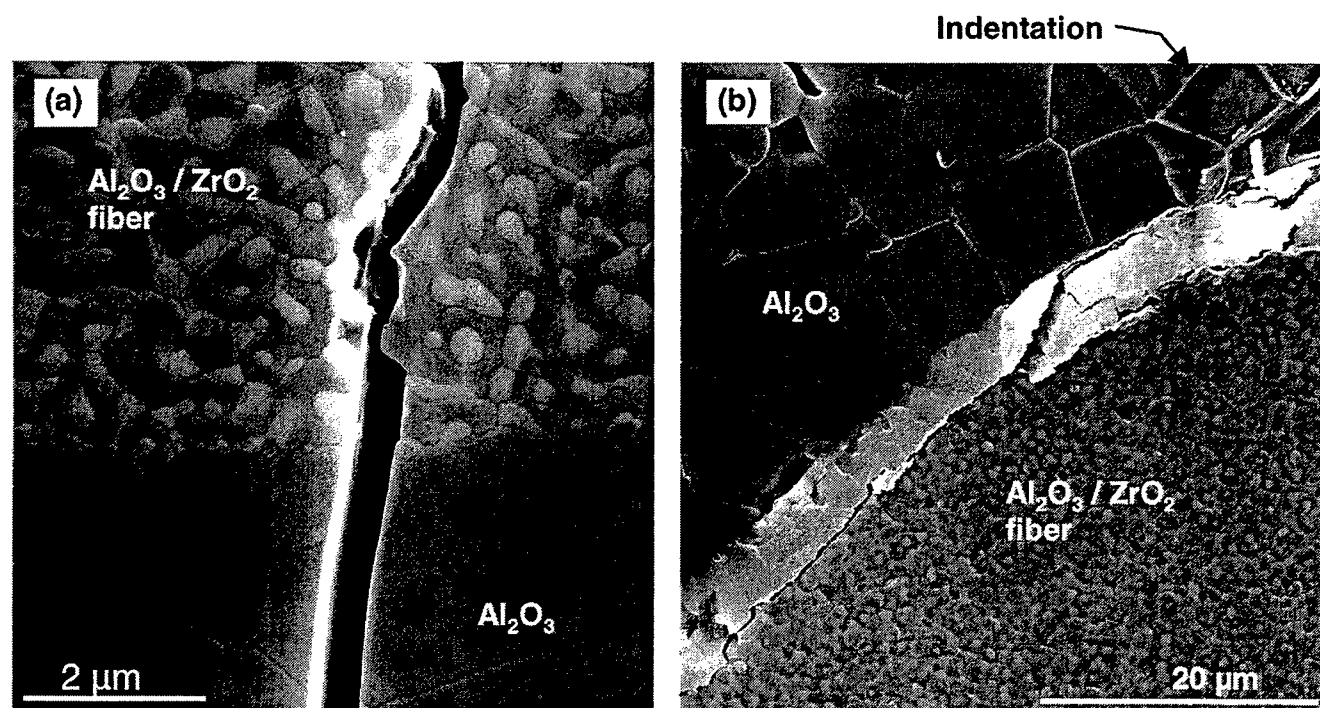

Fig. 3. SEM micrographs showing interactions of indentation cracks with Al$_2$O$_3$/ZrO$_2$ eutectic fibers: (a) uncoated fiber in alumina matrix (indentation located below region shown); (b) fiber coated with LaPO$_4$ (indentation located at top of field of view).
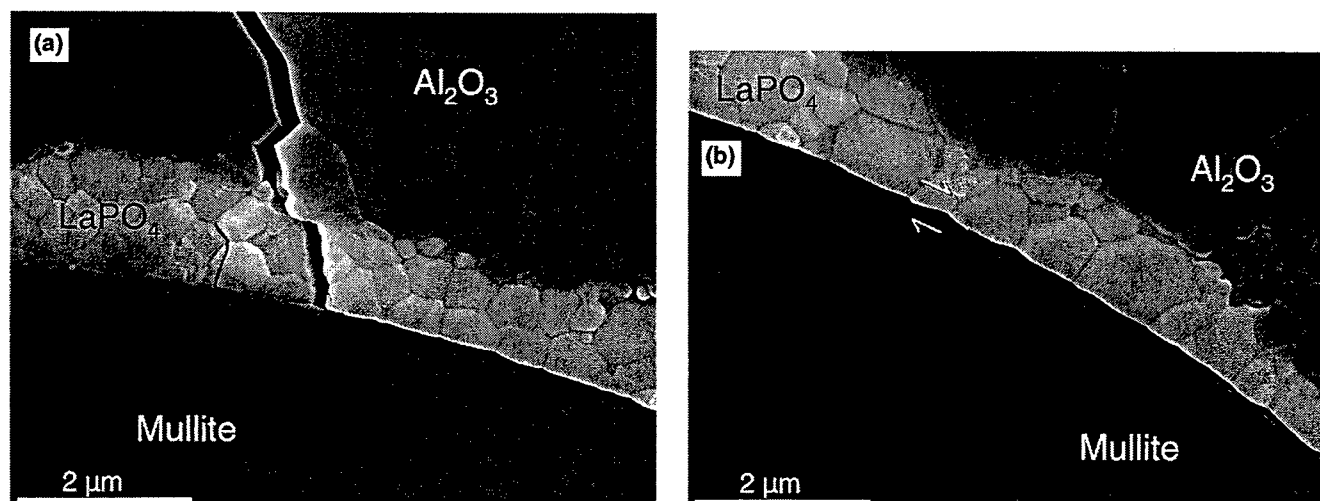
Fig. 4. SEM micrographs showing interaction of indentation crack with single-crystal mullite fiber (coated with LaPO$_4$, in alumina matrix): (a) intersection of indentation crack with interface and debonding (indentation located above region shown); (b) same fiber as in (a) but showing region further to the right along the debonded interface (arrows indicate magnitude of sliding displacement across debond crack).

by atomic force microscopy (ATM) have been reported else-where.[28,29] The cusp heights were typically ~50 nm, and the angular distortions of the surface were small ($\leq$20°). The cusps on the mullite surfaces were very similar.

Some insight into the effect of interfacial roughness on fiber sliding and pullout can be gained from the observations of Figs. 2–4. As the debond grows around the circumference of the fiber, the loading on the crack tip due to the indentation stress field is initially mostly shear (although the loading eventually changes to tension if the crack grows sufficiently). Because fiber pullout also involves shear loading of a debond crack, the initial region of growth of the deflected cracks in Figs. 2–4 should be representative of the behavior during the corresponding stage of pullout.

In all cases, the initial debond crack followed the fiber-matrix interface, even when the interface was rough. For the mullite fibers (Fig. 4) the sliding displacement of the debond crack surfaces (~250 nm, i.e., opening displacement of initial indentation crack) is smaller than the average spacing between the interfacial cusps (~600 nm). Sliding caused separation of the debonded surfaces to accommodate their misfit (Fig. 4(b)), despite the constrained configuration with large residual compressive normal stress (~700 MPa; Table I). The misfit was apparently accommodated by elastic strains, with no irreversible deformation of the mullite fiber or the LaPO$_4$ coating discernable by SEM. In contrast, sliding of the eutectic fibers caused extensive damage in the LaPO$_4$ coating (Fig. 2 (c)), without discernable damage in the fibers. The damage included cracks across the full width of the coating, aligned at ~45° to the interface on planes of maximum tension, similar to previous observations of cracking in layers of LaPO$_4$ sandwiched between polycrystalline Al$_2$O$_3$.[1] More intense local damage is evident at individual asperities, as in Fig. 2(c). The damage included cracking and fine lamellar features, which could be cracks or twins.

(3) Fiber Pushout

All the fibers debonded during the pushout experiments. Sliding occurred unstably over distances of ~5–10 μm at a critical load between 10–20 N. The average shear stress (load divided by fiber surface area) at the critical load was 130 ± 10 MPa for the sapphire fibers, 200 ± 20 MPa for the mullite fibers, 190 ± 20 MPa for the Al$_2$O$_3$/YAG fibers, and 255 ± 30 MPa for the Al$_2$O$_3$/ZrO$_2$ fibers.

(A) Sapphire Fibers: Sliding of the sapphire fiber occurred at the fiber-coating interface, as reported previously.[1] Grain-boundary cusps were observed along the separated interfaces by SEM and AFM, although no damage was visible in either the fiber or the coating.

(B) Al$_2$O$_3$/YAG and Al$_2$O$_3$/ZrO$_2$ Fibers: Extensive wear tracks were observed in the LaPO$_4$ coatings on both eutectic fibers, indicating that sliding involved plastic deformation (Fig. 5). Sliding occurred mostly adjacent to the fiber-matrix interface, although smeared fragments of the LaPO$_4$ coating remained on the fiber surface. In some regions (such as Fig. 5), sliding occurred near the matrix-coating interface.

TEM observations from a typical specimen containing a pushed out Al$_2$O$_3$/YAG fiber are shown in Figs. 6–8. Sliding occurred along a debond crack between the LaPO$_4$ coating and the fiber. In most regions, a thin layer of the LaPO$_4$ coating within ~100–300 nm of the fiber was heavily deformed (Figs. 6–8). The intensity of deformation decreased with distance from the debond crack, with regions more than ~500 nm from the fiber being undeformed. The Al$_2$O$_3$/YAG fiber was also undamaged.

Deformation in the LaPO$_4$ consisted of tangled dislocations, lamellar features resembling twins, microcracks, and regions of densely packed fine crystallites (diameter as small as 10 nm) that resemble recrystallized microstructures (Fig. 6). The density of dislocations varied from grain to grain and generally decreased with distance from the debond crack. The nano-crystalline regions were within ~50–100 nm of the debond crack. In one region, there was no deformation on the monazite side of the debond crack, but a thin layer of dense nano-crystalline monazite was smeared on the

fiber surface. In some areas, this smeared layer was overlaid with a less dense, coarser grained agglomeration of angular monazite particles of diameter ~50–100 nm (Fig. 7), suggestive of cata-clastic flow, a process involving repeated microfracture and fine-particle transport.[30] Similar features (intense deformation, fine crystallites, and agglomerates of angular particles) were observed in monazite debris (irregularly shaped balls, ~100–500 nm diameter) in the debond crack.

(C) Mullite Fibers: Sliding of the mullite fibers occurred predominantly at the fiber-coating interface. SEM observations of separated interfaces showed plastic deformation of the LaPO$_4$ coating where the varying fiber diameter caused compression of the coating during sliding, as depicted in region B of Fig. 9. (Note that the sliding displacements are smaller than the period of the diameter fluctuations and larger than the spacing of cusps associated with grain boundaries in the LaPO$_4$ coating.) Where sliding caused tension across the coating-fiber interface (region A in Fig. 9), the separated interface was similar to that of the sapphire fiber, with grain-boundary cusps, clean separation, and no damage in the fiber or the coating.

Direct correlation of the changes in coating damage with fiber diameter fluctuation by TEM was difficult, because only limited areas were observed. Nevertheless, some trends are evident. Deformation was distributed, often nonuniformly, through the entire coating thickness (Figs. 10 and 11), rather than being localized in a thin layer adjacent to the fiber as for the Al$_2$O$_3$/YAG fiber. In some places, the monazite adjacent to the fiber was undeformed, whereas in others plastic deformation was confined to an isolated grain (Fig. 10). The region of Fig. 10 was thought to have experienced tension during sliding (as in Region A, Fig. 9), although the correlation with fiber diameter is uncertain because some of the fiber adjacent to the debond crack was removed during ion milling. Extensive microcracking was distributed throughout the coating, often at ~±45° to the fiber surface (Figs. 10 and 11).

In regions of coating inferred to have been compressed during sliding (as in region B of Fig. 9), almost the entire coating was microcracked and plastically deformed (Fig. 11). Extensive dislo-cation plasticity was evident, with variations in density from grain to grain. Some grains were twinned parallel to the fiber/matrix interface (Fig. 11), the orientation of maximum shear stress due to pushout of the fiber. Microcracking at ~45° to the fiber surface was extensive, with crack spacings as small as ~50 nm and an abundance of planar segments consistent with cleavage on, (100), (010), and (001), as reported previously.[31] There was some tendency for cracks oriented normal to the maximum tensile stress (northwest to southeast in Fig. 11) to be longer and have greater opening displacements than other cracks; however, the trends are subjective and the possibility of a sample preparation artifact cannot be ruled out.

IV. Discussion

(1) Effects of Residual Stress

The residual stresses noted in Table I might be expected to influence interfacial debonding. Therefore, it is necessary to establish whether the fracture behavior in the model experiments reported here is representative of that in real composites, given the differences in residual stress states and crack orientations.

In the analysis of He *et al.*,[32] the presence of residual stresses shifts the debond criterion by an amount that depends on the parameters η_p and η_d:

$$\eta_p = \frac{\sigma_p a^{1/2}}{K}, \quad \eta_d = \frac{\sigma_d a^{1/2}}{K} \tag{1}$$

where σ_p and σ_d are the residual stresses normal to potential crack paths along the interface or into the fiber, K is the applied stress intensity factor for the incident crack, and a is a defect size. For a crack approaching the fiber on a radial plane, as in the indentation cracking experiments of Section II(2), the residual stresses σ_p and σ_d (radial and hoop stresses at the fiber surface) are equal, so the debond condition is not affected by the residual stresses.

For cracks oriented normal to the fiber axis (the most important case for a composite), σ_p is the axial stress in the fiber and σ_d is the radial stress at the fiber surface. The ratio of the axial to the radial stress is ~2 for all the fibers (Table I), both stresses being compressive for the mullite fibers and tensile for the others. Therefore, the residual stresses should favor debonding for mullite fibers and fiber penetration for both eutectic fibers. However, this result is sensitive to the volume fraction of fibers. For a fiber volume fraction of 0.5, a typical value for structural composites, the magnitudes of the axial stresses decrease by a factor of ~2 to a level similar to the radial stresses. Then the residual stresses do not affect the condition for debonding and observations from cracks oriented as in the model indentation experiments are representative of transverse cracking in the composite. The additional influence of the residual stress field of the indentation, which favors penetration of the crack into the fiber, makes the indentation crack a conservative indicator for debonding.

(2) Effects of Misfit Stresses

Misfit stresses were generated during fiber sliding by roughness at two length scales, one microstructural (grooves that form at intersections of grain boundaries in the monazite coating or lamellae boundaries of the eutectic fibers with the fiber/coating interface), and the other caused by long-range fluctuations in fiber diameter (Fig. 1 and Table II). Sliding displacements in the pushout experiments exceeded the microstructural dimensions by a factor of ~5–10, but were smaller than the period of the diameter fluctuations by factors of ~10–100. The microstructural roughness dominated the misfit strains for the eutectic fibers and sapphire fibers (Table II).

For the mullite fibers, the superposition of misfit strains caused by thermal expansion mismatch (Table I) and diameter fluctuations (at the maximum sliding displacement) would cause compressive radial stresses as high as 5.2 GPa in some regions and tension in others. Because this maximum compressive stress is similar to the hardness of $LaPO_4$ (5 GPa[1]), plastic deformation should occur throughout the coating, as observed in Fig. 11.

For the other fibers, the maximum radial mismatch caused by fluctuations in fiber diameter is of similar magnitude and opposite sign to the thermal expansion mismatch. Therefore, deformation of the coating should depend on the microstructural roughness (both the roughness shape and the mismatch strain, $\delta r/R$). The single crystal fibers had smaller microstructural mismatch strains ($\delta r/R < 0.002$) than the eutectic fibers ($\delta r/R \approx 0.004$).

The only oxide fibers currently available commercially in quantities sufficient to fabricate composites are polycrystalline, with grain size ~50–100 nm and diameter ~12 μm.[33,34] The surface roughness due to grain-boundary grooving in as-fabricated fibers is typically very small (<5 nm for Nextel 720^{TM}, 3M Corp., St. Paul, MN).[35] However, the grooves would be expected to grow during processing of the matrix to depths up to approximately half of the grain size (~20–50 nm). Although this roughness amplitude is smaller than that of the eutectic fibers, the mismatch strain is similar or larger ($\delta r/R \approx 0.003–0.005$). Therefore, deformation of the coating might be expected if these fibers were to be embedded in a matrix with stiffness similar to that used in this study. However, in a composite with a porous matrix, the response would be mitigated by the reduced constraint, owing to the lower elastic stiffness of the matrix.

(3) Plastic Deformation of $LaPO_4$

The sliding of rough interfaces over distances large compared with the roughness wavelength caused plastic deformation of monazite coatings (Figs. 5–8). Plastic deformation of monazite by twinning and dislocations has also been observed after quasi-static contact with spherical indenters at room temperature.[31,37] Such deformation can occur in any brittle material in the presence of sufficient hydrostatic pressure to suppress fracture.[38–43] Because monazite, with a hardness of 5 GPa,[1] is much softer than alumina, zirconia, and mullite (hardnesses ranging between 10–40 GPa),[44]

sliding of these fibers is expected to deform the monazite without damaging the fibers.

Wear and abrasion of ceramics are known to cause intense plastic deformation, similar to that in heavily cold-worked metals, with fine, heavily deformed wear debris as in Fig. 6–8.[43,45–48] The depth of the deformed zone is expected to be similar to the dimensions of the sliding asperities, consistent with the observations of Figs. 6–8 (~500 nm depth of monazite deformation from sliding of Al_2O_3/YAG fiber with roughness amplitude ~200 nm and wavelength ~1 μm). Mullite fibers, with larger roughness amplitude (2.5 μm) and wavelength (100 μm), deform the entire coating, rather than just a thin layer. Abrasive wear of interfaces in a composite can affect the fiber sliding resistance and thus the mechanical properties of the composite, particularly during fatigue.[49]

The mechanism responsible for forming the dense nano-crystalline regions that resemble recrystallized grains, as in Fig. 6, is not known. Recrystallization normally occurs only at sufficiently high temperatures and long times to allow dislocation climb.[50] This would not be expected during room-temperature deformation of a refractory material, such as $LaPO_4$, and was not observed in indented monazite.[31] In alumina, which has a similar melting point, recovery and recrystallization of cold-worked microstructures typically requires temperatures of at least 800°C,[45] and perhaps as high as 1200°C.[51] This raises a question of whether friction caused local heating in these experiments, or whether another mechanism might be responsible for this microstructure. Two possible mechanisms are low-temperature amorphization and recovery, which has been observed in wear and abrasion of two-phase metals,[48] or very fine-scale comminution accompanied by densification by local deformation.

(A) Local Heating Effects: Several estimates of temperature rises during sliding, based on different assumptions about heat dissipation mechanisms, are given in Appendix A. An upper (adiabatic) limit for quasi-static continuous deformation gives temperature rises between ~800°–2000°C, depending on whether analysis is performed for individual asperities or for an average contact area. However, according to a very conservative estimate, an upper-bound for the sliding velocity is several orders of magnitude smaller than that required for adiabatic heating. A similar conclusion is drawn from application of frictional sliding analyses,[52–54] which give small temperature increments for this upper-bound sliding velocity (~0.5°C for an asperity calculation and ~5°C for an average calculation).

These calculations indicate that significant increases in temperature could not have occurred in these experiments if the assumptions of quasi-static, continuous deformation are valid. Several mechanisms could potentially violate these conditions by producing local discontinuous deformation. One is stick slip motion, which causes local sliding velocities significantly larger than average.[55] The local velocity would need to exceed the maximum upper-bound average velocity by a factor of ~100 to approach adiabatic conditions (Appendix A). Although this is possible (local elastic unloading could cause local velocities approaching sonic values), experiments and geological observations have found less heating during stick-slip than during stable sliding[55] (reduction of normal stress by interface separation waves were suggested as a cause).

Another mechanism is cataclastic flow[30] accompanied by plastic deformation of the debris. Fine-grained (50–100 nm), angular, and porous monazite debris characteristic of cataclastic flow was observed in some regions (Fig. 7). The prevalence of other deformation microstructures (dislocations, nano-crystalline regions) also varied from place to place, suggesting that there was spatial and perhaps temporal variation in the intensity of deformation during the pushout experiments. Local adiabatic heating could occur during cataclastic flow as a result of imperfect contact between the debris and the surroundings, leading to reduced heat conduction to the surroundings, or by local stick-slip motion of the angular debris causing rapid impact of sharp particles. In geological studies, fine-grained debris (fault gouge) is itself suspected to influence whether
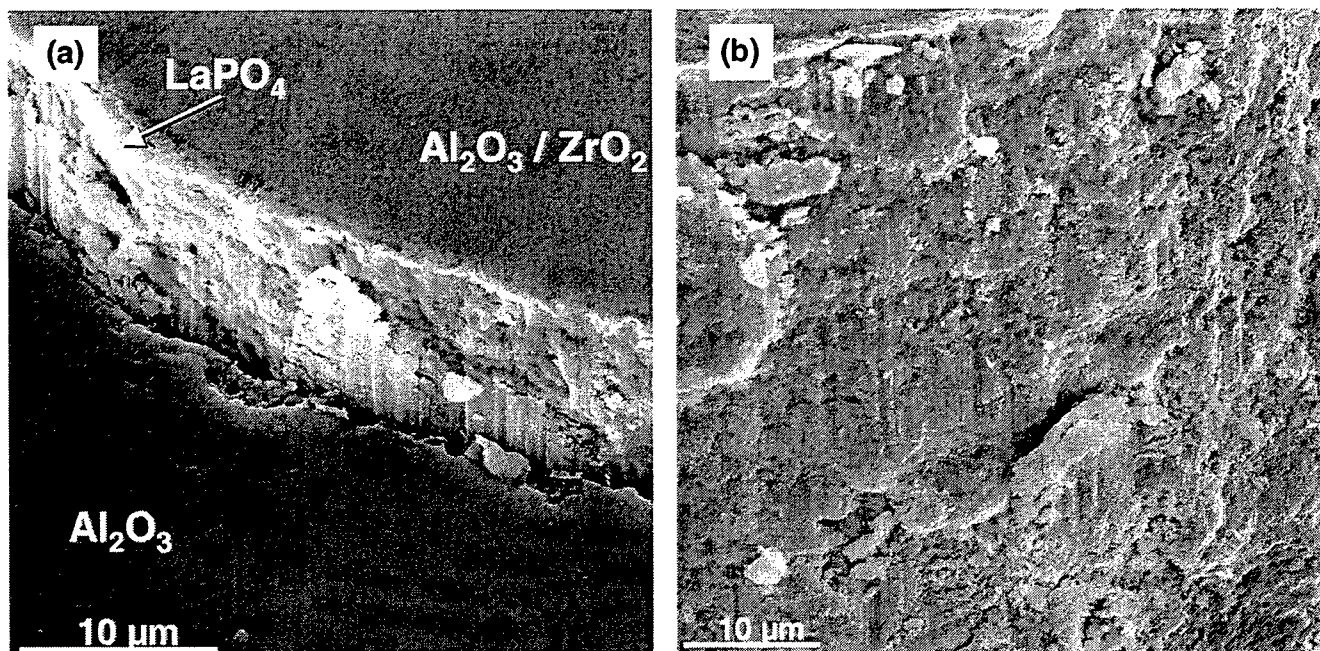
Fig. 5. SEM micrographs showing Al_2O_3/ZrO_2 eutectic fiber after push-out: (a) bottom of push-out specimen (monazite-coated eutectic fiber, polycrystalline Al_2O_3 matrix); (b) monazite layer remaining attached to fiber, showing deformation caused by sliding.
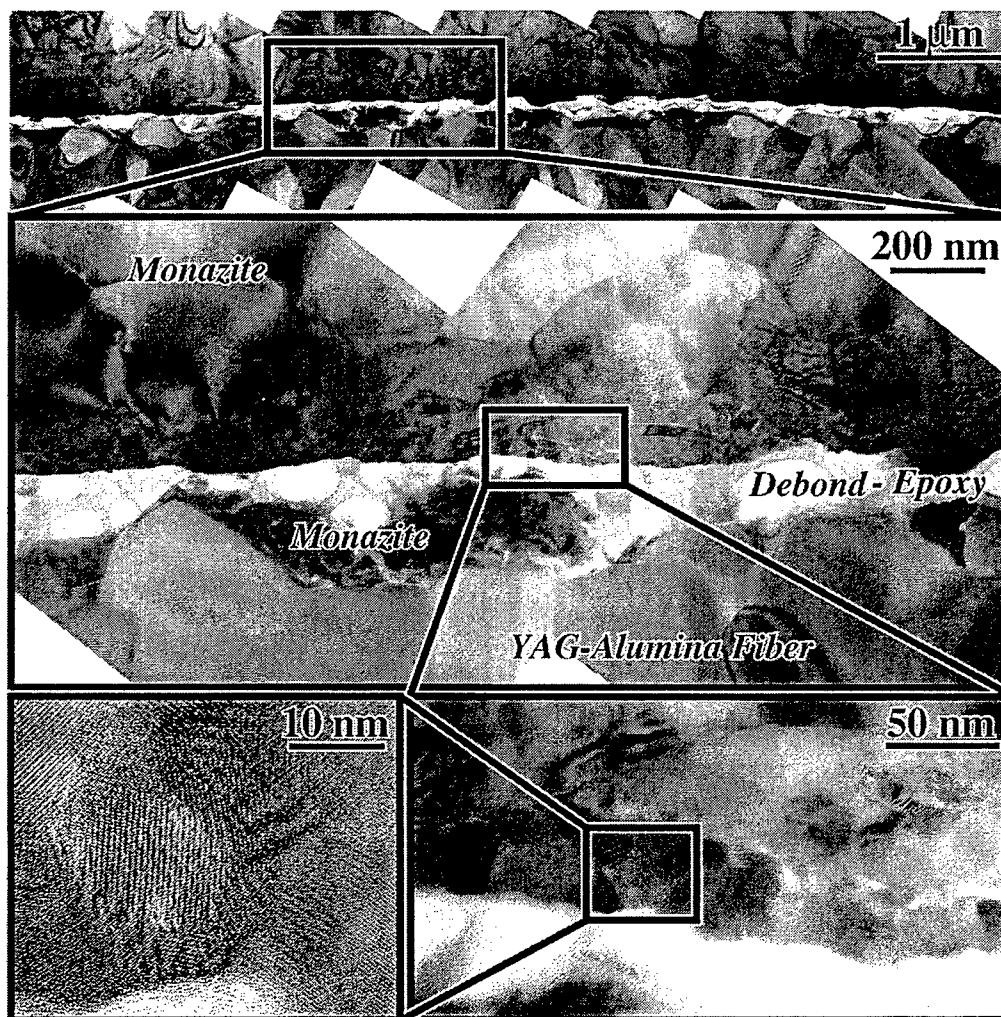
Fig. 6. TEM micrographs at progressively increasing magnification from cross section of monazite-coated Al_2O_3/YAG fiber after push-out. Heavily deformed monazite debris between asperities on the fiber surface is evident at intermediate magnification. Dense nano-crystalline microstructure along the debond crack is evident at high-magnification.
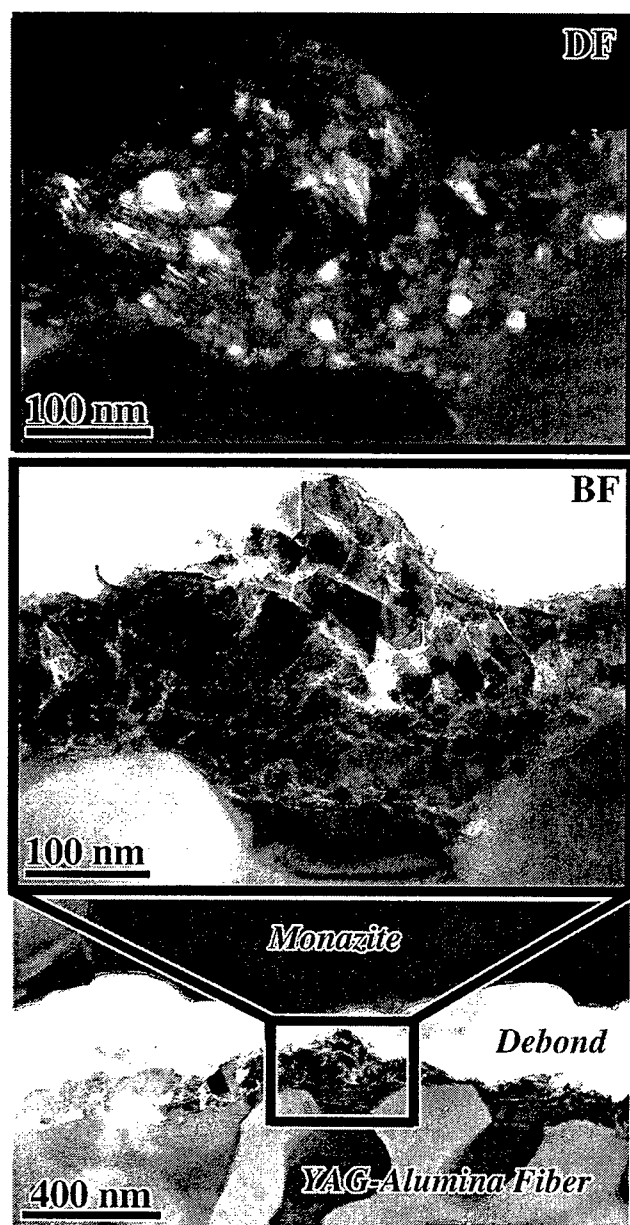
Fig. 7. TEM micrograph of monazite smeared onto Al$_2$O$_3$/YAG fiber surface. Layer adjacent to fiber has dense fine grains (~10–20 nm scale) resembling recrystallized microstructure. Layer further from fiber has more porous, coarse-grained angular particles diagnostic of cataclastic flow.

stick-slip or stable sliding occurs, with most observations pointing toward inhibition of stick-slip by fine-grained debris.[30] A progression from stick-slip to stable sliding as debris builds up during fiber pushout displacement is possible, with a consequent change in local temperature increases. Unfortunately, it is not straightforward to assess any of these effects quantitatively.

(B) Annealing of Radiation Damage: Monazite is known to recover readily from displacive damage events at near-ambient temperatures,[56,57] making it extremely resistant to amorphization by radiation damage, and thus an ideal host for containment of actinide or transuranic elements.[58,59] In a recent study,[60] radiation damage in LaPO$_4$ and several related ABO$_4$-type phosphates and silicates was monitored as a function of temperature *in situ* by TEM. Fundamental differences in the amorphization and recrystallization kinetics between the orthophosphates and silicates were observed. The critical temperature above which amorphization
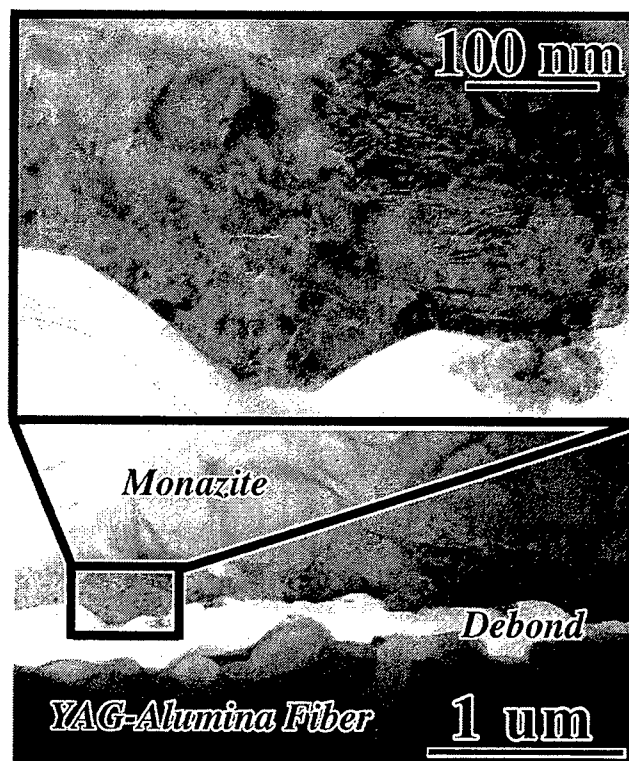
Fig. 8. Intense plastic deformation and fine-scale microcracking in coating on Al$_2$O$_3$/YAG fiber. Heavily deformed ball of monazite (~100 nm diameter) is evident in debond crack at higher magnification (lower right-hand corner).

could not be induced (i.e., recrystallization processes were faster than damage accumulation) was only 35°C for LaPO$_4$, but >700°C for zircon. This difference was tentatively attributed to the higher stability of isolated PO$_4$ tetrahedra than isolated SiO$_4$ units, with less bond-breaking required to crystallize the amorphous structure.

Whether this behavior might be related to recrystallization after intense mechanical deformation is not clear. Recrystallization of a
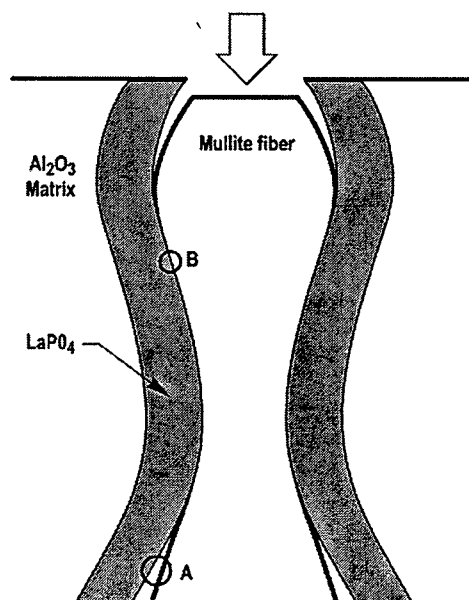
RSC0828 090501

Fig. 9. Schematic of fiber sliding for monazite-coated mullite fiber.
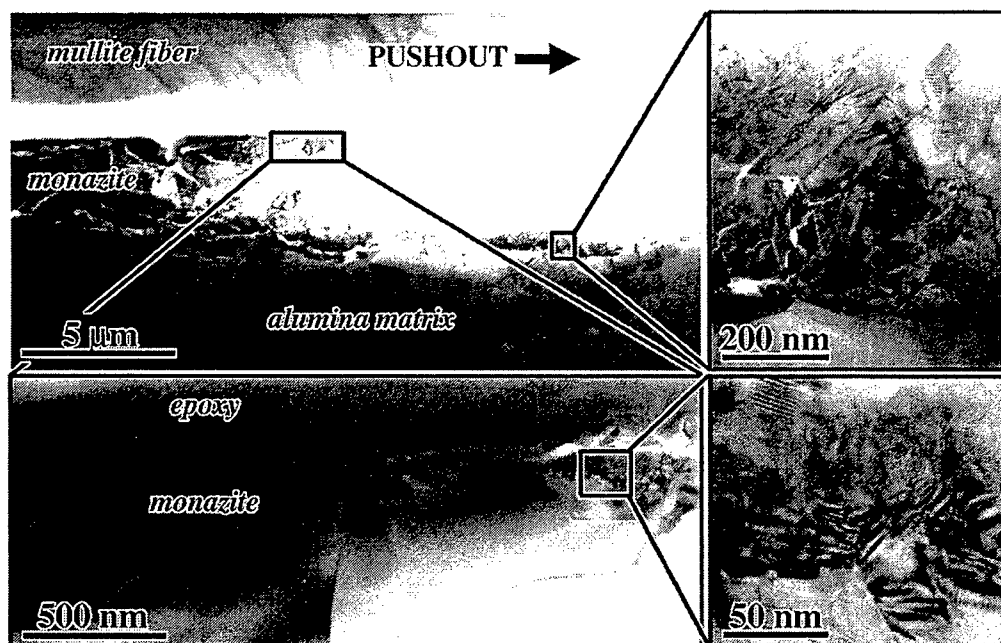
Fig. 10.   Monazite coating on mullite fiber: region thought to have experienced tension during fiber sliding (as in Region A, Fig. 9). Monazite next to fiber is mostly undamaged, but entire coating is cracked. Compression increases toward right side of micrograph.

material with high density of dislocations requires lattice diffusion for dislocation climb,[50] whereas recrystallization after amorphization by radiation damage does not require such diffusion. Nevertheless, the resistance of monazite to amorphization hints that solid-state processes in monazite are faster than those in many other ceramics, such as alumina and zircon, at similar homologous temperatures.[60] Independent measurements of nucleation, recrystallization, grain growth, and diffusion are needed to determine whether recrystallization of intensely deformed monazite might occur near room temperature.
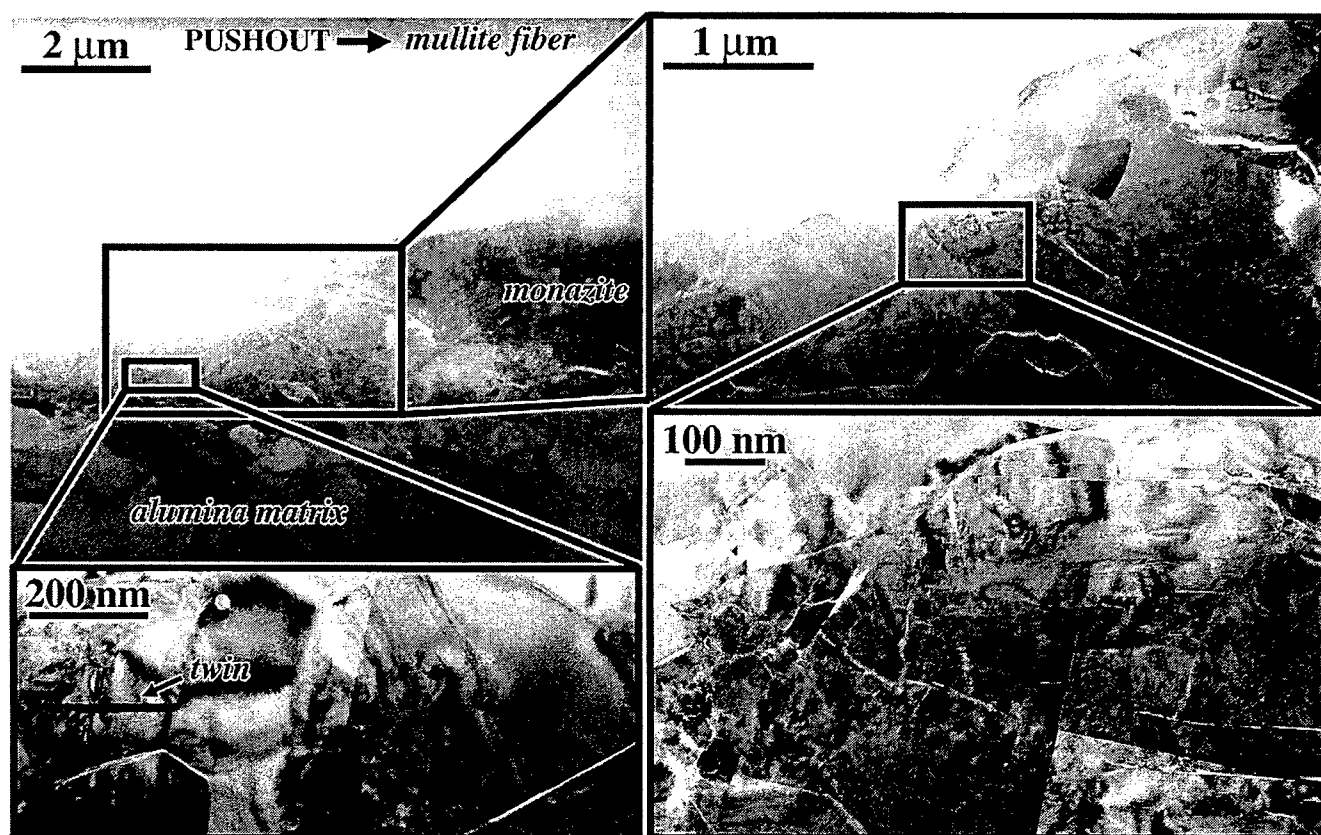
Fig. 11.   Monazite coating on mullite fiber: region thought to have experienced compression during fiber sliding (as in Region B, Fig. 9). Coating is heavily deformed through entire thickness, although with grain-to-grain variation. Large cracks tend to run NW–SE.

Table II. Misfit Strains and Stresses

	Value			
	Sapphire	Mullite	YAG/Al$_2$O$_3$	Al$_2$O$_3$/ZrO$_2$
Fiber radius (R/μm)	50	25	50	50
Microstructural roughness				
Amplitude, δr (μm)	0.05	0.05	0.2	0.2
Period, λ_r (μm)	2	2	1	1
$\delta r/R$	0.001	0.002	0.004	0.004
σ_r (MPa)[‡]	-200	-300	-770	-730
Fiber diameter fluctuation				
Amplitude, ΔR (μm)	0.5	2.5	0.5	1
Period, λ_R (μm)	500	100	1000	400
($\Delta R/R$) ($\pi z_{max}/\lambda_R$)[†]	0.0006	0.03	0.0003	0.0015
σ_R (MPa)[‡]	-120	-4500	-60	-270

[†]z_{max} is the maximum sliding displacement (~ 10 μm)
[‡]Nominal radial misfit stresses intended only as rough guide for comparisons: stresses calculated as in Table 1 but with radial misfit strains $\delta r/R$ and ($\Delta R/R$) ($\pi z_{max}/\lambda_R$), the latter being the maximum misfit strain for sinusoidal diameter fluctuation ($z_{max} \ll \lambda_R$).

V. Summary and Conclusions

La-monazite is compatible with mullite, YAG, ZrO$_2$, and Al$_2$O$_3$. The interfaces between La-monazite and these materials are sufficiently weak to allow debonding when a crack approaches the interface from within the monazite. This occurs even in the presence of substantial residual compressive stresses normal to the interface, as in the case of the mullite fiber in an alumina matrix.

All the monazite-coated fibers in this study (single crystal mullite and alumina, eutectic Al$_2$O$_3$/YAG, and Al$_2$O$_3$/ZrO$_2$) underwent sliding in single fiber pushout experiments. Sliding occurred along a single interfacial debond when the displacements were small and/or the fiber surfaces were relatively smooth. At larger displacements, the eutectic fibers, which had rougher interfaces than the single crystal fibers, caused extensive damage in the LaPO$_4$ coating adjacent to the fiber. The mullite fibers, which had smooth surfaces but large oscillations in diameter, caused deformation through the entire thickness of the coating in regions of large misfit strain. Damage mechanisms included fracture, dislocation plasticity, and occasional twinning. The fibers were undamaged, as might be expected given their higher hardnesses. The relative softness of La-monazite, resulting from its ability to deform plastically at low temperatures, may be critical for its use as a composite interface.

TEM observations showed densely packed fine crystallites of monazite in the most heavily deformed regions, resembling recrystallized microstructures. Several analyses indicated that significant frictional heating during sliding was unlikely unless stick-slip motion or cataclastic flow caused large increases in local sliding velocities and deformation rates. The detailed mechanisms responsible for this microstructure, which is unusual for such a refractory material at low temperature, have not been identified. However, a parallel exists in the recrystallization from radiation damage at much lower temperatures in La-monazite than in other minerals.

Appendix A

Estimates of Heating from Fiber Sliding

Several approaches, based on different assumptions about dissipation mechanisms, may be taken to estimate limits on local temperature rises during fiber sliding. Some results from these analyses are summarized as follows:

(1) Adiabatic Sliding

If we assume that the work done by sliding friction is dissipated entirely by uniform adiabatic heating in a zone of deformed monazite adjacent to the plane of sliding, the temperature rise is

$$\Delta T = \frac{\tau_s \delta}{\rho c_p h} \tag{A-1}$$

where τ_s is the sliding friction stress, δ is the sliding displacement, h is the thickness of the deformation zone, and ρ and c_p are the density and specific heat of the monazite. For the sliding experiment corresponding to Fig. 6, the measured parameters are $\tau_s \sim 200$ MPa, $\delta = 5$ μm and $h \sim 0.2$ μm. With $\rho = 5$ g/cm^3 and $c_p = 500$ J·(kg·K)$^{-1}$,[61] Eq. (A-1) gives $\Delta T = 2000$°C.

An alternative estimate based on incremental sliding of individual asperities, as depicted in Fig A1, gives the temperature rise as

$$\Delta T = \frac{H A_a}{\rho c_p A_b} \tag{A-2}$$

where H is the hardness of the monazite, A_a is the cross-sectional area of the asperity and A_b is the cross-sectional area of the plastic deformation zone created by the asperity as it slides (the sliding force acting on the asperity being set equal to HA_a). If we take H as the room temperature hardness of monazite (~ 5 GPa)[1] and $A_b/A_a \approx 2$ (from Fig. 6), Eq. (A-2) gives $\Delta T = 1000$°C.

Both of these estimates are subject to considerable uncertainty (a factor of ~ 2) associated with the parameters h and A_a/A_b as well as the assumption of uniform heating within the zone. Nevertheless, they indicate that large local temperature rises could occur if the sliding velocity is sufficiently large to cause adiabatic conditions.

(2) Estimated Sliding Velocity and Transient Heating Effects

The time in transient heat conduction problems always appears normalized by the characteristic time, τ:[62]

$$\tau = \frac{\rho c_p d^2}{k} \tag{A-3}$$

where k is the thermal conductivity and d is a characteristic diffusion distance. In the fiber sliding problem, d is the depth of the deformation zone and the conditions are close to adiabatic only if the time, t_h, taken to heat the deformation zone is small compared with τ. If we assume that heat is conducted only into the monazite (k ≈ 2 W·(m·K)$^{-1}$),[61] τ is $\sim 10^{-7}$ s for a zone of depth ~ 0.2 μm. The time t_h is given by $t_h = \delta/v$, where δ is the sliding distance and v is the sliding velocity.

Although the sliding velocity was not measured in the experiments described in Section II, a very conservative upper bound may be estimated. The experiments involved loading the indenter
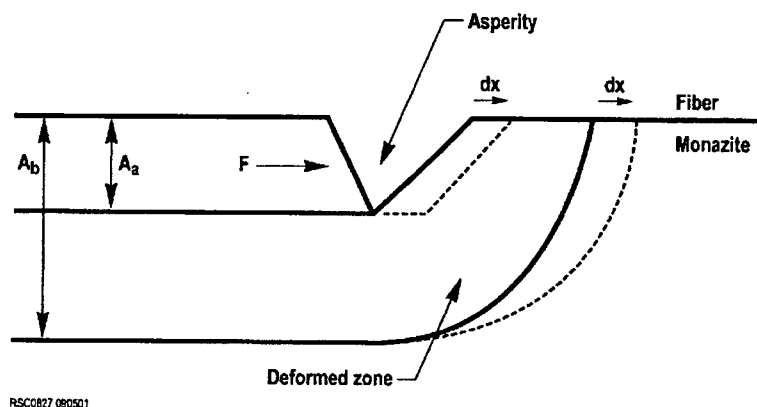
RSC0827 080501

Fig. A1. Schematic showing asperity sliding and associated deformation zone.

on the end of the fiber using a fixed weight lowered slowly (velocity $<10^{-4}$ m/s) by a viscous dashpot. When the interface debonded, the sliding fiber accelerated unstably until the indenter contacted the matrix. The magnitude of the acceleration was determined by the resultant force on the fiber (the difference between the combined weight of the loading mass, indenter, and fiber and the opposing forces due to sliding friction and the dash-pot). An upper bound for this acceleration, corresponding to zero resistance from sliding and the dashpot, is the gravitational acceleration, g. This acceleration acting over the measured sliding displacement (~5 μm) would result in a maximum velocity of 10^{-2} m/s. A less conservative overestimate obtained by assuming that the sliding friction remains constant during the test gives a value smaller by a factor of 15.

With the upper-bound velocity of 10^{-2} m/s and the sliding distance $\delta = 5$ μm for the average analysis of Eq. (A-1), the lower bound estimate for the heat input time is $t_h \sim 5 \times 10^{-4}$ s. This is more than three orders of magnitude larger than the value of τ estimated above, indicating that adiabatic conditions are not approached. For the asperity sliding analysis (Eq. (A-2)), the relevant sliding distance is smaller (equal to the dimensions of the asperity, ~0.5 μm) giving a smaller heat input time, although still far from adiabatic conditions ($t_h/\tau \approx 10^2$).

It is worth noting the role of asperity size in the above analysis. Because both d in Eq. (A-3) and the sliding distance δ that determines the sliding time (t_h) scale with the asperity size, the ratio t_h/τ increases with decreasing asperity size. Therefore, if the damage observed in Fig. 6 was caused by sequential sliding of asperities of various sizes, the conditions for the smaller asperities would have been further from adiabatic. Given the conservative nature of these estimates it appears unlikely that large temperature increases could have occurred in these experiments if sliding occurred uniformly.

(3) Frictional Sliding Analyses

In the literature on frictional sliding, the assumption is made that work done by frictional forces is dissipated as heat at the interface between the sliding surfaces.[52–54] Solutions for the interface temperature as a function of the sliding velocity are obtained from analysis of heat flow into the materials either side of the interface. Solutions are available at a macroscopic level (average) and at an asperity contact level for transient and steady-state conditions. These solutions can be written in the general form[54]

$$\Delta T = \left(\frac{F_s v}{A}\right)\left(\frac{k_1}{\ell_1} + \frac{k_2}{\ell_2}\right)^{-1} \tag{A-4}$$

where ΔT is the difference between the interface temperature and the remote temperature, F_s is the sliding force, v the velocity, A the contact area, k_1 and k_2 are the thermal conductivities of materials 1 and 2 either side of the interface, and l_1 and l_2 are functions of

the contact geometry, thermal diffusivities (α) and the time over which the heat is applied. A limitation of these models is that ΔT increases without limit as the sliding velocity increases (i.e., as adiabatic conditions are approached), a consequence of the assumption that the heat is dissipated at the interface rather than in a deformation zone of finite volume.

For the analysis of sliding asperities, a convenient solution for l_1 and l_2 is that of a gaussian heat source applied for a time t over a circular contact area of radius r_o:[54]

$$\ell = r_o\pi^{-1/2}\tan^{-1}\left(\frac{4t\alpha}{r_o^2}\right)^{1/2} \tag{A-5}$$

An upper bound for the sliding force on an asperity is given by taking the contact pressure equal to the hardness of the monazite and a friction coefficient of unity, so that $F_s/A = H$. For asperity contact times between the limits of $\sim r_o/v$ and δ/v, the temperature increase estimated from Eq. (A-4) for an Al_2O_3/YAG asperity with $r_0 = 0.2$ μm, $\alpha \approx 0.05$ cm²/s, $k \approx 20$ W·(m·K)$^{-1}$,[63] and other parameters as defined above is ~0.5°C. An alternative analysis based on the measured sliding force and uniform contact gave $\Delta T \approx 5$°C.

References

[1]P. E. D. Morgan and D. B. Marshall, "Ceramic Composites of Monazite and Alumina," *J. Am. Ceram. Soc.*, **78**, 1553–63 (1995).
[2]P. E. D. Morgan, D. B. Marshall, and R. M. Housley, "High Temperature Stability of Monazite–Alumina Composites," *Mater. Sci. Eng.*, *A*, **A195**, 215–22 (1995).
[3]D. B. Marshall, P. E. D. Morgan, R. M. Housley, and J. T. Cheung, "High Temperature Stability of the Al_2O_3–$LaPO_4$ System," *J. Am. Ceram. Soc.*, **81** [4] 951–56 (1998).
[4]D. B. Marshall, J. B. Davis, P. E. D. Morgan, and J. R. Porter, "Interface Materials for Damage-Tolerant Oxide Composites," *Key Eng. Mater.*, **127–131**, 27–36 (1997).
[5]J. B. Davis, D. B. Marshall, and P. E. D. Morgan, "Oxide Composites of Al_2O_3 and $LaPO_4$," *J. Eur. Ceram. Soc.*, **19**, 2421–26 (1999).
[6]J. B. Davis, D. B. Marshall, and P. E. D. Morgan, "Monazite Containing Oxide–Oxide Composites," *J. Eur. Ceram. Soc.*, **20** [5] 583–87 (2000).
[7]K. A. Keller, T.-I. Mah, E. E. Boakye, and T. A. Parthasarathy, "Gel-Casting and Reaction Bonding of Oxide–Oxide Minicomposites with Monazite Interphase," *Ceram. Eng. Sci. Proc.*, **21** [4] 525–34 (2000).
[8]T. A. Parthasarathy, E. Boakye, M. K. Cinibulk, and M. D. Perry, "Fabrication and Testing of Oxide/Oxide Microcomposites with Monazite and Hibonite as Interlayers," *J. Am. Ceram. Soc.*, **82** [12] 3575–83 (1999).
[9]S. M. Johnson, Y. Blum, C. Kanazawa, H.-J. Wu, J. R. Porter, P. E. D. Morgan, D. B. Marshall, and D. Wilson, "Processing and Properties of an Oxide/Oxide Composite," *Key Eng. Mater.*, **127–131**, 231–38 (1997).
[10]S. M. Johnson, Y. Blum, and C. H. Kanazawa, "Development and Properties of an Oxide Fiber–Oxide Matrix Composite," *Key. Eng. Mater.*, **164–165**, 85–90 (1999).
[11]K. A. Keller, T. Mah, T. A. Parthasarathy, E. E. Boakye, and M. Cinibulk, "Evaluation of All-Oxide Composites Based on Coated Nextel 610 and 650 Fibers," *Ceram. Eng. Sci. Proc.*, in press (2001).
[12]Y. Hikichi and T. Nomura, "Melting Temperatures of Monazite and Xenotime," *J. Am. Ceram. Soc.*, **70** [10] C-252–C-253 (1987).
[13]D. B. Marshall, P. E. D. Morgan, and R. M. Housley, "Debonding in Multilayered Composites of Zirconia and $LaPO_4$," *J. Am. Ceram. Soc.*, **80** [7] 1677–83 (1997).
[14]D.-H. Kuo and W. M. Kriven, "Characterization of Yttrium Phosphate and a Yttrium Phosphate/Yttrium Aluminate Laminate," *J. Am. Ceram. Soc.*, **78** [11] 3121–24 (1995).

[15]M. G. Cain, R. L. Cain, A. Tye, P. Rian, M. H. Lewis, and J. Gent, "Structure and Stability of Synthetic Interphases in CMCs," *Key Eng. Mater.*, 127–131, 37–49 (1997).

[16]D.-H. Kuo, W. M. Kriven, and T. J. Mackin, "Control of Interfacial Properties through Fiber Coatings: Monazite Coatings in Oxide–Oxide Composites," *J. Am. Ceram. Soc.*, 80 [12] 2987–96 (1997).

[17]R. J. Kerans and T. A. Parthasarathy, "Debond Crack Roughness, Interface Properties and Fiber Coating Design in Ceramic Composites," *Key Eng. Mater.*, 127–131, 51–62 (1977).

[18]A. Sayir, "Directional Solidification of Eutectic Ceramics"; pp. 197–211 in *Computer Aided Design of High Temperature Materials*. Edited by A. Pechenik, R. Kalia, and P. Vashishta. Oxford University Press, Oxford, U.K., 1999.

[19]A. Sayir and S. C. Farmer, "Directionally Solidified Mullite Fibers," *Mater. Res. Soc. Symp. Proc.*, 365, 11–21 (1995).

[20]A. Sayir and S. C. Farmer, "The Effect of the Microstructure on Mechanical Properties of Directionally Solidified $Al_2O_3/ZrO_2(Y_2O_3)$ Eutectic," *Acta Mater.*, 48 [18–19] 4691–97 (2000).

[21]A. Sayir and L. E. Matson, "Growth and Characterization of Directionally Solidified $Al_2O_3/Y_3Al_5O_{12}$ (YAG) Eutectic Fibers," *Proc. 2nd Ann. HITEMP Rev.*, 83, 1–14 (1991).

[22]T. A. Hahn, "Thermal Stress Relaxation due to Plastic Flow in the Fiber Coating of a Continuous Fiber Reinforced Composite," *J. Compos. Mater.*, 27 [16] 1545–77 (1993).

[23]W. M. Kriven, J. W. Palko, S. Sinogeikin, J. D. Bass, A. Sayir, G. Brunauer, H. Boysen, F. Frey, and J. Schneider, "High Temperature Single Crystal Properties of Mullite," *J. Eur. Ceram. Soc.*, 19, 2529–41 (1999).

[24]Y. S. Touloukian, R. K. Kirby, R. E. Taylor, and T. Y. R. Lee, *Thermal Expansion—Non-Metallic Solids*. New York, Plenum, 1977.

[25]S. Geller, G. P. Espinosa, and P. B. Crandall, "Thermal Expansion of Yttrium and Gadolinium Iron, Galluim and Aluminum Garnets," *J. Appl. Crystallogr.*, 2, 86–88 (1969).

[26]R. S. Hay, J. R. Welch, and M. K. Cinibulk, "TEM Specimen Preparation and Characterization of Ceramic Coatings on Fiber Tows," *Thin Solid Films*, 308–309, 389–92 (1997).

[27]M.-Y. He and J. W. Hutchinson, "Crack Deflection at an Interface between Dissimilar Materials," *Int. J. Solids Struct.*, 25, 1053–67 (1989).

[28]D. B. Marshall, J. B. Davis, P. E. D. Morgan, J. R. Waldrop, and J. P. Porter, "Properties of La-Monazite as an Interphase in Oxide Composites," *Z. Metallkd.*, 90 [12] 1048–52 (1999).

[29]D. B. Marshall, J. R. Waldrop, and P. E. D. Morgan, "Thermal Grooving at the Interface between Alumina and Monazite," *Acta Mater.*, 48, 4471–74 (2000).

[30]M. S. Paterson, *Experimental Rock Deformation—The Brittle Field*; p. 254. Springer-Verlag, Heidelberg, New York, and Berlin, 1978.

[31]R. S. Hay, "Monazite and Scheelite Deformation Mechanisms," *Ceram. Eng. Sci. Proc.*, 21 [4] 203–28 (2000).

[32]M.-Y. He, A. G. Evans, and J. W. Hutchinson, "Crack Deflection at an Interface Between Dissimilar Elastic Materials: Role of Residual Stresses," *Int. J. Solids Struct.*, 31 [24] 3443–55 (1994).

[33]R. S. Hay, E. Boakeye, M. D. Petry, Y. Berta, K. Von Lehmden, and J. Welch, "Grain Growth and Tensile Strength of 3M Nextel 720™ after Thermal Exposure," *Ceram. Eng. Sci. Proc.*, 20 [3] 165–72 (1999).

[34]D. M. Wilson and L. R. Visser, "Nextel 650 Ceramic Oxide Fiber: New Alumina-based Fiber for High Temperature Composite Reinforcement," *Ceram. Eng. Sci. Proc.*, 21 [4] 363–73 (2000).

[35]A. Romoscanu, "Topography Characterization of Alumina-Mullite Fibers Using Atomic Force Microscopy and Relationship to Mechanical Properties," Masters Thesis. University of Pennsylvania, Philadelphia, PA (1998).

[36]L. E. Matson and N. Hecht, "Microstructural Stability and Mechanical Properties of Directionally Solidified Alumina/YAG Eutectic Monofilaments," *J. Eur. Ceram. Soc.*, 19, 2487–503 (1999).

[37]J. B. Davis, D. B. Marshall, P. E. D. Morgan, and R. M. Housley, "Machinable Ceramics Containing Rare-Earth Phosphates," *J. Am. Ceram. Soc.*, 81 [8] 2169–75 (1998).

[38]B. J. Hockey, "Plastic Deformation of Aluminum Oxide by Indentation and Abrasion," *J. Am. Ceram. Soc.*, 54 [5] 223–31 (1971).

[39]A. H. Heuer, "Deformation Twinning in Corundum," *Philos. Mag. A*, 13 [122] 379–93 (1966).

[40]R. M. Cannon, "Structure and Properties of MgO and Al_2O_3"; pp 818–38 in Advances in Ceramics, Vol. 10. Edited by W. D. Kingery. Columbus, Ohio, American Ceramic Society, 1984.

[41]H. M. Chan and B. R. Lawn, "Indentation Deformation and Fracture of Sapphire," *J. Am. Ceram. Soc.*, 71 [1] 29–35 (1988).

[42]K. P. D. Lagerlof, A. H. Heuer, J. Castaing, J. P. Riviere, and T. E. Mitchell, "Slip and Twinning in Sapphire (α-Al_2O_3)," *J. Am. Ceram. Soc.*, 77 [2] 385–97 (1994).

[43]S. B. Toh and R. McPherson, "Plastic Deformation during the Abrasive Wear of Ceramics"; pp. 723–32 in *Deformation of Ceramic Materials*, Vol. 2. Edited by R. E. Tressler and R. C. Bradt. Plenum Press, New York and London, 1984.

[44]I. J. McColm, *Ceramic Hardness*; p. 324. Plenum Press, New York, 1990.

[45]I. A. Cutter and R. McPherson, "Plastic Deformation of Alumina during Abrasion," *J. Am. Ceram. Soc.*, 56, 266 (1973).

[46]S.-J. Cho, H. Moon, B. J. Hockey, and S. M. Hsu, "The Transition from Mild to Severe Wear in Alumina during Sliding," *Acta Metall. Mater.*, 40 [1] 185–92 (1992).

[47]B. J. Inkson, "Dislocations and Twinning Activated by the Abrasion of Alumina," *Acta Mater.*, 48, 1883–95 (2000).

[48]D. Kuhlmann-Wilsdorf, "What Role for Contact Spots and Dislocations in Friction and Wear," *Wear*, 200, 8–29 (1996).

[49]H. Kakisawa and Y. Kagawa, "Effect of Abrasive Wear on Interfacial Shear Sliding Resistance in SiC Fiber-Reinforced Al_2O_3 Matrix Composite," *Ceram. Eng. Sci. Proc.*, 18 [3] 757–62 (1997).

[50]F. J. Humphreys and M. Hatherly, *Recrystallization and Related Annealing Phenomena*, 1st Ed.; p. 497. Pergamon, 1996.

[51]B. J. Hockey, "Observations by Transmission Electron Microscopy of the Subsurface Damage Produced in Aluminum Oxide by Mechanical Polishing and Abrasion," *Proc. Br. Ceram. Soc.*, 20, 95–115 (1972).

[52]F. P. Bowden and D. Tabor, *Friction and Lubrication of Solids, Parts I and II*. Clarendon Press, Oxford, U. K., 1964.

[53]J. C. Jaeger, "Moving Sources of Heat and Temperature at Sliding Contacts," *J. Proc. R. Soc. NSW*, 76, 203 (1942).

[54]M. F. Ashby, J. Abulawi, and H. S. Kong, "Temperature Maps for Frictional Heating in Dry Sliding," *Tribol. Trans.*, 34 [4] 577–87 (1991).

[55]S. Brown, "Frictional Heating on Faults: Stable Sliding versus Stick-Slip," *J. Geophys. Res.*, 103 [B4] 7413–20 (1998).

[56]F. G. Karioris, K. A. Gowda, and L. Cartz, "Heavy Ion Bombardment of Monoclinic $ThSiO_4$, ThO_2, and Monazite," *Radiat. Eff. Lett. Sect.*, 58, 1–3 (1981).

[57]T. C. Ehlert, K. A. Gowda, F. G. Karioris, and L. Cartz, "Differential Scanning Calorimetry of Heavy Ion Bombarded Synthetic Monazite," *Radiat. Eff.*, 70, 173–81 (1983).

[58]L. A. Boatner and B. C. Sales, "Monazite"; Ch. 8 in *Radioactive Waste Forms for the Future*. Edited by W. Lutze and R. C. Ewing. North-Holland, New York, 1988.

[59]A. Meldrum, L. A. Boatner, and R. C. Ewing, "Electron-Irradiation-Induced Nucleation and Growth in Amorphous $LaPO_4$, $ScPO_4$, and Zircon," *J. Mater. Res.*, 12 [7] 1816–27 (1997).

[60]A. Meldrum, L. A. Boatner, and R. C. Ewing, "A Comparison of Radiation Effects in Crystalline $ABO4$-type Phosphates and Silicates," *Mineral. Mag.*, 64 [2] 185–94 (2000).

[61]Y. Hikichi, T. Nomura, Y. Tanimura, and S. Suzuki, "Sintering and Properties of Monazite-type $CePO_4$," *J. Am. Ceram. Soc.*, 73 [12] 3594–96 (1990).

[62]F. P. Incropera and D. P. DeWitt, *Introduction to Heat Transfer*. New York, Wiley, 1996.

[63]Y. S. Touloukian, R. W. Powell, C. Y. Ho, and P. G. Klemens, *Thermal Conductivity—Non-Metallic Solids*. Plenum New York, 1970. □

Section 7

Deformation Twinning in Monazite

by R. S. Hay and D. B. Marshall,

Deformation twinning in monazite

R.S. Hay [a,*], D.B. Marshall [b]

[a] Air Force Research Laboratory, Materials and Manufacturing Directorate, WPAFB, OH, USA
[b] Rockwell Scientific Co., Thousand Oaks, CA, USA

Abstract

Polycrystalline monazite ($LaPO_4$) was deformed at room temperature by a spherical indenter. Deformation twins were identified by TEM in 70 grains. Five twin planes were found: (1 0 0) was by far the most common; (0 0 1) and (1 2 0) were less common; (1 2 $\bar{2}$) was rare, and kinks in (1 2 0) twins were identified as irrational '(4 8 3)' twin planes. The twinning modes on these planes were inferred from the expression of twinning shear at free surfaces, predictions of classical deformation twinning theory, and various considerations of twin morphology and crystal structure. Atomic shuffle calculations that allow formation of either a glide plane or a mirror plane at the twin interface were used to analyze twin modes. The inferred twin modes all have small atomic shuffles. For (0 0 1) twins, the smallest shuffles were obtained with a glide plane at the interface, with displacement vector $\mathbf{R} = \frac{1}{2}[010]$. The results do not uniquely define a twin mode on (1 0 0), leaving open the possibility of more than one mode operating on this plane. Factors that may determine the operative deformation twinning modes are discussed. Crystal structure considerations suggest that the relative abundance of twinning modes may correlate with low shear modulus on the twin plane in the direction of twinning shear, and with a possible low-energy interface structure consisting of a layer of xenotime of one half-unit-cell thickness that could form at (1 0 0) and (0 0 1) twins. The three most common twins have low strains to low Σ coincidence site lattices (CSLs).
Published by Elsevier Ltd on behalf of Acta Materialia Inc.

Keywords: Crystalline oxides; Transmission electron microscopy; Twinning; Modeling; Deformation structure; Monazite

1. Introduction

1.1. Deformation twinning background

Twinning is a deformation mechanism that can impart some ductility to complex oxides. However, detailed knowledge of twinning modes in complex and low symmetry materials is limited [1,2]. We report observations of deformation twinning in monazite (monoclinic $LaPO_4$) induced by a spherical indenter at room temperature.

TEM observations provide information on twin planes and orientation relationships. However, they usually do not define the shear direction, which is needed for a complete specification of the twin mode. To determine twin modes, we use additional

* Corresponding author. Tel.: +1-937-2559825; fax: +1-937-6564296.
E-mail address: Randall.Hay@wpafb.af.mil (R.S. Hay).

observations of the expression of twinning shear at free surfaces along with other considerations of crystal structure, classical deformation twinning theory [1,3] (calculated twinning shear and shuffle displacements), and special boundary structures, such as those predicted from coincidence site lattice (CSL) theory [4–6]. In a companion paper, twin modes in a kinked monazite twin are inferred by other methods [7].

Twins are identified with the twin plane ($\mathbf{K}_1$). Twin modes are labeled using conventions reviewed by Christian and Mahajan [1] and Crocker [8], which use $\mathbf{K}_1$, $\mathbf{K}_2$ (the other undistorted plane), η_1 (the shear direction), and η_2 (the direction in $\mathbf{K}_2$ normal to the intersection of $\mathbf{K}_1$ and $\mathbf{K}_2$) (Fig. 1). Since only two of these parameters are independent, any two of them can be used to specify the twin mode. Three types of classical twins can be distinguished: type I twins, in which the twin and matrix are related by reflection across the twin plane or a 180° rotation around the normal to the twin plane, with $\mathbf{K}_1$ and η_2 being rational and $\mathbf{K}_2$ and η_1 irrational; type II twins which are related by rotation of 180° around the shear direction or a reflection in the plane normal to the shear direction, with $\mathbf{K}_1$ and η_2 being irrational and $\mathbf{K}_2$ and η_1 rational; and compound twins, which have $\mathbf{K}_1$, η_2, $\mathbf{K}_2$, and η_1 all rational, in which case all reflection and rotation operations are equivalent. For centrosymmetric crystals like

Fig. 1. Twin mode conventions: the four twinning elements and the shear plane.

monazite, the reflection and 180° rotation operation for both type I and type II twins are equivalent [1,3,9]. The twins are labeled using pairs of rational parameters: $(\mathbf{K}_1)[\eta_2]_I$ for type I; $(\mathbf{K}_2)[\eta_1]_{II}$ for type II; and $(\mathbf{K}_1)[\eta_2]_C$ for compound twins. The plane containing η_1 and η_2 is the shear plane. The shear strain, s, is equal to $2\tan(\theta/2)$, where θ is the angular twinning shear, and $\theta/2$ is the angle between $\mathbf{K}_1$ and η_2 or $\mathbf{K}_2$ and η_1 (Fig. 1). Irrational indices are denoted by the closest rational indices using the notation '[ ]' or '( )'.

1.2. Monazite background

Monazite has recently received attention for use in structural ceramics that rely on its unusual combination of properties: high temperature stability (melting point 2072 °C), compatibility with common structural oxide ceramics [10–12], relatively low hardness (5 GPa [10], Moh's hardness of 5.5 [13]), and weak bonding with other oxide ceramics [10]. The low hardness and weak bonding are especially important for machinable ceramics [14], where they enable material removal, and for fiber reinforced composites, where they allow crack deflection and fiber pullout, without the problem of oxidation experienced by the more commonly used graphitic carbon and BN interfaces.

A soft or compliant fiber coating aids the pullout of fibers in a ceramic composite by accommodating mismatch strains from irregularities on the fiber surface [15]. Although monazite is relatively soft for a refractory material, it is not as soft as graphitic carbon or BN. Consequently, the fiber pushout stresses for monazite coated fibers are higher (~150–200 MPa) [10] than for carbon and BN coated fibers (~2–20 MPa) [16,17]. Nevertheless, there is convincing evidence for crack deflection and pullout of monazite coated fibers [10,18,22], accompanied by deformation of the coating.

Monazite deformation mechanisms have not been studied in detail. Cleavage and twinning on (1 0 0) and (0 0 1) have been reported in the mineralogical literature [23], although it is not known whether the twins were formed by deformation or during crystal growth. Studies of deformation caused by spherical indentation of polycrystalline monazite and monazite/oxide mixtures have shown
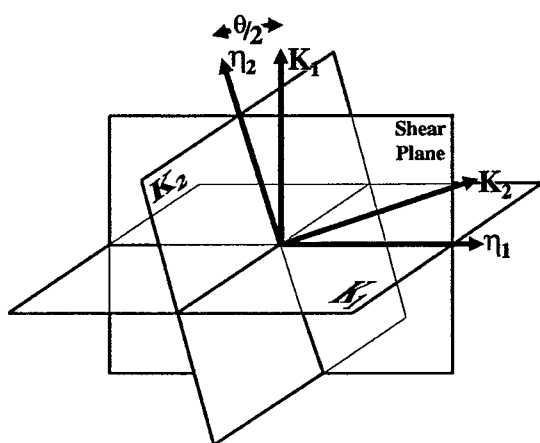
evidence for plastic deformation at room temperature. A preliminary report has shown both slip and twinning [24]. Extensive deformation involving slip and twinning has also been observed in monazite fiber coatings after fiber push-out at room temperature [25].

Monazite is monoclinic, with space group $P2_1/n$ and lattice parameters $a = 0.6825$ nm, $b = 0.7057$ nm, $c = 0.6482$ nm, and $\beta = 103.21°$ [26]. An equivalent description consistent with current crystallographic conventions [27] is space group $P2_1/c$ with lattice parameters $a' = -c = 0.6482$ nm, $b' = b = 0.7057$ nm, $c' = (a + c) = 0.8269$ nm, and $\beta = 126.53°$. Historically, the $P2_1/n$ space group has been used for monazite. Since this space group gives a simpler description of the observed twins, it will be used here.

2. Experiments

Monazite powder was hot pressed to near full density with grain size ~5–20 μm (and occasional grains exceeding 50 μm). The hot-pressed material was indented at room temperature with a 3 mm tungsten carbide ball using 20 kg load. TEM samples were prepared from regions surrounding five indentations by tripod polishing back to the indented surface, mounting the polished slices (5–10 μm thickness) on copper grids, and ion-milling in a Gatan Precision Ion Polishing System (Model 691) at 4.5 kV. Optical microscopy in polarized transmitted light was done prior to ion-milling. TEM samples were not carbon coated. Further details of sample preparation are described elsewhere [28].

The samples were observed using a Phillips CM200 TEM with a field emission gun operating at 200 kV. A double-tilt holder was used to orient the samples so that twin boundaries were edge-on and the same low-index zone was present for both the matrix and twin. In this orientation, the twin boundary plane could be identified. A similar method was used to identify cleavage planes. Since good two-beam imaging conditions are difficult to achieve with large lattice-parameter materials like monazite, zone-axis diffraction conditions were used for low magnification images. Corresponding

selected-area diffraction patterns from regions including both twins and matrix are included with most images. TEM negatives were digitized in a Leafscan 45 and measurements were made from the digital images. Distortion introduced into the digitized images was calibrated and corrected when necessary. This distortion was responsible for earlier confusion about whether some twins may have been martensitic phase transformations [24]. After correction for distortion during digitization, it was clear that only twins were present.

3. Results

Indentation of the monazite with the WC ball left permanent impressions similar to those produced in metallic or "quasi-plastic" materials [14,29,30]. Twinning was not visible optically in polarized transmitted light, although twins of sufficient width for optical observation were observed in other samples [14]. Extensive microcracking and dislocation plasticity were observed beneath the center of the indent, but twinning was rare. Towards the sides of indents, twinning was more common, with twins being in, at most, one out of every three grains.

When TEM sections were very thin over a very large area and copper from the TEM grid was far away, monazite would sublime under the electron beam when conditions for bright illumination at moderate (~100k×) and higher magnification were used. We do not know if other refractory oxides behave in a similar way under the high beam intensity and high vacuum of a field emission gun TEM. There was no other beam damage.

Twinning was much less common than slip, although in some favorably oriented grains, it was the dominant deformation mechanism. The abundance of twinning in a particular grain varied from one or two small isolated lamellae to multiple twinning throughout the grain (Fig. 2). Five different twin planes (K_1) were identified in 70 different monazite grains. Since twins, or any other evidence of deformation, were not observed in material remote from the indentations, all twins are inferred to be deformation twins and not growth twins. Twin intersections were not observed. Microcrack-
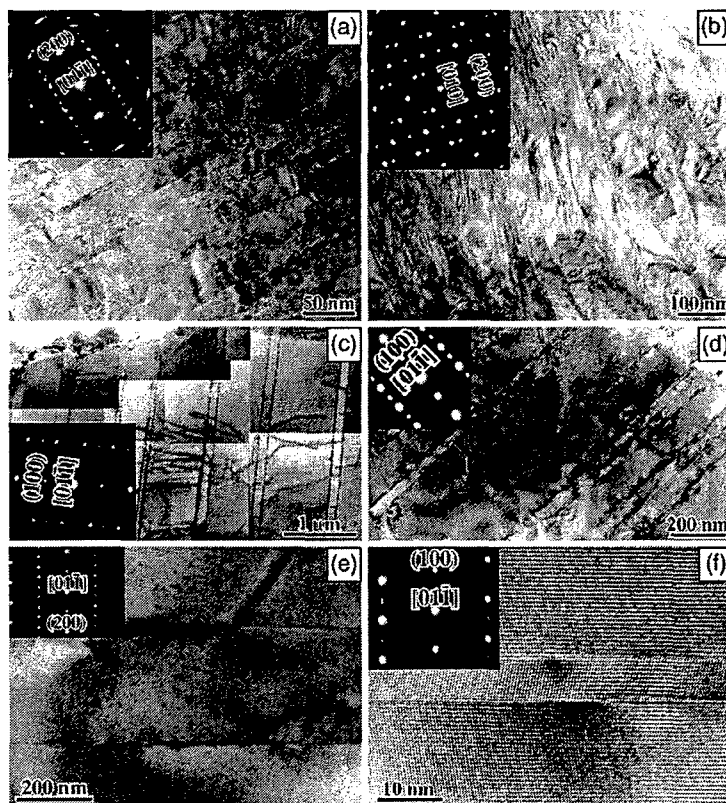
Fig. 2. (1 0 0) Twins with a variety of morphologies. (a) Narrow lens shaped twins completely fill the grain along with intense deformation by dislocation slip. (b) Lens shaped twins; slightly lower twin density and deformation by dislocation slip than (a). (c) Thicker, plate shaped twins with moderate deformation by dislocation slip. (d) Narrow lens shaped twins, little deformation by dislocation slip. (e) Thick, plate shaped twin; a few dislocations impinge the boundary. (f) A very narrow, planar twin.

ing by cleavage on (1 0 0) and (0 0 1) was abundant, consistent with the mineralogical literature [23]. Cleavage on (0 1 0), (0 1 1), (1 1 0), and (1 2 0) was also observed.

3.1. (1 0 0) Twins

These twins were by far the most common, which is consistent with the geological abundance (although we do not know whether the geological twins were formed by growth or deformation) [23]. They were observed in 58 different grains along four different imaging zones: [0 1 1], [0 1 0], [0 0 1], and [0 1 2]. Some thick twins had (1 0 0) cleavage cracks along one twin plane. Some grains were so heavily deformed by twinning and slip that

sharp electron diffraction patterns could not be obtained (Fig. 2a,b). In other grains, only thin isolated twins were present, with little evidence of slip (Fig. 2e,f). Most grains were between these two extremes, with several twins, and moderate evidence of slip (Fig. 2c,d).

The (1 0 0) twins had two distinct morphologies. There were many thin twins (Fig. 2f). Some were lenticular (Fig. 2d), with steps on the twin boundary. Thicker twins were less abundant and planar, often nearly atomically flat over distances of several microns (Fig. 2e). Average twin widths in a grain had a bimodal log-normal distribution in the 58 grains in which these twins were observed, with maxima at 18 and 56 nm (Fig. 3), and with ~70% in the smaller distribution and ~30% in the larger.
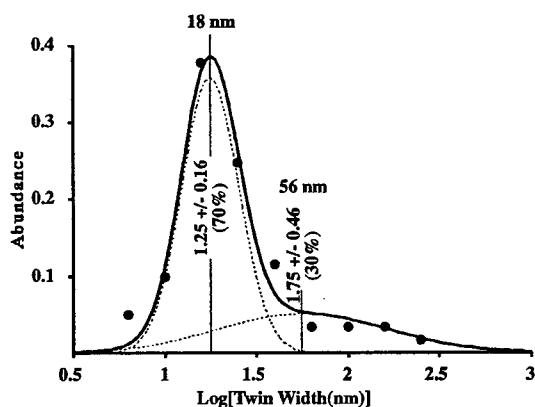
Fig. 3. Bimodal log-normal distribution of grains (based on 58 observations) with (1 0 0) twins of different widths. When more than one twin was in a grain, the average of the widths was used.

Wider twins were usually in grains with little evidence of slip, while narrower twins were often, but not always, in grains heavily deformed by slip.

In a few images, the twin deformation could be observed where twins intersected free surfaces (e.g., cracks at grain boundaries (Fig. 4)). These images allow measurement of the projected shear angle (θ_p) along the beam direction: values of 28°, 18°, and 8° ($\pm\sim5°$) were observed along the [0 1 0], [0 1 1], and [0 1 2] imaging zones, respectively. Since the samples were often tilted ~10° for observation along these zones, θ_p may be slightly distorted, but not by more than a few percent.

3.2. (0 0 1) Twins

(0 0 1) twins were observed in five different grains along four imaging zones: [2 1 0], [1 1 0], [0 1 0], and [1 0 0]. One twin was observed along two different zones (Fig. 5). These twins were thicker than (1 0 0) twins, averaging ~140 nm, with the smallest being 30 nm and the largest 340 nm. Lenticular twins were only observed in one grain. The remainder were flat-sided and relatively free of boundary defects. Occasionally, (0 0 1) cleavage cracks were observed along the twin plane. There was moderate density of dislocations in grains containing these twins. Only one grain with (0 0 1)
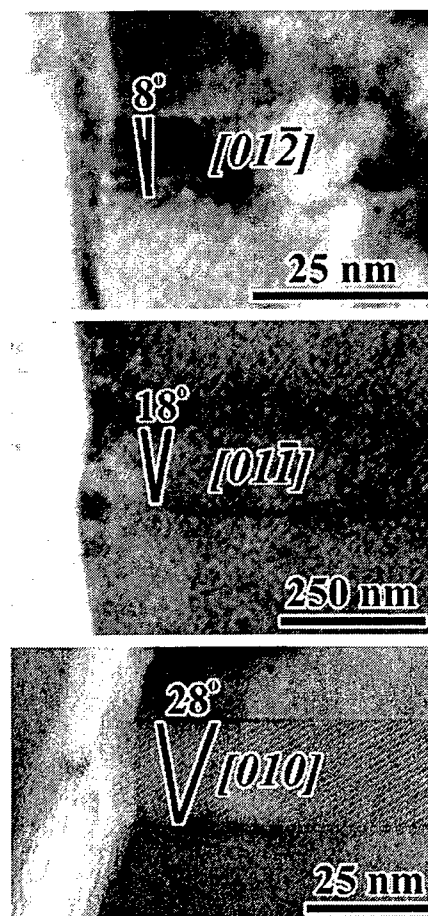
Fig. 4. Shear projection (θ_p) of (1 0 0) twins along different imaging zones.

twins was severely plastically deformed. In all five grains, the twins were widely spaced.

3.3. (1 2 0) Twins and kinks

(1 2 0) twins were observed in five different grains along four different zones: [0 0 1], [2 $\bar{1}$ 1], [2 $\bar{1}$ 0], and [4 $\bar{2}$ 3]. These twins were narrow, averaging about 28 nm, the widest being 42 nm. Three were flat sided and two were lenticular. One (flat sided) was cracked on one side, which shows that (1 2 0) is a cleavage plane. In grains containing these twins, there was usually little evidence
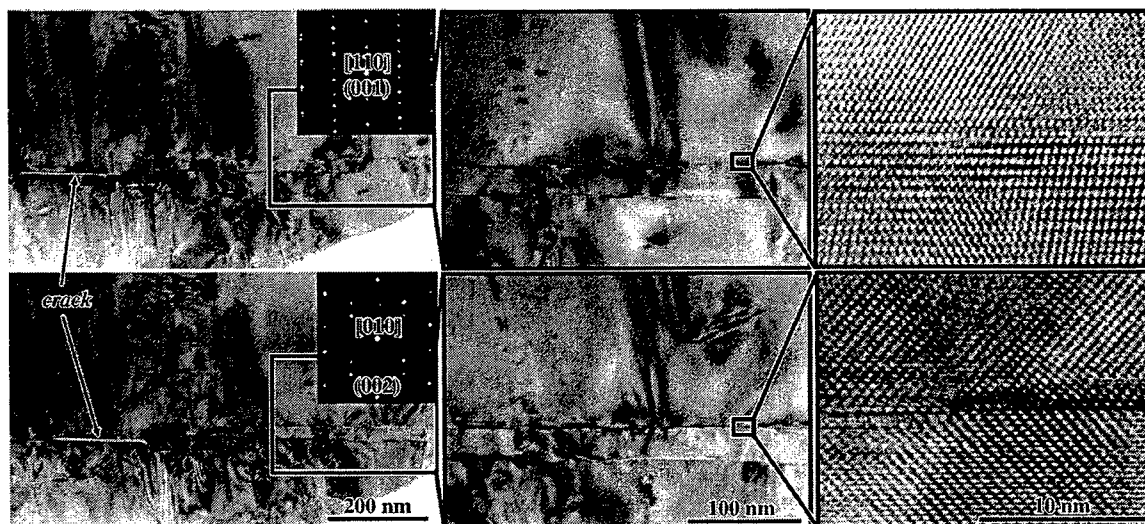
Fig. 5. The same area of an (0 0 1) twin observed down both the [1 1 0] and [0 1 0] zone axis.

of dislocation slip. In two grains, these twins were kinked along a plane of somewhat variable orientation, but close to (1 2 1) (Fig. 6). Analysis discussed later, and in a companion paper [7], suggests that this may be a type II twin with an irrational '(4 8 3)' twin plane. Unusual features of these twins are discussed in more detail in the companion paper [7].

3.4. (1 2 $\bar{2}$) Twins

Twins on (1 2 $\bar{2}$) were observed in two grains along the [2 $\bar{1}$ 0] and [2 0 1] imaging zones. Both were lens shaped. The lens shape was more pronounced than in (1 0 0) twins. One grain was heavily deformed by dislocation slip, while the other was not (Fig. 7). One twin had an indentation similar to that observed for (1 2 0) twins (Fig. 7).

In one grain imaged along [2 $\bar{1}$ 0], the twin terminated at a crack, which was planar and close to (1 2 0) in the matrix, suggesting cleavage. The projected shear angle (θ_p) at this crack was negligibly small (Fig. 7), implying that either the twin shear is very small, or the shear direction (η_1) is very close to [2 $\bar{1}$ 0].

4. Analysis and discussion

The TEM observations defined five deformation twin planes (K_1) and corresponding orientation relationships for monazite. Each of these twins could in principle be produced by many different deformation twin modes, which cannot be distinguished by electron diffraction patterns. Observations of projected shear angles (θ_p) combined with K_1 can be used to help identify twin modes [2]. There are also empirically based selection rules for the prediction of twin modes.

Deformation twin mode selection criteria have been empirically deduced in the classical theory of deformation twinning [1,3]. These selection rules are: (i) the twinning shear (θ) is small, (ii) the atomic shuffles needed to complete the twin after twinning shear are of small magnitude (δ), (iii) the periodicity of the shuffles (λ) is small, and (iv) if the shuffles are large, shuffle directions are close to parallel to η_1 [1,3,8]. For metal systems with few atoms per unit cell and non-directional bonding, shuffles, if required, are often represented by a single parameter, such as the average shuffle distance divided by the nearest neighbor distance [31,32]. However, for more complex crystal struc-
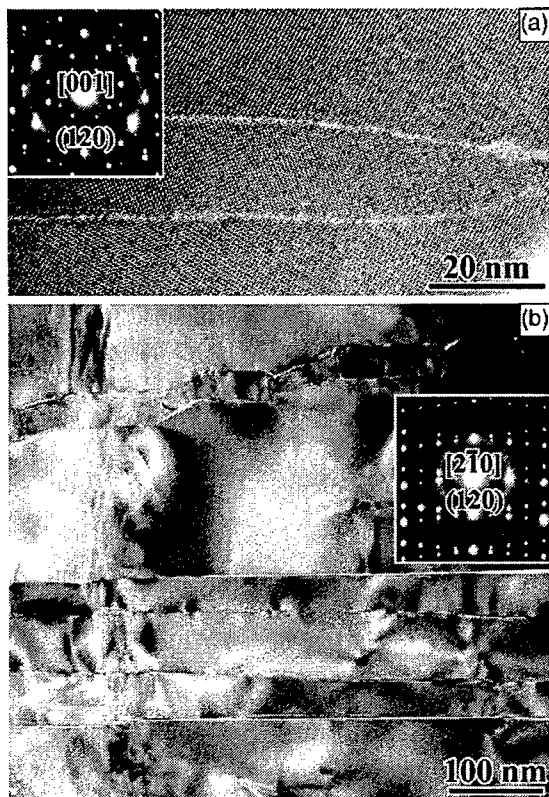
Fig. 6. (1 2 0) Twins. (a) HRTEM image along [0 0 1] zone showing reflection across (1 2 0). (b) Three parallel (1 2 0) twins; the upper twin is kinked along '(4 8 3)'.

Fig. 7. (1 2 2̄) Twins viewed along [2 1̄ 0] and [2 0 1]. In the upper micrograph, the twin terminates at a crack. Note the lack of shear projection along this crack.

tures such as monazite (24 atoms per unit cell) with strongly directional bonding, account must be taken of the relative bond stiffnesses and orientations as well as the shuffle magnitudes.

The fraction of parent lattice points carried to twin lattice sites by the twin shear is $1/q$, where $q = K_1 \cdot \eta_2$ for type I twins and $K_2 \cdot \eta_1$ for type II twins [1,3,8]. The periodicity of the shuffling (λ) is equal to $1/2q$ when q is even, and q when q is odd [1,3,9]. For a given twin plane, as λ becomes arbitrarily large, it is possible to find η_2 for a twin mode on that plane with θ arbitrarily small [3]. Favored modes are those which have both small shear and simple shuffle mechanisms (small θ and λ). Therefore, large values of either θ or λ were not considered when assessing potential twin modes.

For monazite, each P atom is bonded to four O atoms, while each La atom is bonded to nine O atoms. The PO_4 tetrahedra are isolated, connected to each other only by the LaO_9 polyhedra, which share edges and corners with each other, as well as with PO_4 tetrahedra (each O atom is bonded to one P atom and two or three La atoms). The PO_4 tetrahedra are smaller and more tightly bound than the LaO_9 polyhedra. This difference is reflected in the bond length distributions for the two polyhedra: P–O bond lengths vary between 0.1524 and 0.1540 nm, whereas La–O bond lengths vary between 0.250 and 0.277 nm. Thus, as well as being longer, the La–O bonds have much greater variability in length (by an order of magnitude). This suggests that any bond breaking needed during twinning would occur at La–O bonds, and that the PO_4 tetrahedra are relatively rigid, being connected through more flexible LaO_9 polyhedra. In this case, the O atom shuffles can be calculated from the sum of displacements due to translation and rotation of the PO_4 tetrahedra.

Shuffle displacements (δ) for PO_4 tetrahedra and

La atoms and rotations (ϕ) for PO_4 tetrahedra were calculated for all possible type I, type II, and compound monazite twin modes with $q \leq 4$, indices $\leq$ 4, and $\theta < 65°$. Details are given in Appendix A. The calculations allow shuffles out of the plane of shear, and the possibility of forming either a glide plane or a mirror plane at the twin interface for type I twins, or at the plane normal to η_1 for type II twins. Comparisons between twin modes were then made using λ and the maximum values of δ and ϕ for each mode, with maximum δ considered for La atoms and PO_4 tetrahedra together and separately. The different parameters for each mode are distinguished by subscripts and superscripts (eg., ϕ_{mx}, δ_{mx}^P, δ_{mx}^{La}, δ_{mx}^{LaP}, where δ_{mx}^{LaP} is the largest shuffle of all La atoms and PO_4 tetrahedra).

4.1. (1 0 0) Twins

Possible twin modes for (1 0 0) are listed in Table 1, along with calculated shuffle parameters and projected shear angles, θ_p, for the imaging zones <0 1 0>, <0 1 1>, and <0 1 2>, corresponding to the observations described in Section 3.1. Only one mode, (1 0 0)[1 0 0]$_C$, had θ_p within 5° of the observations for all three imaging zones (Fig. 4). If we assume that only one mode operates on (1 0 0), then all other modes are ruled out. This mode also has $\lambda = 1$, the lowest value of the shuffle parameter δ_{mx}^{LaP}, and the third smallest shear (θ). If we allow the possibility of more than one twin mode on (1 0 0), then there are three other reasonable modes that have small δ_{mx}^{LaP}, $\lambda = 1$, and θ_p matching observations for two out of the three zones: (1 0 0)[2 1 0]$_I$, (1 0 0)[2 1 1]$_I$, and (1 0 0)[2 0 1]$_C$. The (1 0 0)[2 1 0]$_I$ mode has significantly smaller ϕ_{mx} than the other two, whereas the (1 0 0)[2 0 1]$_C$ mode has much smaller shear. It may be possible that the bimodal distribution in (1 0 0) twin widths (Fig. 3) is due to the operation of more than one twin mode on (1 0 0).

All other modes in Table 1 have $\lambda = 2$ or 3 and much larger δ_{mx}^{LaP}. Most values of θ_p for these modes do not match observations. Note that very low shear alone does not appear to be a deciding factor in mode selection; the mode with by far the

Table 1
Calculated shuffle parameters and projected shear angles, θ_p, along directions indicated for possible (1 0 0) twin modes with $\theta <$ 65° and $q \leq 4$. Bold values of θ_p are those that match observations within 5°

| Mode		(Å)		(°)		θ_p (°)				
η_2	λ	δ_{mx}^{La}	δ_{mx}^P	ϕ_{mx}	θ	[0 1 0]	[0 1 1]	[0 Ī 1]	[0 1 2]	[0 Ī 2]
[1 0 0]	1	0.4	0.7	39	26	**26**	**20**	**20**	**13**	**13**
[2 1 0]	1	0.8	1.1	7	60	**26**	56	**21**	60	39
[2 0 1]	1	1.1	1.1	51	28	**28**	**21**	**21**	14	14
[2 1 1]	1	1.1	1.2	90	61	**28**	**20**	57	38	61
[3 1 0]	3	1.5	1.7	7	46	26	45	8	46	22
[3 1 1]	3	1.8	1.9	90	40	10	**20**	34	30	39
[3 1 2]	3	1.8	1.7	90	57	45	8	57	**13**	54
[4 0 Ī]	2	2.0	2.1	51	40	40	28	1	39	**13**
[4 2 1]	2	2.1	2.0	90	56	1	39	40	50	50
[4 1 3]	2	2.1	2.0	90	59	53	**21**	57	1	50
[4 0 1]	2	2.1	2.0	51	1	1	1	1	1	1
[4 0 3]	2	2.2	2.2	51	51	51	39	39	26	26
[4 1 1]	2	2.2	2.2	90	53	53	40	40	27	27
[4 1 0]	2	2.2	2.1	90	39	**26**	39	1	38	14
[3 0 2]	3	2.2	2.2	90	45	45	34	34	22	22
[3 0 1]	3	2.2	2.2	90	10	10	8	8	**5**	**5**
[4 1 2]	2	2.3	2.3	51	30	1	**20**	**21**	26	27
[4 1 Ī]	2	2.4	2.6	90	57	51	56	**20**	50	1
[3 0 Ī]	3	2.4	2.6	39	58	58	45	45	30	30
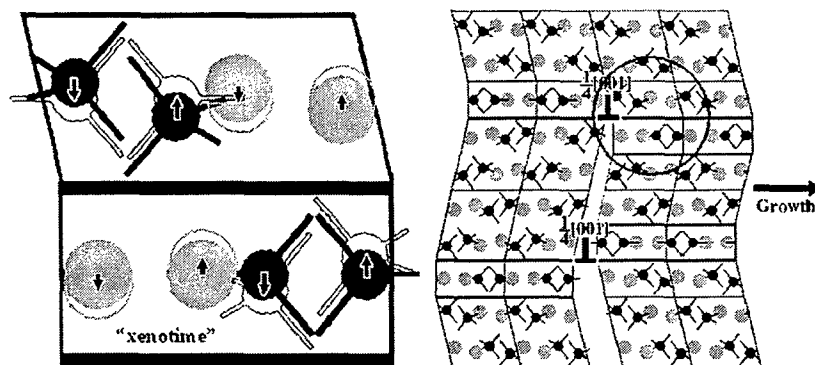
Fig. 8. Shuffles and growth mechanisms for $(1\ 0\ 0)[1\ 0\ 0]_C$ monazite deformation twin mode. The circled area is enlarged on the left-hand side of the diagram. Large gray circles are reflected La atom positions; black tetrahedra are reflected PO_4 group positions. Arrows show shuffle directions from sheared to reflected positions.

lowest shear, $(1\ 0\ 0)[4\ 0\ 1]_C$, is ruled out by the observed shear projections and by classical selection criteria is unlikely because it has $\lambda = 2$ and high δ_{mx}^{LaP}.

The shuffles for the $(1\ 0\ 0)[1\ 0\ 0]_C$ mode are shown schematically in Fig. 8. Adjacent PO_4 tetrahedra shuffle 0.068 nm in opposite directions parallel to $[1\ 0\ 0]$ (η_2), and rotate 39° in opposite directions around $[0\ 0\ 1]$. Adjacent La atoms shuffle 0.041 nm in opposite directions parallel to $[1\ 0\ 0]$ (Fig. 8). All shuffles are close to perpendicular to the twin shear direction (η_1), and lie in the plane of shear.

If during twinning, all of the atom shuffles and rotations within a $(1\ 0\ 0)$ layer of half-unit-cell thickness occur together, the structure of the layer halfway through the twinning transformation is that of xenotime, the tetragonal orthophosphate with higher molar volume formed by smaller rare-earth cations [33]. Although La-monazite resists transformation to the xenotime structure in bulk, this structure may act as an intermediate activated state, with a relatively low barrier to twinning. Moreover, if the xenotime structure within the half-unit-cell layer is stabilized at the twin boundary (the higher molar volume of xenotime being partially stabilized by the interface excess volume), the twin boundary energy may be reduced. The presence of such a layer would also produce mirror symmetry in the boundary structure (Fig. 8). Analogous boundary structures have been observed or

hypothesized for twins in other materials. The twin boundary for the common e-twin in calcite has been suggested to have similarities to the aragonite structure [34]. Extended twin boundaries consisting of unusual crystal structures have been observed in synthetic bicrystals of copper by Ernst et al. [35], who used high resolution TEM to identify thin slabs of rhombohedral (9R) and body-centered-cubic structures and used atomistic simulations to show that these structures lowered the boundary energies.

4.2. (0 0 1) Twins

Possible $(0\ 0\ 1)$ twin modes are listed in Table 2. There were no observations of the projected shear angle (θ_p) for this twin. However, the $(0\ 0\ 1)[0\ 0\ 1]_C$ mode, which is the reciprocal (or conjugate) of the $(1\ 0\ 0)[1\ 0\ 0]_C$ mode discussed in the previous section, has much smaller δ_{mx} for La atoms and PO_4 tetrahedra than other possible modes, and is therefore tentatively inferred to be the operating mode. This mode has $\lambda = 1$, the third smallest θ, and average ϕ_{mx}. The shuffles and the rotations of the tetrahedra are the same as those for the $(1\ 0\ 0)[1\ 0\ 0]_C$ mode, making the shuffles in this case parallel to η_1, rather than η_2 (Fig. 9). Like the $(1\ 0\ 0)[1\ 0\ 0]_C$ mode, a boundary structure consisting of a half-unit-cell of xenotime could form.

The $(0\ 0\ 1)[0\ 0\ 1]_C$ twin mode results in forma-

Table 2
Possible (0 0 1) twinning modes with $\theta < 65°$ and $q \leq 4$

Mode (η_2)	λ	$\delta_{mx}^{L.a}$ (Å)	δ_{mx}^{p} (Å)	ϕ_{mx} (°)	θ (°)
[0 0 1]	1	0.4	0.7	39	26
[0 1 2]	2	1.5	2.3	60	62
[1 2 4]	2	1.9	2.5	60	58
[1 1 2]	2	2.0	1.6	60	65
[0 1 3]	3	2.0	2.0	60	47
[2 1 3]	3	2.1	2.3	60	63
[1 1 3]	3	2.2	2.3	60	43
[3 1 4]	2	2.3	2.4	61	65
[1 0 4]	2	2.3	2.3	61	4
[1 0 2]	1	2.3	2.3	60	34
[2 0 3]	3	2.3	2.3	61	52
[1 0 3]	3	2.3	2.3	61	14
[0 1 4]	2	2.4	2.3	61	40
[1 1 4]	2	2.5	2.5	61	31
[$\bar{1}$ 0 3]	3	2.5	2.3	49	62
[$\bar{1}$ 1 4]	2	2.6	2.7	61	60
[3 0 4]	2	2.6	2.7	61	60
[2 1 4]	2	2.6	2.5	60	45
[$\bar{1}$ 0 4]	2	2.7	2.8	49	54
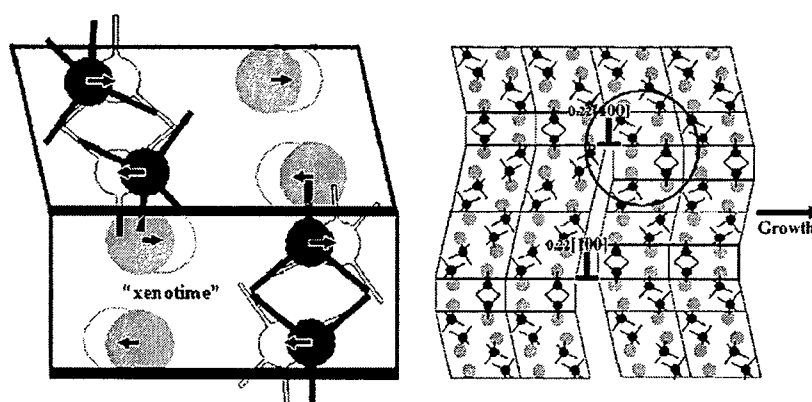
Fig. 9. Shuffles and growth mechanisms for (0 0 1)[0 0 1]$_c$ monazite deformation twin mode. The circled area is enlarged on the left-hand side of the diagram. This twin mode requires formation of a glide plane with displacement R of $\frac{1}{2}$[0 1 0].

tion of a glide plane with translation $\mathbf{R} = \frac{1}{2}$[010] at the twin boundary, rather than a mirror plane (see Appendix A). The glide plane could be distinguished from a mirror plane by imaging in dark-field TEM using reflections from planes common to both the twin and the parent that would be faulted by $\mathbf{R}$, i.e., with the beam along [1 0 0] using reflections of the type (0 k l) with k odd. Then the twins themselves should be out of con-

trast, but the twin boundaries would show up as antiphase boundaries if the displacement $\mathbf{R}$ was present. This test was not done in the present study. Nevertheless, twin planes with translation faults have been observed in other materials: {1 1 2} twins in b.c.c crystals [1,36] and pericline twins in feldspars [37–39]. The former requires physical translation of the twin relative to the parent by one-sixth of the interatomic distance, which results in

Table 3
Possible (1 2 0) twinning modes with $\theta < 65°$ and $q \leq 4$

Mode	η_1	λ	δ^{La}_{mx} (Å)	δ^{P}_{mx} (Å)	ϕ_{mx} (°)	θ (°)
(1 2 0)[0 1 0]$_I$	'[4 $\bar{2}$ 1]'	1	0.7	0.8	85	56
(0 1 2)[0 0 1]$_{II}$	[0 0 1]	1	0.9	0.8	90	54
(1 0 0)[4 $\bar{2}$ 1]$_{II}$	[4 $\bar{2}$ 1]	2	0.9	0.9	85	56
($\bar{1}$ $\bar{1}$ 2)[0 0 1]$_{II}$	[0 0 1]	1	1.6	1.6	90	55
(1 2 0)[1 1 0]$_I$	'[2 $\bar{1}$ $\bar{1}$]'	3	2.3	2.4	56	35
(1 2 0)[1 1 1]$_I$	'[2 $\bar{1}$ 5]'	3	2.5	2.6	56	62

a reduction in boundary energy, whereas the latter involves **R** of half the unit-cell length, without physical translation of the twin (i.e., intrinsic to the twin mode), as proposed here for the (0 0 1) monazite twin (an underlying assumption being that sheared atoms will shuffle by the smallest possible distances to create the twin structure, regardless of whether a glide plane or mirror plane forms). The effect of combined shear and lattice translation on twin interface structure is reviewed and discussed elsewhere [1,40]. A similar glide plane has been proposed for twin boundaries in aragonite [41].

4.3. (1 2 0) Twins and "Kinks"

Possible twin modes are listed in Table 3. There were no observations of θ_p for this twin. The mode with the smallest value of δ^{LaP}_{mx} is (1 2 0)[0 1 0]$_I$. This mode has $\lambda = 1$. However, it has significantly larger shear (θ) than the modes suggested for (1 0 0) and (0 0 1) twins. The shuffles are shown schematically in Fig. 10: all shuffles are normal to the **K**$_1$ plane, and rotations are around [0 0 1]. Two of the PO$_4$ tetrahedra require small shuffles (0.014 nm) with small rotations ($\phi \sim 12°$), while the other two require larger shuffles (0.085 nm) and rotations ($\phi \sim 85°$). Similarly, two of the La shuffles are small (0.028 nm) and two are larger (0.071 nm). The xenotime structure does not appear to be an intermediate step in these twin shears and shuffles.

Two of the other possible modes listed in Table 3 ((0 1 2)[0 0 1]$_{II}$, (1 0 0)[4 $\bar{2}$ 1]$_{II}$) have low values of δ^{LaP}_{mx}. Both are type II modes, with **K**$_1$ being irrational and misoriented by 0.90° and 0.87°,
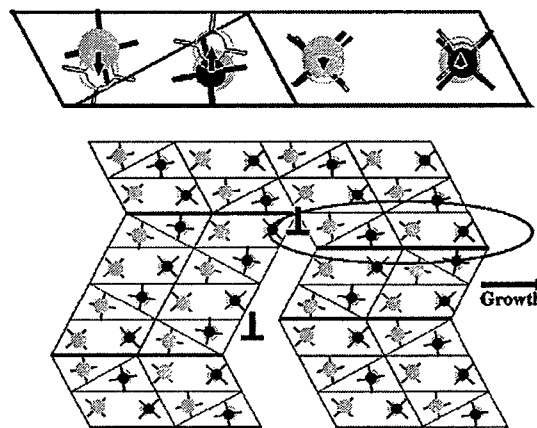
Fig. 10. Shuffles and growth mechanisms for the (1 2 0)[0 1 0]$_I$ monazite deformation twin mode.

respectively, from (1 2 0). TEM lattice images and diffraction patterns, which have alignment accuracy of about 1°, cannot distinguish these misorientations (Fig. 6). However, the (1 2 0) plane is a reflection plane rather than a 180° rotation in all (1 2 0) twin images, so the type II modes can be ruled out. The respective shear directions [4 $\bar{2}$ 1] and '[4 $\bar{2}$ 1]' are misoriented by 1.53° for the (1 0 0)[4 $\bar{2}$ 1]$_{II}$ and (1 2 0)[0 1 0]$_I$ modes, and **K**$_2$ is (1 0 0) for both; these modes are almost identical as far as shear directions and magnitudes are concerned, and could be considered to be a single compound mode, except that the symmetry across the (1 2 0) plane clearly distinguishes reflection from 180° rotation.

Two (1 2 0) twins were kinked on a plane near (1 2 1) (Fig. 6). Analysis presented in a companion paper [7] strongly suggests that these kinks are

(1 0 0)[2 1 0]$_{II}$ twins ($\mathbf{K}_1$ = ('4 8 3')), the reciprocal to a possible (1 0 0) twin mode (i.e. (1 0 0)[2 1 0]$_I$) discussed earlier. This kinking analysis is also consistent with the above identification of the (1 2 0) twin mode as (1 2 0)[0 1 0]$_I$. Shuffles and shear for (1 0 0)[2 1 0]$_{II}$ are the same as those the reciprocal mode (Fig. 11, Table 1). Shuffle directions are neither close to parallel to the shear direction (η_1) nor in the plane of shear. Like the (0 0 1) twin, the shuffles require formation of a glide plane at the twin interface.

Note that since [0 1 0] is a diad axis, the reciprocal mode to (1 2 0)[0 1 0]$_I$ is not a twin mode, but is indistinguishable from [0 1 0](0 0 1) slip. Similar relationships have been noted in intermetallic systems, where the reciprocal mode to a primary twining mode is a secondary slip system at low and intermediate temperatures, and a primary slip system at high temperatures. Since compatibility stresses caused by a particular deformation mode

Fig. 11. Shuffles for (1 0 0)[2 1 0]$_{I,II}$ twins. Shuffles do not lie in the plane of shear and require formation of a glide plane. Shuffle magnitudes are identical for both twin types, but PO$_4$ tetrahedra rotations differ.

can be relieved by the reciprocal mode, operation of both modes can help allow plastic deformation without cracking [42].

4.4. (1 2 $\bar{2}$) Twins

For the (1 2 $\bar{2}$) twin, there are few possible twin modes with indices≤4 and q≤4. The only mode consistent with the shear direction implied by the observation of θ_p~0 along [2 $\bar{1}$ 0] is (1 2 $\bar{2}$)[0 1 $\bar{1}$]$_I$, with an irrational shear direction η_1 of '[9 $\bar{4}$ 0]' that is 3.48° from [2 $\bar{1}$ 0] (Fig. 7). There are four different La shuffles of 0.11, 0.10, 0.10, and 0.05 nm and four different PO$_4$ shuffles of 0.12, 0.12, 0.11, and 0.05 nm, with PO$_4$ tetrahedra rotations of 53°, 40°, 39°, and 18°. The maximum shuffle is 0.12 nm, which is slightly larger than values inferred for the (1 0 0), (0 0 1), and (1 2 0) modes, and the shuffling periodicity λ is 2 instead of 1. Required shuffles are shown schematically in Fig. 12. None of the shuffles are parallel to η_1, and they do not lie in the plane of shear. Analysis of (1 2 $\bar{2}$) indentations in a companion paper [7] is consistent with the choice of (1 2 $\bar{2}$)[0 1 $\bar{1}$]$_I$ as the operating mode.

4.5. Twin mode prediction

In principle, the number of possible twin modes for a monoclinic crystal is very large. Even if we restrict the indices of the twin planes and shear directions to be ≤4 and the shear angles to less than 90°, and only consider those twin modes with q≤4, there are ~1100 possible modes with more than 150 rational twin planes (type I twins) and 150 rational shear directions (type II twins). In the
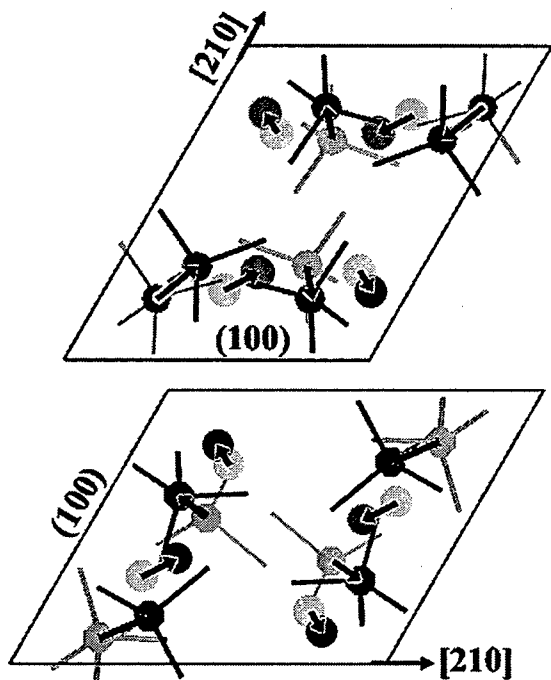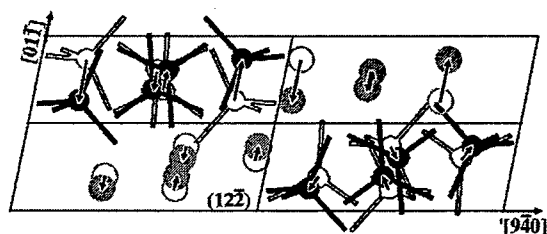

Fig. 12. Shuffles for the (1 2 $\bar{2}$)[0 1 $\bar{1}$]$_I$ twin. There are four distinct types of shuffles for both La atoms and PO$_4$ tetrahedra. Shuffles do not lie in the plane of shear.

previous sections, four primary twin modes and one secondary "kink" mode were inferred from observations of twin planes and shear-angle projections combined with considerations of the magnitudes of twinning shear and shuffle displacements. It is of interest to determine whether these observed twin planes and corresponding modes would be predicted *a priori* from ranking of any of the parameters used to characterize the shear and shuffle displacements.

The parameters θ, ϕ, and δ were calculated for all possible twin modes in monazite with indices≤4, q≤4, and $\theta < 65°$. Selected results are shown in Table 4 ranked to show the top 31 selec-

tions for the δ^{LaP}_{mx} parameter. The three most commonly observed twins have $\lambda = 1$ and fall at the top of the rankings, whereas the less common $(1\,2\,\bar{2})[0\,1\,\bar{1}]_I$ twin (two cases observed) has $\lambda = 2$ and falls slightly down the list, in 12th place. The uncommon $(1\,0\,0)[2\,1\,0]_{II}$ kinks in the $(1\,2\,0)$ twins (two cases observed), which are identified in the companion paper [3], and the reciprocal to this mode, $(1\,0\,0)[2\,1\,0]_I$, which was suggested as a possible additional twin mode on $(1\,0\,0)$ (Section 4.1), are ranked seventh and eighth.

Of the 11 modes with lower δ^{LaP}_{mx} than $(1\,2\,\bar{2})[0\,1\,\bar{1}]_I$, four are inferred to operate, another four are possible additional modes for $(1\,0\,0)$ and

Table 4

The twin modes in monazite with $\theta < 65°$, q≤4, indices≤4, and the 31 smallest shuffle magnitudes (δ^{LaP}_{mx}). Inferred modes are in bold. Other possible modes on observed twin planes are in bold italics. The column R shows whether a mirror plane (m) or glide plane (g) forms

#	Mode	K₁	η₁	λ	R	δ^{La}_{mx} (Å)	δ^{P}_{mx} (Å)	ϕ_{mx} (°)	θ (°)
1	**(1 0 0)[1 0 0]$_C$**	**(1 0 0)**	**[0 0 1]**	**1**	**m**	**0.4**	**0.7**	**39**	**26**
2	**(0 0 1)[0 0 1]$_C$**	**(0 0 1)**	**[1 0 0]**	**1**	**g**	**0.4**	**0.7**	**39**	**26**
3	**(1 2 0)[0 1 0]$_I$**	**(1 2 0)**	**[4 $\bar{2}$ 1]**	**1**	**m**	**0.7**	**0.8**	**85**	**56**
4	**(0 1 2)['0 0 1]$_I$**	**(0 1 2)**	**'[1 2 1]'**	**1**	**m**	**0.9**	**0.8**	**51**	**54**
5	**(0 1 2)[0 0 1]$_{II}$**	**'(1 2 0)'**	**[0 0 1]**	**1**	**g**	**0.9**	**0.8**	**90**	**54**
6	**(1 0 0)[4 $\bar{2}$ 1]$_{II}$**	**'(1 2 0)'**	**[4 $\bar{2}$ 1]**	**2**	**g**	**0.9**	**0.9**	**85**	**56**
7	*(1 0 0)[2 $\bar{1}$ 0]$_{II}$*	*(1 0 0)*	*[0 $\bar{2}$ 1]*	*1*	*g*	*0.8*	*1.1*	*7*	*60*
8	**(1 0 0)[2 $\bar{1}$ 0]$_{II}$**	**'(4 8 3)'**	**[2 $\bar{1}$ 0]**	**1**	**g**	**0.8**	**1.1**	**63**	**60**
9	(0 1 0)[0 2 1]$_{II}$	'(1 2 $\bar{4}$)'	[0 2 1]	1	g	1.1	1.1	71	49
10	*(1 0 0)[2 0 1]$_C$*	*(1 0 0)*	*[0 0 1]*	*1*	*g*	*1.1*	*1.1*	*51*	*29*
11	($\bar{1}$ 0 2)[0 0 1]$_C$	($\bar{1}$ 0 2)	[0 0 1]	1	g	1.1	1.1	55	29
12	**(1 2 $\bar{2}$)[0 1 $\bar{1}$]$_I$**	**(1 2 $\bar{2}$)**	**'[9 $\bar{4}$ 0]'**	**2**	**m**	**1.1**	**1.2**	**53**	**23**
13	($\bar{1}$ 2 2)[0 1 1]$_{II}$	(7 2 $\bar{2}$)	[0 1 1]	2	m	1.1	1.2	42	23
14	*(1 0 0)[2 1 1]$_I$*	*(1 0 0)*	*'[0 2 1]'*	*1*	*g*	*1.1*	*1.2*	*90*	*61*
15	(1 0 0)[2 1 1]$_{II}$	'($\bar{2}$ 3 1)'	[2 1 1]	1	g	1.1	1.2	40	61
16	(2 1 2)[1 0 1]$_I$	(2 1 2)	'[3 $\bar{7}$ 1]'	2	m	1.3	1.4	68	33
17	(2 1 2)[1 0 1]$_{II}$	'($\bar{1}$ 7 1)'	[1 0 1]	2	m	1.3	1.4	68	33
18	($\bar{1}$ 1 1)[0 1 1]$_I$	($\bar{1}$ 1 1)	'[2 1 1]'	1	g	1.4	1.4	38	58
19	($\bar{1}$ 1 1)[0 1 1]$_{II}$	'(9 1 $\bar{1}$)'	[0 1 1]	1	g	1.4	1.4	42	58
20	(2 1 0)[1 0 0]$_I$	(2 1 0)	'[$\bar{1}$ 2 1]'	1	g	1.4	1.4	79	57
21	(2 1 0)[1 0 0]$_{II}$	'(1 1 $\bar{1}$)'	[1 0 0]	1	g	1.4	1.4	60	57
22	($\bar{1}$ 0 1)[$\bar{1}$ 0 1]$_C$	($\bar{1}$ 0 1)	[1 0 1]	1	g	1.0	1.5	68	6
23	(1 0 1)[1 0 1]$_C$	(1 0 1)	[$\bar{1}$ 0 1]	1	m	1.0	1.5	73	6
24	(0 1 0)[1 2 1]$_{II}$	'(1 $\bar{1}$ 1)'	'[1 2 1]'	1	g	1.5	1.5	61	61
25	(1 0 $\bar{1}$)[2 0 $\bar{1}$]$_C$	($\bar{1}$ 0 1)	[1 0 1]	3	m	1.5	1.5	66	35
26	(1 0 1)[1 0 2]$_C$	(1 0 1)	[$\bar{1}$ 0 1]	3	m	1.5	1.5	66	35
27	(1 1 0)[1 1 0]$_I$	(1 1 0)	'[1 $\bar{1}$ 4]'	1	g	1.5	1.5	55	19
28	(1 1 0)[1 1 0]$_{II}$	'(1 $\bar{1}$ 6)'	[1 1 0]	1	g	1.5	1.5	53	19
29	(0 1 0)[1 4 1]$_{II}$	'(2 $\bar{1}$ 2)'	[1 4 1]	2	g	1.5	1.5	79	33
30	($\bar{1}$ 1 2)[0 0 $\bar{1}$]$_I$	($\bar{1}$ 1 2)	'[2 $\bar{4}$ 3]'	1	m	1.6	1.6	59	55
31	($\bar{1}$ 1 2)[0 0 $\bar{1}$]$_{II}$	'(1 2 0)'	[0 0 1]	1	m	1.6	1.6	90	55

(1 2 0) planes (Sections 4.1–4.3), and two have insignificantly smaller δ_{mx}^{LaP}. Differences in δ of ~0.01 nm have questionable significance in view of the evidence mentioned above for other factor(s) influencing twin selection. The only twin plane that was not observed, but has a mode with significantly smaller δ_{mx}^{LaP} than (1 2 $\bar{2}$)[0 1 $\bar{1}$]$_1$ or (1 0 0)[2 1 0]$_{II}$, is (0 1 2).

The twin shear (θ) and PO_4 tetrahedra rotation (ϕ) parameters and the presence of glide or mirror planes at the twin interface do not seem to correlate with the presence or absence of twin modes.

4.6. Twin mode abundance

The (1 0 0) twins were far more abundant (by a factor of 10) than any other twin. However, this relatively high abundance is not reflected in the relative values of any of the parameters λ, θ, ϕ, or δ; the less common (0 0 1) twins have identical values for all these parameters, while the (1 2 0) twins have slightly larger values of δ_{mx} and much larger values of θ and ϕ. Therefore, there must be other factors that affect twin abundance.

Other factors expected to affect both the selection and abundance of a twin mode would include the existence of low energy intermediate states, such as the xenotime structure discussed in Section 4.1, the elastic modulus for shear on K_1 in the direction of η_1, and the existence of low-energy twin boundary structures. Since the xenotime structure is possible for both the (1 0 0) and (0 0 1) twins, it does not account for their difference in abundance.

Significant differences exist in bond distributions across (1 0 0) and (0 0 1) planes of monazite. At the location marked in Fig. 13, the (1 0 0) planes are crossed only by relatively weak La–O bonds. Moreover, the projections of all these La–O bonds on (0 1 0), the plane of shear for the (1 0 0) twin, are close to perpendicular to the shear direction, $\eta_1 = $ [0 0 1]. This suggests that the elastic modulus for shear on (1 0 0) along [0 0 1] should be relatively low, favoring twinning and dislocation motion in this direction on this plane. In contrast, (0 0 1) planes at all locations are intersected at various angles by the stronger P–O bonds as well as La–O bonds, suggesting a higher elastic
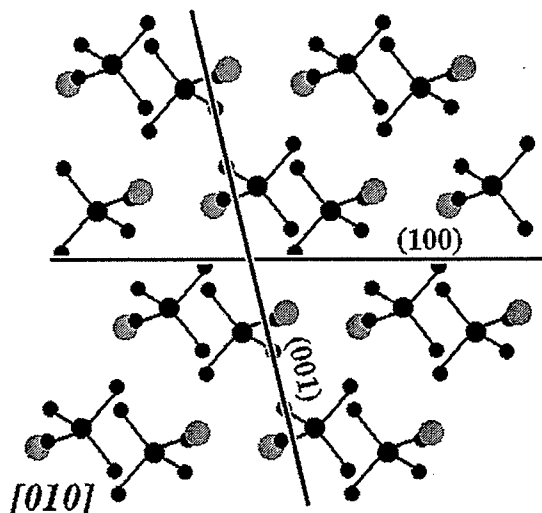

Fig. 13. P–O bond density projections across twin planes for the (1 0 0) and (0 0 1) twins. Projection zone is [0 1 0].

modulus for shear during (0 0 1) twinning. Anisotropy in shear modulus may be a determining factor for other twin modes as well, although this is difficult to assess quantitatively without single crystal elastic moduli for monazite, which to our knowledge have not been measured. Note that the other three inferred modes (1 2 0)[0 1 0]$_I$, (1 2 $\bar{2}$)[0 1 $\bar{1}$]$_I$, and (1 0 0)[2 $\bar{1}$ 0]$_{II}$ all have shear directions (η_1) on or very close to $\langle 210 \rangle$ ($'$[4 $\bar{2}$ 1]$'$, $'$[9 $\bar{4}$ 0]$'$, and [2 $\bar{1}$ 0], respectively). This suggests that shear in this direction is particularly easy, regardless of the shear plane.

Low-energy boundary structures might also be explained by geometric criteria, such as CSL theory. The near overlap of diffraction spots in electron diffraction patterns taken across twin boundaries was in some cases striking (Fig. 14). This suggests that CSLs might correlate with formation of certain twin planes. CSL theory has been used to describe twin modes and twin-plane defects, on the basis of the hypothesis that twin interfaces'"near" a low Σ CSL may have low interface energy, and may therefore nucleate more easily [4,43,44]. However, the CSLs are the same for all type I twin modes with the same K_1 and type II twins with the same η_1; they cannot distinguish which mode may operate on a particular plane or direction.
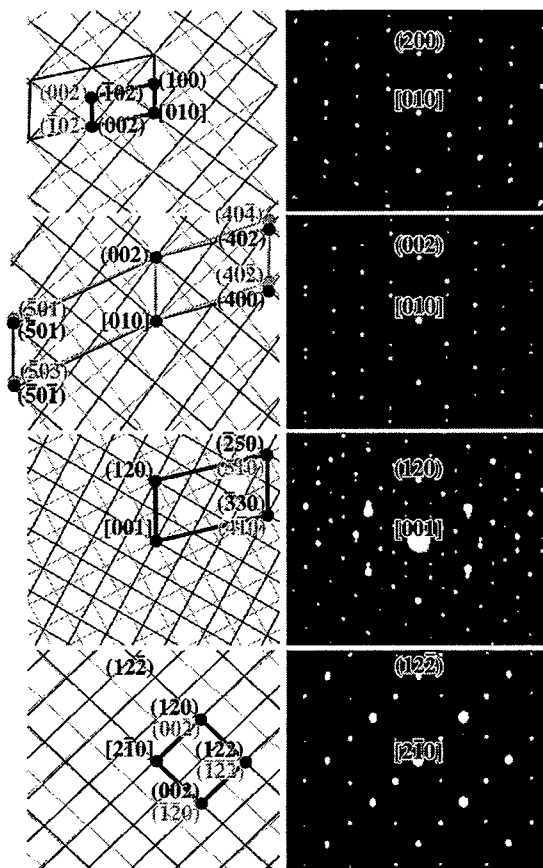
Fig. 14. Electron diffraction patterns for the four observed twin modes (1 0 0), (0 0 1), (1 2 0), and (1 1 $\bar{2}$). Near-coincidence site lattices for the twins are shown to the left of the twin interface.

The Σ value for CSLs is the ratio of the volume of the coincidence cell to a unit cell, or equivalently, the ratio of total lattice points to coincidence lattice points [45]. Interfaces with low energy often have low Σ CSLs [46], although not all low Σ CSLs have low energy [47,48]. For twinning, one coincidence site is always defined by $\mathbf{K}_1$ (Type I) or η_1 (Type II). For a monoclinic structure, the other lattice sites are usually not in exact coincidence, but "near" coincidence (NCSL) [5,6]. In this case, a shear strain, ε, characterizes the deviation from exact coincidence. Details of NCSL calculations are given in Appendix B. Results are listed

in Table 5 in order of increasing Σ for those with the smallest Σ and ε less than five.

The (1 0 0) twin has the lowest Σ NCSL (Σ = 2), and very low strain (ε = 1.8%). The two next most common twins, (0 0 1) and (1 2 0), also have reasonably low Σ and ε. The less common (12$\bar{2}$) twin has significantly higher Σ, as does the [2 1 0] "kink" twin. Twinning on (0 1 2) was not observed, but modes with small shuffles exist for this plane (Section 4.5), and this twin also has low strain to a low Σ CSL. This suggests that like the (0 0 1) plane, shear moduli on (0 1 2) may be relatively high and make twinning difficult.

The NCSL for the (1 0 0) twins is interesting (Figs. 8 and 14). The displacement shift complete (DSC) lattice that defines permissible interface dislocations has a $\frac{1}{2}$[0 0 1] component, which is twice the twinning dislocation for the (1 0 0)[1 0 0] mode (Fig. 8). Therefore, strain induced in the parent lattice by four twin boundary steps can be almost completely relieved by one $\mathbf{b}$ = [0 0 1] lattice dislocation.

5. Summary and conclusions

Five twin planes were observed, four of these being primary twins and one being found only as kinks in (1 2 0) twins. The observed/inferred twin modes for these planes are summarized in Table 6, and the twin planes and directions are rep-

Table 5
Σ and ε for monazite twin NCSLs. Listed by $\mathbf{K}_1$ or η_1 for increasing Σ. Observed twins are in bold

#	Σ	ε (%)	$\mathbf{K}_1/\eta_1$
1	**2**	**1.8**	**(1 0 0)**
2	**5**	**3.7**	**(0 0 1)**
3	6	3.4	(0 1 2)
4	7	3.4	(2 0 $\bar{1}$)
5	7	3.4	(1 0 3)
6	8	2.9	(0 1 $\bar{1}$)
7	8	3.9	(1 0 $\bar{2}$)
8	**9**	**1.4**	**(1 2 0)**
42	**16**	**2.5**	**(1 2 $\bar{2}$)**
58	**19**	**3.3**	**[2 1 0]**

Fig. 15. Stereonet showing the shear planes and principal directions for the five monazite deformation twin modes. Shear directions (η_1) are denoted by a hollow square. Arrows show the shear angle ($\frac{1}{2}\theta$) from η_2 to K_1.

resented on a stereonet in Fig. 15. The (0 0 1) twin plane and shear direction are unique. The (1 2 0), (1 2 $\bar{2}$), and [2 1 0] twins each have two equivalent twin planes. The most likely mode for the common (1 0 0) twins is a compound twin, (1 0 0)[1 0 0]$_C$, although the observations could not eliminate the possibility of several additional modes (shown in Table 6 but not in Fig. 15), each of which would have two equivalent shear directions in a given

monoclinic crystal. Therefore, a crystal of monazite may form deformation twins on a total of eight shear planes and directions, with additional shear directions possible for the (1 0 0) twin plane.

The twin modes are generally consistent with the selection rules of the classical theory of deformation twinning (small shear, shuffles, and shuffle periodicity). All except one have shuffle periodicity $\lambda = 1$. The three most common twins have modes with the lowest shuffle displacements of all the possible twin modes in a monazite crystal. The remaining two observed twins also have very small shuffle displacements; the only twin with significantly smaller shuffles that was not observed was (0 1 2), although there are additional modes on the (1 0 0) and (1 2 0) planes with smaller shuffles that may also be present. The (1 0 0), (0 0 1), and (1 2 $\bar{2}$) twins also have low shear angles. The shear angle, θ, and the shuffle rotations, ϕ, of the PO_4 tetrahedra appear to be less important indicators for twin selection than the shuffle displacement magnitude and periodicity. All of the inferred twin modes have $\theta < 65°$, shuffle displacements < 0.12 nm (approximately half of the La–O bond length), and shuffle periodicity≤2.

The abundance of the (1 0 0) twins is most likely a result of a relatively low shear modulus in the direction of twinning on the (1 0 0) plane, which is evident from simple inspection of the crystal structure. The difference in abundance between this and the other twins was not reflected in any of the shear or shuffle parameters.

Unusual boundary structures are proposed that

Table 6
Twin modes in monazite

{K_1, K_2, η_1, η_2, θ}	Abbreviation	Comments
(1 0 0), (0 0 1), [0 0 1], [1 0 0], 26.5°	(1 0 0)[1 0 0]$_C$	Observed in 58 grains
(0 0 1), (1 0 0), [1 0 0], [0 0 1], 26.5°	(0 0 1)[0 0 1]$_C$	Observed in five grains
(1 2 0), (1 0 0), '[4 $\bar{2}$ 1]', [0 1 0], 55.8°	(1 2 0)[0 1 0]$_1$	Observed in five grains
(1 2 $\bar{2}$), '(7 2 2)', '[9 $\bar{4}$ 0]', [0 1 $\bar{1}$], 23.2°	(1 2 2)(0 1 1)$_1$	Observed in two grains
'(4 $\bar{8}$ 3)', (1 0 0), [2 1 0], [0 $\bar{2}$ 1], 60.2°	(1 0 0)[2 1 0]$_{II}$	Kink in (1 2 0) twins: observed in two grains
(1 0 0), '(4 $\bar{8}$ 3)', '[0 $\bar{2}$ 1]', [2 1 0], 60.2°	(1 0 0)[2 1 0]$_1$	Possible if more than one mode operates on (1 0 0)
(1 0 0), '(5 $\bar{7}$ 3)', '[0 $\bar{2}$ 1]', [2 1 1], 60.9°	(1 0 0)[2 1 1]$_1$	
(1 0 0), ($\bar{1}$ 0 2), (0 0 1), [2 0 1], 28.4°	(1 0 0)[2 0 1]$_C$	

would influence the selection and abundance of twinning modes. However, direct experimental observations are required to confirm whether or not these structures exist. One such structure is a glide plane, rather than a mirror plane, at twin boundaries. The (0 0 1) twin was suggested to have this structure, with displacement vector $\mathbf{R} = \frac{1}{2}[0\ 1\ 0]$. Another is the formation of a slab of xenotime of half-unit-cell thickness at the interface of (1 0 0) and (0 0 1) twins, which may lower the twin interface energy and provide a low-energy intermediate structure, making twin growth facile. Low strain to a low Σ CSL may correlate with low energy for the twin plane ($\mathbf{K_1}$) and influence the abundance of such twins.

Acknowledgements

Appendix A. Calculation of twin shears and atomic shuffles

Two matrices, A and B, with rows containing vectors describing atomic coordinates from the center of a monazite unit cell are defined. A is a 3 × 192 matrix for a 2 × 2 × 2 monazite unit cell (192 atoms) that is reflected across $\mathbf{K_1}$ (type I) or rotated 180° around η_1 (type II), and B is a 3 × 5184 matrix for a 6 × 6 × 6 unit cell (5184 atoms) that is sheared. The number of different shuffles for a particular mode was found to be $\geq q$, and for modes with shuffles of small magnitude, the number of different shuffles always equaled q. With a 2 × 2 × 2 unit cell, all shuffles for modes with $q \leq 4$ can be found; for modes with larger q, only the four smallest shuffles out of a larger number of distinct shuffles can be found. Both A and B were transformed to Cartesian coordinates, with η_1 aligned with $[0\ 0\ 1]_{\text{Cartesian}}$ and $\mathbf{K_1}$ aligned with $[1\ 0\ 0]_{\text{Cartesian}}$, using standard procedures [49]. The

shear strain, s, is equal to $2\tan(\theta/2)$, and the twinning shear angle (θ) is:

$$\theta = 2\tan^{-1}([(\mathbf{m_1}\cdot\mathbf{I_2})^{-2}-1]^{1/2}) \qquad (A.1)$$
$$= 2\tan^{-1}(s/2)$$

where $\mathbf{m_1}$ is a Cartesian unit vector along $\mathbf{K_1}$ and $\mathbf{l_2}$ is a Cartesian unit vector along η_2 for type I twins [8]. A similar formula applies to type II twins, where $\mathbf{m_2}$ lies along $\mathbf{K_2}$ and $\mathbf{l_1}$ lies along η_1. A and B are rotated to a Cartesian reference frame using a rotation matrix with rows defined by $\mathbf{m_1}$, $\mathbf{m_1} \times \mathbf{l_1}$, and $\mathbf{l_1}$. In this frame of reference, the shear matrix H, reflection matrix F_I (type I twins), and rotation matrix F_{II} (type II twins) are:

$$H = \begin{bmatrix} 1 & 0 & 0 \\ 0 & 1 & 0 \\ s & 0 & 1 \end{bmatrix} \quad F_I = \begin{bmatrix} -1 & 0 & 0 \\ 0 & 1 & 0 \\ 0 & 0 & 1 \end{bmatrix} \quad F_{II} = \begin{bmatrix} -1 & 0 & 0 \\ 0 & -1 & 0 \\ 0 & 0 & 1 \end{bmatrix}$$
$$(A.2)$$

The coordinates in A were translated from $\mathbf{T}=[-1/2,-1/2,-1/2]_{\text{crystal}}$ to $[1/2,1/2,1/2]_{\text{crystal}}$ (after rotation and transformation of $\mathbf{T}$ to the Cartesian reference frame) in two successive iterations with increments in $\mathbf{T}$ of 1/6 and 1/24; this was checked for resolution of global minima from local minima by using one iteration of 1/12. A was then either reflected across $\mathbf{K_1}$ (type I twins) or rotated 180° around η_1 (type II twins) to find reflected or rotated atom coordinates A_r for a particular $\mathbf{T}$:

$$A_r = F_{I,II}\cdot(A-\mathbf{T}) \qquad (A.3)$$

The sheared coordinates B_s are:

$$B_s = H\cdot B \qquad (A.4)$$

A matrix with the coordinates of 32 La and 32 P atoms (B_{sm}) in B_s with the smallest maximum displacement (δ_{mx}) between A_s and B_s was found for each displacement vector $\mathbf{T}$. In some cases, a particular sheared La or P atom was the atom closest to more than one reflected La or P atom, respectively. When this occurred, the second smallest shuffles for each atom were compared and appropriate substitutions made. The δ_{mx} were compared for A_r with different $\mathbf{T}$ (Eq. (A.3)), and A_r with the smallest

δ_{mx} (A_{rm}) for all iterations of **T** was selected. The matrix S with shuffles for each atom can then be found from:

$$S = B_{sm} - A_{rm} \qquad (A.5)$$

The shuffle magnitude δ for a particular atom can be calculated from the magnitude of its respective row vector in S. The displacement vector **T** for A_{rm} (Eq. (A.3)) can be decomposed into vectors along η_2, η_1, and $\eta_2 \times \eta_1$. The component along η_2 defines the unit cell coordinates of K_1, and components along η_1 and $\eta_2 \times \eta_1$ define the displacement vector **R**. If **R** is non-zero, the twin plane is a glide plane rather than a mirror plane.

PO$_4$ tetrahedra rotations (ϕ) were calculated from lattices defined by three tetrahedra vectors from one oxygen atom. This was done for both the sheared (B_{sm}) tetrahedra and the reflected or rotated tetrahedra (A_{rm}), after correction for shuffles (Eq. (A.5)). The rotation of the sheared lattice with respect to rotated lattice was found using standard methods for decomposing a general lattice transformation into a symmetrical transformation and a rotation [49,50].

These calculations were incorporated into a *Mathematica*^{TM} program. La atom shuffles (δ^{La}), PO$_4$ tetrahedra shuffles (δ^P), PO$_4$ tetrahedra rotations (ϕ), shear angle (θ), and **R** vectors were calculated for all possible twin modes in monazite with indices$\leq$4, $q\leq$4, and shear strain (θ)$\leq$65°. Subsets of the results of these calculations are given in Tables 1–4.

Appendix B. Calculation of coincident site lattices

For type I twins, the lowest Σ reciprocal-space CSLs are assumed to contain K_1, and for type II twins, the lowest Σ real-space CSLs are assumed to contain η_1. Parent and twin crystal reciprocal-lattice vectors (type I) or real-space vectors (type II) are transformed to Cartesian coordinates and rotated to a Cartesian reference frame for a particular twin orientation relationship as described in Appendix A. Parent (V_P) and twin (V_T) real or reciprocal-space lattice vectors that are nearly coincident are found from:

$$2|V_P - V_T| / |V_P + V_T| < e \qquad (B.1)$$

where "nearness" is defined as $e = 0.05$. Lattice vectors from $[\bar{5}\,\bar{5}\,\bar{5}]$ to $[5\,5\,5]$ were searched. For type I twins, the parent structure matrix (S_P) for a tentative CSL is the 3×3 matrix formed from K_1 and two parent reciprocal-lattice vectors, V_{P1} and V_{P2}. S_P is compared to twin structure matrix (S_T) formed from K_1 and the twin reciprocal-lattice vectors V_{T1} and V_{T2} determined to be nearly coincident to V_{P1} and V_{P2} from Eq. (B.1). Σ is the determinant of S_P [49]. The strain tensor (E) defining how close a tentative CSL comes to exact coincidence for type I twins is [50]:

$$E = I - \begin{bmatrix} K_1 \\ V_{P1} \\ V_{P1} \end{bmatrix} \cdot \begin{bmatrix} K_1 \\ V_{T1} \\ V_{T1} \end{bmatrix}^{-1} \qquad (B.2)$$

where I is the identity matrix. A similar relationship substituting η_1 for K_1 and real-space for reciprocal-space lattice vectors holds for type II twins. Real-space and reciprocal-space CSLs have a reciprocity relationship through the displacement-shift-complete lattice (DSC) that is derived elsewhere [51]. The DSC lattice defines permissible line defects in the interface.

Since only off-diagonal elements are non-zero, the strain is a shear strain (ε) equal to the square root of the sum of the squared elements of E. The lowest Σ CSL with $\varepsilon < 5\%$ was found. A small subset of the results are listed in Table 5. Some calculations were checked using a modified method that did not assume coincidence for K_1 or η_1; in all cases, the calculated CSLs were the same. These calculations were incorporated into a *Mathematica*^{TM} program that looped through all possible twin planes and directions with indices$\leq$5. For a few twins a CSL with $\varepsilon < 5\%$ could not be found for indices$\leq$5, and it was necessary to do separate calculations for indices greater than 5.

The CSLs for the four observed twin planes and one twin direction are:

$(1\ 0\ 0)$: $\{(0\ 0\ 2), (0\ 1\ 0), (1\ 0\ 0)\}_P \approx \{(1\ 0\ 2), (0\ 1\ 0), (\bar{1}\ 0\ 0)\}_T$ $\Sigma = 2, \varepsilon = 1.8$

$(0\ 0\ 1)$: $\{(\bar{5}\ 0\ 0), (0\ 1\ 0), (0\ 0\ 1)\}_P \approx \{(\bar{5}\ 0\ 2), (0\ 1\ 0), (0\ 0\ \bar{1})\}_T$ $\Sigma = 5, \varepsilon = 3.7$

$(1\ 2\ 0)$: $\{(\bar{2}\ 1\ 1), (2\ 0\ 1), (1\ 2\ 0)\}_P \approx \{(\bar{2}\ 1\ 1), (1\ \bar{2}\ 1), (\bar{1}\ \bar{2}\ 0)\}_T$ $\Sigma = 9, \varepsilon = 1.4$

$(1\ 2\ \bar{2})$: $\{(\bar{3}\ 2\ 1), (1\ 2\ 0), (1\ 2\ \bar{2})\}_P \approx \{(\bar{3}\ 2\ 1), (0\ 0\ 2), (\bar{1}\ \bar{2}\ 2)\}_T$ $\Sigma = 16, \varepsilon = 2.5$

$[2\ 1\ 0]$: $\{[\bar{3}\ 2\ 3], [4\ 0\ 1], [2\ 1\ 0]\}_P \approx \{[\bar{1}\ \bar{4}\ 3], [2\ 3\ \bar{1}], [2\ 1\ 0]\}_T$ $\Sigma = 19, \varepsilon = 3.3$

References

[1] Christian JW, Mahajan S. Deformation twinning. Prog. Mat. Sci. 1995;39(1/2):1–157.

[2] Chu F, Pope DP. Deformation twinning in intermetallic compounds—the dilemma of shear vs. shuffles. Mater. Sci. Eng. 1993;A170:39–47.

[3] Bilby BA, Crocker AG. The theory of the crystallography of deformation twinning. Proc. Roy. Soc. 1965;A288:240.

[4] Baluffi RW, Brokman A, King AH. CSL/DSC lattice model for general crystal–crystal boundaries and their line defects. Acta Metall. 1982;30:1453–70.

[5] Bonnet R, Cousineau E. Computation of coincident and near-coincident cells for any two lattices–related DSC-1 and DSC-2 lattices. Acta Cryst. 1977;A33:850–6.

[6] King AH, Singh A. Generalizing the coincident site lattice model to non-cubic materials. J. Phys. Chem. Solids 1994;55(10):1023–33.

[7] Hay RS. (1 2 0) and (1 2 $\bar{2}$) monazite deformation twins. Acta Mater.

[8] Crocker AG. The crystallography of deformation twinning. In: Yoo MH, Wuttig M, editors. Twinning in advanced materials. Pittsburgh (PA): TMS; 1993. p. 3–17.

[9] Saxl I. Transformation of indices of planes and directions in twinned crystals. Czech. J. Phys. 1967;B17:586–94.

[10] Morgan PED, Marshall DB. Ceramic composites of monazite and alumina. J. Am. Ceram. Soc. 1995;78(6):1553–63.

[11] Marshall DB, Morgan PED, Housley RM, Cheung JT. High-temperature stability of the Al_2O_3-$LaPO_4$ system. J. Am. Ceram. Soc. 1998;81(4):951–6.

[12] Hikichi Y, Nomura T. Melting temperatures of monazite and xenotime. J. Am. Ceram. Soc. 1987;70(10):C252–C3.

[13] Hurlbut CS, Klein C. Manual of mineralogy (after James D. Dana), 19. New York: John Wiley & Sons, 1977 p. 532.

[14] Davis JB, Marshall DB, Housley RM, Morgan PED. Machinable ceramics containing rare-earth phosphates. J. Am. Ceram. Soc. 1998;81(8):2169–75.

[15] Kerans RJ. Viability of oxide fiber coatings in ceramic composites for accommodation of misfit stresses. J. Am. Ceram. Soc. 1996;79(6):1664–8.

[16] Curtin WA, Eldredge JI, Srinivasan GV. Push-out test on a new silicon carbide/reaction bonded silicon carbide ceramic matrix composite. J. Am. Ceram. Soc. 1993;76(9):2300–4.

[17] Cao HC, Bischoff E, Sbaizero D, Ruhle M, Evans AG, Marshall DB, Brennan JJ. Effect of interfaces on the properties of fiber-reinforced ceramics. J. Am. Ceram. Soc. 1990;73(6):1691–9.

[18] Davis JB, Marshall DB, Morgan PED. Monazite containing oxide–oxide composites. J. Eur. Ceram. Soc. 2000;20(5):583–7.

[19] Johnson SM, Blum Y, Kanazawa C, Wu H-J, Porter JR, Morgan PED et al. Processing and properties of an oxide/oxide composite. Key Eng. Mater. 1997;127-131:231–8.

[20] Johnson SM, Blum YD, Kanazawa CH. Development and properties of an oxide fiber–oxide matrix composite. Key Eng. Mat. 1999;164-165:85–90.

[21] Keller KA. Evaluation of all-oxide composites based on coated Nextel™ 610 and 650 fibers. Ceram. Eng. Sci. Proc. 2001;22(3):667–75.

[22] Keller KA et al. Effectiveness of monazite coatings in oxide/oxide composites after long term exposure at high temperature. J Am Ceram Soc 2003;86(2):325–32.

[23] Deer WA, Howie RA, Zussman J. Non-silicates. Rock forming minerals, 5. John Wiley and Sons: New York, 1963 pp. 339–46.

[24] Hay RS. Monazite and scheelite deformation mechanisms. Ceram. Eng. Sci. Proc. 2000;21(4):203–18.

[25] Davis JB et al. The influence of interfacial roughness on fiber sliding in oxide composites with La-monazite interphases. J Am Ceram Soc 2003;86(2):305–16.

[26] Mullica DF, Milligan WO, Grossie DA, Beall GW, Boatner LA. Ninefold coordination in $LaPO_4$: pentagonal interpenetrating tetrahedral polyhedron. Inorg. Chim. Acta 1984;95:231–6.

[27] Hahn T, editor. Space group symmetry. International tables for crytsallography, brief teaching edition, A. Dordrecht/Boston/Lancaster: D. Reidel Pub. Co.; 1985. p. 119.

[28] Hay RS, Welch JR, Cinibulk MK. TEM specimen preparation and characterization of ceramic coatings on fiber tows. Thin Solid Films 1997;308-309:389–92.

[29] Fischer-Cripps AC, Lawn BR. Indentation stress–strain curves for quasi-ductile ceramics. Acta Mater. 1996;44(2):519–27.

[30] Fischer-Cripps AC, Lawn BR. Stress analysis of contact deformation in quasi-plastic ceramics. J. Am. Ceram. Soc. 1996;79(10):2609–18.

[31] Park KT, Goo E. Deformation twinning in DO_3-ordered Fe_3Al alloys. Acta Metall. Mater. 1991;39(12):3027–35.

[32] Laves F. Uber den Einfluss von Ordnung un Unordnung auf Mechanische Zwillingsbildung. Naturwissenschaften 1952;39:546.

[33] Ni Y, Hughes JM, Mariano AM. Crystal chemistry of the monazite and xenotime structures. Am. Miner. 1995;80:21–6.

[34] Paterson MS. Dislocations and geological deformation. In: Dislocations and properties of real materials. The Institute of Metals, London; 1985. p. 359–377.

[35] Ernst F, Finnis MW, Kock A, Schmidt C, Straumal B, Gust W. Structure and energy of twin boundaries in copper. Z. Metallkd. 1996;87(11):911–22.

[36] Pond RC. Line defects in interfaces. In: Nabarro FRN, editor. Dislocations in solids. Oxford, UK: Elsevier Science Publishers; 1989. p. 1–66.

[37] Starkey J. Glide twinning in the plagioclase feldspars. In: Reed-Hill RE, Hirth JP, Rogers HC, editors. Deformation twinning. New York (NY): American Institute of Mining, Metallurgical, and Petroleum Engineers; 1964. p. 177–91.

[38] Marshall DB, McLaren AC. The structure of albite and pericline twin boundaries in anorthite. In: Eighth international congress on electron microscopy, 1. 1974. p. 490–1.

[39] Marshall DB, McLaren AC. Deformation mechanisms in experimentally deformed plagioclase feldspars. Phys. Chem. Miner. 1977;1:351–70.

[40] Dimitrakopulos GP, Karakostas T, Antonopoulos JG, Pond RC. Line defects separating distinct interfacial structures: topological character and diffusive flux considerations. Interface Sci. 1997;5:35–46.

[41] Wooster WA. Atomic arrangements on twin boundaries of crystals of calcite and aragonite. Mineral Mag. 1982;46:265–8.

[42] Yoo MH. Deformation twinning in superlattice structures. J. Mater. Res. 1989;4(1):50–4.

[43] Song SG, Gray GT. Structural interpretation of the nucleation and growth of deformation twins in Zr and Ti—I. Application of the coincidence site lattice (CSL) theory to twinning problems in H.C.P. structures. Acta Metall. Mater. 1995;43(6):2325–37.

[44] Lay S, Nouet G. On the possible multiplicity of nearly equivalent coincidence site lattices for (0 1 1 2) twin in hexagonal crystals. Acta Metall. Mater. 1993;41(5):1511–22.

[45] Sutton AP, Baluffi RW. Interfaces in crystalline materials. In: Monographs on the physics and chemistry of materials, 51. Oxford, UK: Oxford Science Publications; 1995. p. 819.

[46] Goodhew PJ. The relationship between grain boundary structure and energy. In: Baluffi RW, editor. Grain boundary structure and kinetics. Cleveland: ASM; 1980.

[47] Sutton AP, Balluffi RW. On geometric criteria for low interfacial energy. Acta Metall. 1987;35(9):2177–201.

[48] Dechamps M, Baribier F, Marrouche A. Grain-boundaries: criteria of specialness and deviation from CSL misorientation. Acta Metall. 1987;35(1):101–7.

[49] Bollmann W. Crystal lattices, interfaces, matrices. 1st ed. Published by the Author. 1982. p. 360.

[50] Hay RS. Coherency strain energy and thermal strain energy of thin films in any crystal system. Scripta Metall. 1992;26:535–40.

[51] Grimmer H. A reciprocity relation between the coincidence site lattice and the DSC lattice. Scripta Met. 1974;8:1221–4.

Section 8

Hardness, Toughness, and Sliding Properties of La-Monazite at High Temperatures

by J. B. Davis and D. B. Marshall

1. INTRODUCTION

La-monazite has a unique combination of properties that make it suitable for use as the basis of two-phase machinable ceramics,[1-3] as well as an interphase between fibers and matrix in oxide composites that enables interfacial debonding and damage tolerance.[4-14] It is a refractory material (melting point 2070°C),[15] compatible in high temperature oxidizing environments with many oxides that are either currently available as reinforcing fibers or of interest for future development as fibers and matrices. Most importantly, studies of various combinations of oxides and rare-earth phosphates (e.g., $LaPO_4$-Al_2O_3, $LaPO_4$-ZrO_2, $CePO_4$-ZrO_2, YPO_4-Al_2O_3 and $NdPO_4$-Al_2O_3) have shown that the oxide-phosphate interfacial bond is sufficiently weak that debonding occurs whenever a crack approaches an interface from within the phosphate.[1,16-19] The most detailed studies have involved the $LaPO_4$-Al_2O_3 system.

La-monazite has relatively low hardness (~5GPa)[1] at room temperature for such a refractory material, and has been shown to deform relatively easily at room temperature by dislocation slip and twinning. These properties clearly play a role in machinability. They may also be critical to the damage-tolerant behavior in ceramic composites, which requires sliding and pullout of fibers in addition to interfacial debonding. Calculations and experiments suggest that sliding of fibers in oxide systems with relatively dense matrices may require plastic deformation of the interphase material to avoid large misfit stresses due to sliding of fibers with rough interfaces or with minor fluctuations in

diameter.[17] Several studies have shown evidence for deformation associated with the sliding of monazite-coated fibers in composites. [16, 20]

Very little is known of the high temperature mechanical properties of La-monazite and the implications for the behavior of composites that depend upon it for their machinability or damage tolerance. In this study we investigate the variation of hardness, fracture toughness, and sliding response of single-phase La-monazite over the temperature range from room temperature to 1000 °C.

2. EXPERIMENTAL

2.1 Material processing

Monolithic $LaPO_4$ test samples of high purity and were fabricated by sintering powders formed by precipitation from aqueous solutions of $LaNO_3$ and phosphoric acid. The processing included procedures that allowed the La/P ratio to be controlled to be very close to the stoichiometric value of unity (within less that 500 ppm).[20] This control is important because powders prepared by normal precipitation methods invariably contain excess P, which is retained in amorphous grain boundary phases that can have a dominant effect on high temperature properties.

The sintered material was fully dense with microstructure consisting of uniform equiaxed grains ~ 0.5 to 1 mm in diameter (Fig. 1). The microstructure was stable for long periods at the sintering temperature (1200 °C). Even at higher temperatures, 1300 °C and 1400 °C, grain growth was slow and uniform.[21] Therefore, microstructural changes were not expected at the test temperatures of the present study.

2.2 Test procedures

Test specimens in the form of plates ~ 10 x 5 x 2 mm with polished surfaces were mounted in a commercial micro-indentation instrument that had been modified to allow testing at temperatures up to 1000 °C in an air environment. The surfaces were contacted under load control, with a Vickers pyramid that had been cut on the end of a long

sapphire rod. Both the specimen and the indenter were located within the hot zone of the furnace. The hardness and fracture toughness were calculated from measured dimensions of the contact area and radial cracks (Fig. 1), obtained after cooling the test specimen to room temperature.

High temperature sliding experiments were performed using the same equipment, using an x-y stage to translate the specimen while keeping the indenter stationary. The indenter in this case was an elongated triangular based pyramid with equivalent indentation volume for given contact area as the Vickers indenter (Fig. 2b)

3. RESULTS AND DISCUSSION

3.1 Hardness and toughness

Hardness and fracture toughness measurements are shown in Fig. 3. The hardness, H, was calculated from the indentation force, P, and projected contact area:

$$H = P/2a^2 \tag{1}$$

The fracture toughness, K_c, was calculated from the lengths, c, of the radial cracks:[22]

$$K_c = 0.016 \, (E/H)^{1/2}(P/c^{3/2}), \tag{2}$$

where E is the Young's modulus (133 GPa).[1] To test whether the hardness is affected by creep in this temperature range, measurements were obtained with the indenter load applied for two different times, 3 and 300 seconds.

The hardness decreased with increasing temperature by about 40% over the range tested, from 4.6 GPa at room temperature to 2.7 GPa at 1000 °C (3 sec. hold time). At the higher temperatures, the values were about 20% lower for the longer hold time, indicating that a small amount of creep occurred. However, given the relative values of the two hold times, these results suggest that the hardness at the shorter hold time should

not have been affected by creep. The fracture toughness decreased by a similar amount, from 1 to 0.4 MPa.m$^{1/2}$ over the temperature range, and showed no difference between the two hold times.

Also shown for comparison in Fig. 3a are literature values for the hardness of Y-doped zirconia, both single crystal and polycrystal, over the same temperature range.[23] The relative decrease in hardness of the La-monazite with temperature is considerably smaller than that of zirconia. A similar trend is seen in comparison with sapphire, where the hardness decreases from 28 to 12 GPa over the same temperature range.[24]

3.2 Sliding resistance

Measurements of sliding resistance, τ, (ratio of horizontal to vertical force) at fixed vertical load for various temperatures are summarized in Fig. 4. The sliding resistance is reasonably insensitive to the vertical load and shows a small decrease with increasing temperature. Representative sliding tracks are shown in Fig. 5.

The sliding deformation in these experiments is expected to be representative of processes occurring during the pullout of reinforcing fibers in tough composite containing monazite interphases. Observations in various systems have shown that initial debonding between the monazite and the oxide fibers follows the interface faithfully around asperities on the fiber surface, and that, as constrained sliding between the fiber and interphase occurs, the asperities (which have higher hardness than monazite) plow through the monazite interphase causing extensive local plastic deformation. However, the sliding in this case occurs at fixed asperity depth rather than fixed load as in the measurements in Fig. 4a. From the measurements in Fig.4a the dependence of the sliding resistance on temperature at fixed penetration depth can be calculated. The result, normalized by the sliding resistance at room temperature is shown in Fig. 4b. The sliding resistance decreases by a factor of about 2.5 over the temperature range studied.

The result in Fig. 4b can be used to estimate the effect of increasing temperature on the pullout of fibers in a composite, and hence the effect on toughness and damage tolerance. If we neglect effects of residual stresses due to expansion mismatch between fibers and matrix, the pullout length is given by:

$$\ell = \frac{R\sigma}{2\tau} \tag{3}$$

where R is the fiber radius, σ the fiber strength, and τ the interface sliding resistance. Thus, if the fiber strength is independent of temperature, a decrease in τ by a factor of 2.5 at 1000 °C, as observed in Fig. 4b, would cause an increase in pullout length by the same factor of 2.5. Changes of this magnitude are smaller than the typical variability measured from fiber to fiber in composites and are not expected to make a large difference to the composite properties.

ACKNOWLEDGEMENTS

REFERENCES

1. J. B. Davis, D. B. Marshall, P. E. D. Morgan and R. M. Housley, "Machinable Ceramics Containing Rare-Earth Phosphates," *J. Am. Ceram. Soc.,* **81**[8] 2169-75 (1998).

2. W. Min, K. Mityahara, K. Yoki, T. Yamaguchi, K. Daimon, Y. Hikichi, T. Matsubara and T. Ota, "Thermal and Mechanical Properties of Sintered $LaPO_4$-Al_2O_3 Composites," Mat. Res. Bull., **36** 939-45 (2001)

3. Zhou ZJ; Yang ZF; Yuan QM; Li XH , "Preparation of machinable Y-TZP/LaPO4 composite ceramics by liquid precursor infiltration," Journal of Rare Earths, 20[3] 197-203 (2002)

4. P. E. D. Morgan and D. B. Marshall, "Ceramic Composites of Monazite and Alumina," *J Am Ceram Soc,* **78** 1553-63 (1995).

5. P. E. D. Morgan, D. B. Marshall and R. M. Housley, "High Temperature Stability of Monazite-Alumina Composites," *J. Mat. Sci. Eng.,* **A195** 215 - 222 (1995).

6. D. B. Marshall, P. E. D. Morgan, R. M. Housley and J. T. Cheung, "High temperature Stability of the Al_2O_3-$LaPO_4$ System," *J. Am. Ceram. Soc.,* **81**[4] 951-56 (1998).

7. D. B. Marshall, J. B. Davis, P. E. D. Morgan and J. R. Porter, "Interface Materials for Damage-Tolerant Oxide Composites," *Key Engineering Materials,* **127-131** 27-36 (1997).

8. J. B. Davis, D. B. Marshall and P. E. D. Morgan, "Oxide Composites of Al_2O_3 and $LaPO_4$," *J. European Ceram. Soc.,* **19** 2421-2426 (1999).

9. J. B. Davis, D. B. Marshall and P. E. D. Morgan, "Monazite Containing Oxide-Oxide Composites," *J. Eur. Ceram. Soc.,* **20**[5] 583 - 587 (2000).

10. K. A. Keller, T.-I. Mah, E. E. Boakye and T. A. Parthasarathy, "Gel-Casting and Reaction Bonding of Oxide-Oxide Minicomposites with Monazite Interphase," *Ceramic Engineering and Science Proceedings,* **21**[4] 525-534 (2000).

11. T. A. Parthasarathy, E. Boakeye, M. K. Cinibulk and M. D. Perry, "Fabrication and Testing of Oxide/Oxide Microcomposites with Monazite and Hibonite as Interlayers," *J. Amer. Ceram. Soc.,* **82**[12] 3575-3583 (1999).

12. S. M. Johnson, Y. Blum, C. Kanazawa, H.-J. Wu, J. R. Porter, P. E. D. Morgan, D. B. Marshall and D. Wilson, "Processing and Properties of an Oxide/Oxide Composite," *Key Engineering Materials,* **127-131** 231-38 (1997).

13. S. M. Johnson, Y. Blum and C. H. Kanazawa, "Development and Properties of an Oxide Fiber-Oxide Matrix Composite," *Key. Eng. Mat.,* **164-165** 85-90 (1999).

14. K. A. Keller, T. Mah, T. A. Parthasarathy, E. E. Boakye and M. Cinibulk, "Evaluation of all-oxide composites based on coated Nextel 610 and 650 fibers," *Ceramic Engineering and Science Proceedings,* **22**[3] 667-75 (2001).

15. Y. Hikichi and T. Nomura, "Melting Temperatures of Monazite and Xenotime," *J. Am. Cer. Soc.,* **70**[10] C252-C253 (1987).

16. Davis, J. B., Hay, R. S., Marshall, D. B., Morgan, P.E.D., and Sayir, A., "The Influence of Interfacial Roughness on Fiber Sliding in Oxide Composites with La-Monazite Interphases," J. Am. Ceram. Soc., 86[2] 305-316 (2003)

17. D. B. Marshall, P. E. D. Morgan and R. M. Housley, "Debonding in Multilayered Composites of Zirconia and $LaPO_4$," *J. Am. Ceram. Soc.,* **80**[7] 1677-83 (1997).

18. D.-H. Kuo and W. M. Kriven, "Characterization of Yttrium Phosphate and a Yttrium Phosphate/Yttrium Aluminate Laminate," *J. Am. Ceram. Soc.,* **78**[11] 3121-3124 (1995).

19. M. G. Cain, R. L. Cain, A. Tye, P. Rian, M. H. Lewis and J. Gent, "Structure and Stability of Synthetic Interphases in CMCs," *Key Engineering Materials,* **127-131** 37-49 (1997).

20. Keller, K.A., et al., "Effectiveness of Monazite Coatings in Oxide/Oxide Composites After Long Term Exposure at High Temperature," J. Am. Ceram. Soc., 2002. **86**[2] 325-32 (2003)

21. Davis, J. B., Sudre, O., Marshall, D. B., Morgan, P.E.D., and Housley, R, "The Synthesis and Processing of La-monazite," in preparation for J. Am. Ceram. Soc

22. Anstis, G.R., Chantikul, P., Lawn, B.R., and Marshall, D.B., "A Critical Evaluation of Indentation Techniques for Measuring Fracture Toughness: I. Direct Crack Measurements," J. Amer. Ceram. Soc. <u>64</u> [9], 533-538 (1981).

23. V. Tikare and A. H. Heuer, "Temperature-Dependent Behavior of Transformation-Toughened Zirconia-Based Ceramics," J. Am. Ceram. Soc., 74[3] 593-97 (1991)

24. Farber, B.Y.; Yoon, S.Y.; Lagerlof, K.P.D.; Heuer, A.H. "Microplasticity During High Temperature Indentation and the Peierls Potential in Sapphire (α-Al_2O_3) Single Crystals," Physica Status Solidi A , 137[2] 485-98 (1993).
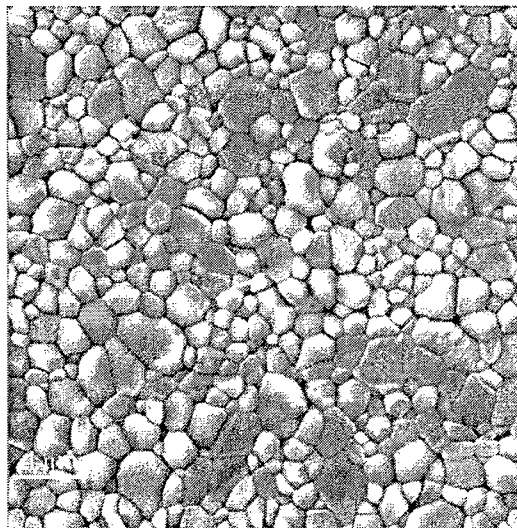
Fig. 1. Microstructure of sintered LaPO$_4$ (thermally etched cross section after sintering at 1200 °C)

Direction of sliding
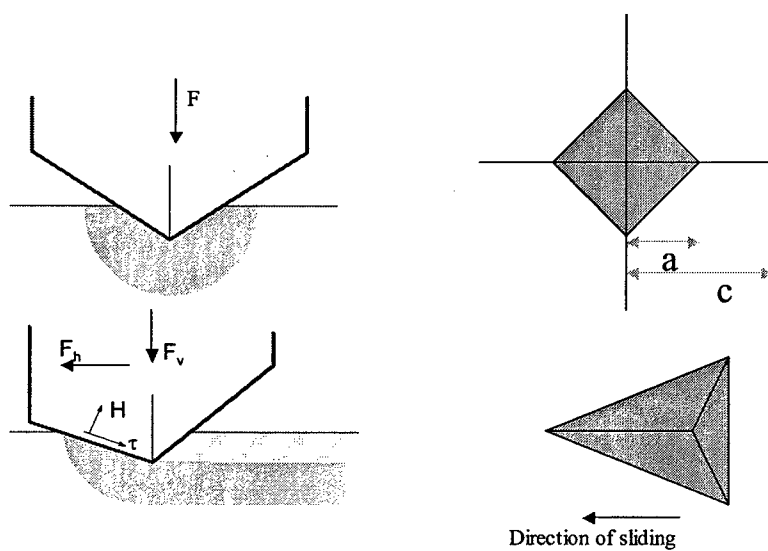
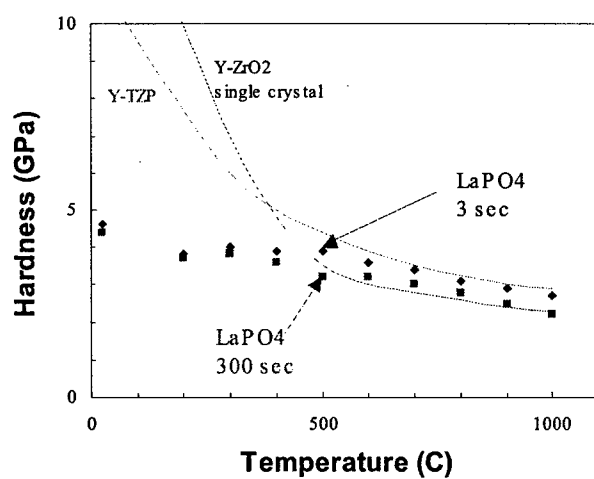Fig. 2. Schematic showing indentation and sliding contact dimensions
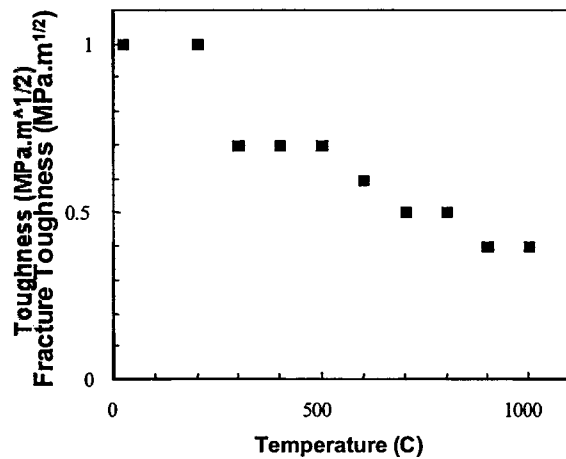
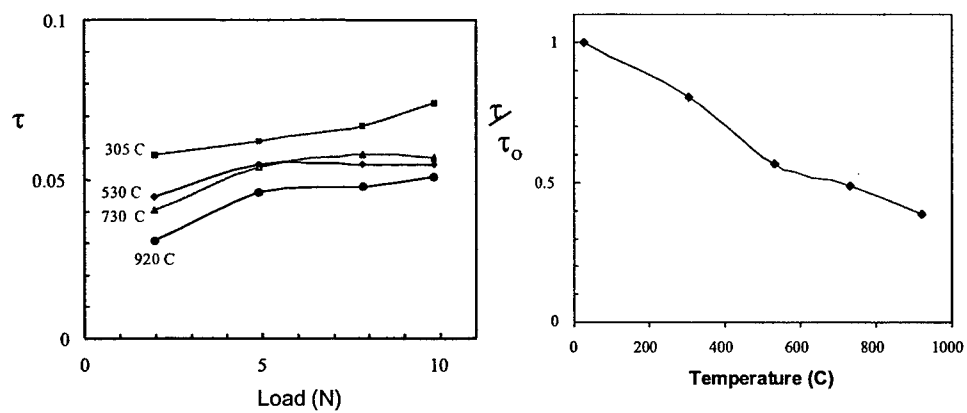Fig. 3. Indentation hardness and fracture toughness of LaPO₄.

Fig.4. Sliding resistance for sharp pyramidal sapphire indenter on La-monazite: (a) ratio of horizontal and vertical forces for range of loads (vertical force) and temperatures; (b) relative decrease with temperature for fixed penetration depth.
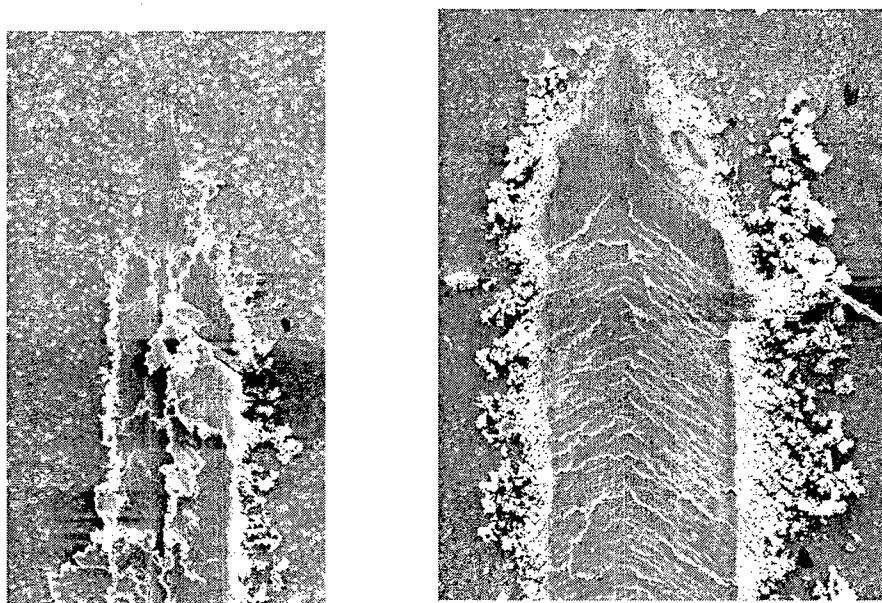
Fig. 5. Damage in La-monazite due to sliding of pyramidal indenter as in Fig. 2 at (a) room temperature and (b) 750 °C.

High Temperature Creep of La-Monazite

by M. Berbon, J. B. Davis and D. B. Marshall

ABSTRACT

Compressive creep of La-monazite is investigated in the temperature range 1100 °C to 1500 °C. The study includes both high-purity single-phase material and material with excess phosphorus located in amorphous grain boundary phases. The results indicate that the presence of small amounts of excess P in polycrystalline $LaPO_4$ has a large effect on microstructural stability and creep at high temperature. Materials with La/P ratio close to unity (within ~ 500 ppm) show little grain growth at temperatures up to 1400 °C and deform by creep at rates similar to those of alumina and zirconia, with stress exponent ~ 1. Materials containing excess P (as little as ~1%) show more rapid grain growth, higher creep rates, and cavitation during creep. The results are compared with creep rates of other refractory oxides and oxide fibers. Implications for the behavior of composites containing La-monazite are considered.

1. INTRODUCTION

La-monazite has a unique combination of properties that make it suitable for use as the basis of two-phase machinable ceramics,[1-3] as well as an interphase between fibers and matrix in oxide composites that enables interfacial debonding and damage tolerance.[4-14] These include: high melting point (2070°C);[15] compatibity in high temperature oxidizing environments with other oxides that are either currently available as reinforcing fibers or of interest for future development as fibers and matrices; and interfacial bonding with other oxides that is sufficiently weak to allow debonding whenever a crack approaches an interface from within the monazite.[1,16-19]

La-monazite also has unusual deformation properties at room temperature for such a refractory material. It has relatively low hardness (~5GPa)[1] and has been shown to deform relatively easily at room temperature by dislocation slip and twinning.[20-24] This ease of deformation clearly plays a role in machinability. It may also be critical to the damage-tolerant behavior in ceramic composites, which requires sliding and pullout of fibers in addition to interfacial debonding. La-monazite is also known to recover readily from radiation-induced displacive damage events at near-ambient temperatures,[25-27] making it extremely resistant to amorphization by radiation damage, and thus an ideal host for containment of actinide or transuranic elements.[28,29] The question therefore arises as to whether high temperature deformation and creep might similarly be enhanced and thereby impair the usefulness of La-monazite in the above applications.

In this study we investigate the compressive creep of La-monazite in the temperature range 1100 °C to 1500 °C. The study includes both high purity single-phase material and material with excess phosphorous located in amorphous grain boundary phases.

2. EXPERIMENTAL

2.1 Material preparation

La-monazite test samples were prepared by sintering powders prepared by precipitation from aqueous solutions of $LaNO_3$ and phosphoric acid. Two preparation methods were used. In one, the precipitate was washed with water, dried and calcined, and hot-pressed at 1400 °C for 1 h. This produced a material with a small excess of phosphorus (<1%), a result of the fact that precipitated rhabdophane ($LaPO_4.1/2H_2O$) invariably contains strongly bound excess phosphorus (thought to be associated with the channels in the rhabdophane structure), which is not removed by aqueous washing and remains as a second phase after final processing.[30] The other method involved washing the precipitated rhabdophane with a strong base to remove the excess phosphorus, and testing for the correct stoichiometry using a sensitive technique described elsewhere.[30] After adjusting the La/P ratio to unity (within ~ 500 ppm), the precipitates were dried and heated to form the monazite structure. The calcined powder was then attrition milled to form a uniform distribution of equiaxed particles with diameter less than ~ 100 nm. The particles were then dispersed, consolidated by filter pressing, and sintered at 1400 °C for 2h.

2.2 Creep testing

La-monazite test samples were cut into rectangular blocks ~ 2.7 x 2.7 x 7 mm with polished faces and loaded in compression in a furnace at temperatures in the range 1100 °C to 1500 °C in air. The load was applied via self-aligning plattens using dead weights. Temperatures were monitored by a thermocouple located adjacent to the test specimens. Creep strains were measured with a self-compensating LVDT system. After testing, both the original polished surfaces of the test specimens and new cross-sections were examined by SEM.

3. RESULTS

Typical creep curves for stoichiometric and P-rich monazite, at 1400 °C and at various stress levels, are compared in Fig. 1. All of the curves show initially high strain rates, which decrease continuously to quasi-steady-state. However, the magnitudes of the strains and strain rates at any given stresses and times are much lower in the stoichiometric material than in the P-rich material. Moreover, the difference between the initial strain rate and the quasi-steady-state value is larger in the P-rich material, with a more distinct change being evident between the two regimes.

Detailed interpretation of creep mechanisms from measured creep rates is complicated by the presence of grain growth during testing. In the stoichiometric material the microstructure was relatively stable, with grain sizes increasing by a negligible amount at 1200 °C and a factor of about 1.5 to 2 at 1300 °C and 1400 °C. A small amount of cavitation at some 3-grain junctions was evident at the highest stress levels and temperature. The quasi-steady-state creep rates (strain rates at end of test) appear to follow a stress exponent of 1 (Fig. 3).

In the P-rich material, microstructural changes during testing, both grain growth and cavitation, were more rapid (Fig. 4). This is most likely due to the presence of liquid phase at grain boundaries and 3-grain junctions, although this has not been observed directly. (Whereas the amount of excess P is sufficiently small in this material that a uniformly distributed amorphous grain boundary phase is not expected to be detectable by SEM observation, such phases have been observed in similar materials with higher amounts of excess P.) The presence of a liquid phase would be expected to give very high initial creep rates and rapid transition to relatively lower creep rates (albeit still higher than in the absence of the liquid) as grain growth occurs, as observed in Fig. 1b. In view of the rapid microstructural evolution during creep tests, stress-jump tests were used in this case to determine the stress exponent at constant microstructure. The value thus obtained was 1.6. This stress exponent is consistent with various creep models, including grain boundary sliding in specimens with grain boundary liquid phase. However, creep

mechanisms in these P-rich monazite specimens are complicated by the extensive cavitation that develops during testing.

4. DISCUSSION

The quasi-steady-state creep rates for both materials are summarized and compared with creep data from the literature for several other oxides (Al_2O_3, Y-ZrO_2, and Al_2O_3/YAG)[31-33] in Fig. 5. To facilitate the comparison, All creep rates are adjusted to correspond to a common grain size, assuming a quadratic grain size dependence:

$$d\varepsilon/dt = A \, D^2 \qquad (1)$$

It is apparent from Fig. 5 that the creep rates under given conditions (temperature, stress, and grain size) for the stoichiometric monazite are similar to those of Y-stabilized zirconia and pure alumina. Therefore, the relativley low resistance of monazite to deformation at room temperature relative to these other oxides does not appear to extend to high temperatures. We note that the creep rates of monazite, pure alumina and Y-ZrO2 are all several orders of magnitude higher than in La-doped alumina, one of the most creep resistant polycrystalline oxides, and that creep rates for the Al_2O_3/YAG eutectic structures are lower considerably lower than any of the polycrystalline materials.

Further insight into the likely influence of creep in oxide composites at high temperature can be gained from Fig, 6, where creep rates at 2.5 μm grain size for monazite and bulk alumina are compared with creep rates for various Nextel oxide fibers (not corrected for grain size). These fibers all have fine grain sizes and correspondingly higher creep rates than comparable, larger grained bulk materials. This is evident in the data in Fig. 6, which shows higher creep rates for Nextel 610 fibers (polycrystalline alumina with grain size ~100 nm) at 1200 °C than for bulk Al_2O_3 with grain size 2.5 μm. The creep rate for $LaPO_4$ is smaller than that of the alumina fibers at given stress, indicating that the presence of $LaPO_4$ in the composite leads to increase of creep resistance rather than a decrease (even more so in the initial stages, where an iso-elastic strain condition would lead to lower stresses in the monazite (Young's modulus 133 GPa) than in the fibers (400 GPa), as indicated by the shaded bands in Fig.6). As creep progresses towards and iso-

strain rate condition, load transfer would occur from the fibers to the matrix. With the more creep-resistant Nextel 720 mullite-based fibers, the opposite conclusions would hold.

Comparisons of the temperature dependence of quasi-steady-state creep rates at fixed stress levels for $LaPO_4$ and Nextel fibers (610 and 720) are given in Fig. 7. The $LaPO_4$ data appears to be less sensitive to temperature, although there is not sufficient overlap in temperature ranges for proper comparison.

5. CONCLUSIONS

The results of this study indicate that the presence of small amounts of excess P in polycrystalline $LaPO_4$ has a large effect on microstructural stability and creep at high temperature. Materials with La/P ratio close to unity (within ~ 500 ppm) show little grain growth at temperatures up to 1400 °C and deform by creep at rates similar to those of alumina and zirconia, with stress exponent ~ 1. Materials containing excess P (as little as ~1%) show more rapid grain growth, higher creep rates, and cavitation during creep.

ACKNOWLEDGEMENTS

REFERENCES

1. J. B. Davis, D. B. Marshall, P. E. D. Morgan and R. M. Housley, "Machinable Ceramics Containing Rare-Earth Phosphates," *J. Am. Ceram. Soc.,* **81**[8] 2169-75 (1998).

2. W. Min, K. Mityahara, K. Yoki, T. Yamaguchi, K. Daimon, Y. Hikichi, T. Matsubara and T. Ota, "Thermal and Mechanical Properties of Sintered $LaPO_4$-Al_2O_3 Composites," Mat. Res. Bull., **36** 939-45 (2001)

3. Zhou ZJ; Yang ZF; Yuan QM; Li XH , "Preparation of machinable Y-TZP/LaPO4 composite ceramics by liquid precursor infiltration," Journal of Rare Earths, 20[3] 197-203 (2002)

4. P. E. D. Morgan and D. B. Marshall, "Ceramic Composites of Monazite and Alumina," *J Am Ceram Soc,* **78** 1553-63 (1995).

5. P. E. D. Morgan, D. B. Marshall and R. M. Housley, "High Temperature Stability of Monazite-Alumina Composites," *J. Mat. Sci. Eng.,* **A195** 215 - 222 (1995).

6. D. B. Marshall, P. E. D. Morgan, R. M. Housley and J. T. Cheung, "High temperature Stability of the Al_2O_3-$LaPO_4$ System," *J. Am. Ceram. Soc.,* **81**[4] 951-56 (1998).

7. D. B. Marshall, J. B. Davis, P. E. D. Morgan and J. R. Porter, "Interface Materials for Damage-Tolerant Oxide Composites," *Key Engineering Materials,* **127-131** 27-36 (1997).

8. J. B. Davis, D. B. Marshall and P. E. D. Morgan, "Oxide Composites of Al_2O_3 and $LaPO_4$," *J. European Ceram. Soc.,* **19** 2421-2426 (1999).

9. J. B. Davis, D. B. Marshall and P. E. D. Morgan, "Monazite Containing Oxide-Oxide Composites," *J. Eur. Ceram. Soc.,* **20**[5] 583 - 587 (2000).

10. K. A. Keller, T.-I. Mah, E. E. Boakye and T. A. Parthasarathy, "Gel-Casting and Reaction Bonding of Oxide-Oxide Minicomposites with Monazite Interphase," *Ceramic Engineering and Science Proceedings,* **21**[4] 525-534 (2000).

11. T. A. Parthasarathy, E. Boakeye, M. K. Cinibulk and M. D. Perry, "Fabrication and Testing of Oxide/Oxide Microcomposites with Monazite and Hibonite as Interlayers," *J. Amer. Ceram. Soc.,* **82**[12] 3575-3583 (1999).

12. S. M. Johnson, Y. Blum, C. Kanazawa, H.-J. Wu, J. R. Porter, P. E. D. Morgan, D. B. Marshall and D. Wilson, "Processing and Properties of an Oxide/Oxide Composite," *Key Engineering Materials,* **127-131** 231-38 (1997).

13. S. M. Johnson, Y. Blum and C. H. Kanazawa, "Development and Properties of an Oxide Fiber-Oxide Matrix Composite," *Key. Eng. Mat.,* **164-165** 85-90 (1999).

14. K. A. Keller, T. Mah, T. A. Parthasarathy, E. E. Boakye and M. Cinibulk, "Evaluation of all-oxide composites based on coated Nextel 610 and 650 fibers," *Ceramic Engineering and Science Proceedings,* **22**[3] 667-75 (2001).

15. Y. Hikichi and T. Nomura, "Melting Temperatures of Monazite and Xenotime," *J. Am. Cer. Soc.,* **70**[10] C252-C253 (1987).

16. Davis, J. B., Hay, R. S., Marshall, D. B., Morgan, P.E.D., and Sayir, A., "The Influence of Interfacial Roughness on Fiber Sliding in Oxide Composites with La-Monazite Interphases," J. Am. Ceram. Soc., 86[2] 305-316 (2003)

17. D. B. Marshall, P. E. D. Morgan and R. M. Housley, "Debonding in Multilayered Composites of Zirconia and $LaPO_4$," *J. Am. Ceram. Soc.,* **80**[7] 1677-83 (1997).

18. D.-H. Kuo and W. M. Kriven, "Characterization of Yttrium Phosphate and a Yttrium Phosphate/Yttrium Aluminate Laminate," *J. Am. Ceram. Soc.,* **78**[11] 3121-3124 (1995).

19. M. G. Cain, R. L. Cain, A. Tye, P. Rian, M. H. Lewis and J. Gent, "Structure and Stability of Synthetic Interphases in CMCs," *Key Engineering Materials,* **127-131** 37-49 (1997).

20. Keller, K.A., et al., "Effectiveness of Monazite Coatings in Oxide/Oxide Composites After Long Term Exposure at High Temperature," J. Am. Ceram. Soc., 2002. **86**[2] 325-32 (2003)

21. Hay, R. S. and Marshall, D. B., "Deformation Twinning in Monazite," Acta Mat. **51**[18] 5235-5254 (2003)

22. R. S. Hay, "Monazite and Scheelite Deformation Mechanisms," *Ceram. Eng. Sci. Proc.* **21**, 203–18 (2000).

23. R. S. Hay, "(120) and (12*2*) Monazite Deformation Twins," *Acta Mater.* **51**, 5255–62 (2003).

24. R. S. Hay, "Climb-Dissociated Dislocations in Monazite at Low Temperature," *J. Am. Ceram. Soc.,* **87** [6] 1149–1152 (2004)

25. F. G. Karioris, K. A. Gowda and L. Cartz, "Heavy Ion Bombardment of Monoclinic ThSiO4, ThO2 and Monazite," *Radiation Effects Letters,* **58** 1-3 (1981).

26. T. C. Ehlert, K.A. Gowda, F. G. Karioris and L. Cartz, "Differential Scanning Calorimetry of Heavy Ion Bombarded Synthetic Monazite," *Radiation Effects,* **70** 173-181 (1983).

27. A. Meldrum, L. A. Boatner and R. C. Ewing, "A Comparison of Radiation Effects in Crystalline ABO4-type Phosphates and Silicates," *Mineralogical Magazine,* **64**[2] 185-194 (2000).

28. L. A. Boatner and B. C. Sales, "Monazite"; in Radioactive Waste Forms for the Future. Eds W. Lutze and R. C. Ewing. New York, North-Holland. **Chapter 8,** 1988.

29. A. Meldrum, L. A. Boatner and R. C. Ewing, "Electron-Irradiation-Induced Nucleation and Growth in Amorphous LaPO$_4$, ScPO$_4$, and Zircon," *J. mater. Res.,* **12**[7] 1816-1827 (1997).

30. Davis, J. B., Sudre, O., Marshall, D. B., Morgan, P.E.D., and Housley, R., "The Synthesis and Processing of La-monazite" in preparation for J. Am. Ceram. Soc.

31. Al2O3 data:Cho et al J. Mat. Res. 16[2]425-429 (2001)

32. T. A. Parthasarathy, T. Mah and L. E. Matson, Deformation Behavior of an Al_2O_3-$Y_3Al_5O_{12}$ Eutectic Composite in Comparison wih Sapphire and YAG," J. Am. Ceram. Soc., **76**[1] 29-32 (1993)

33. M. Jimenez-Melendo, A. Dominguez-Rodriguez and A. Bravo-Leon, "Superplastic Flow of Fine-Grained Yttria-Stabilized Zirconia Polycrystals: Constitive Equation and Deformation Mechanisms," J. Amer. Ceram. Soc., 81[11] 2761-76 (1998)

34. Wilson & Viser, Nextel 650 Ceramic Oxide Fiber: New Alumina-Based Fiber for High Temperature Composite Reinforcement," Ceram. Eng. Sci. Proc. 21[4] 363-373 (2000)

35. D. M. Wilson, S. L. Lieder and D. C. Lueneburg, "Microstructure and High Temperature Properties of Nextel 720 Fibers," Ceram. Eng. Sci. Proc. 16[5] 1005 (1995)

36. D. M. Wilson, D. C. Lueneburg and S. L. Lieder, "High Temperature Properties of Nextel 610 and Alumina-based Nanocomposite Fibers," Ceram. Eng. Sci. Proc. **14**[7] 609-621 (1993)
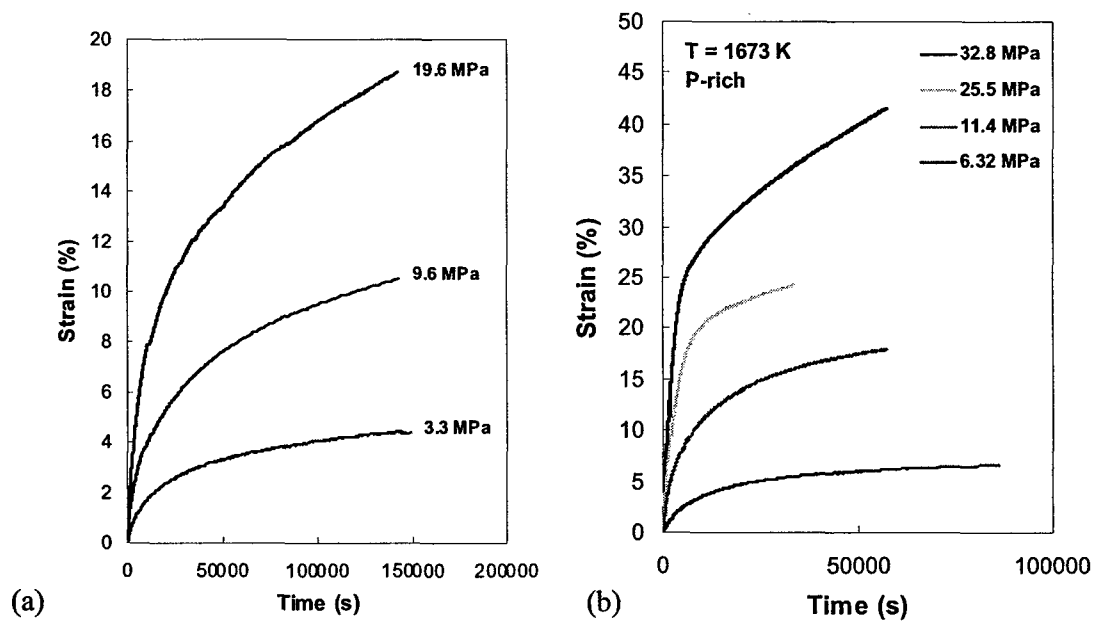
Fig. 1. Compressive creep of La-monazite at 1400 °C: (a) material with La/P=1, grain size 6 μm; (b) P-rich material , grain size 12 μm.
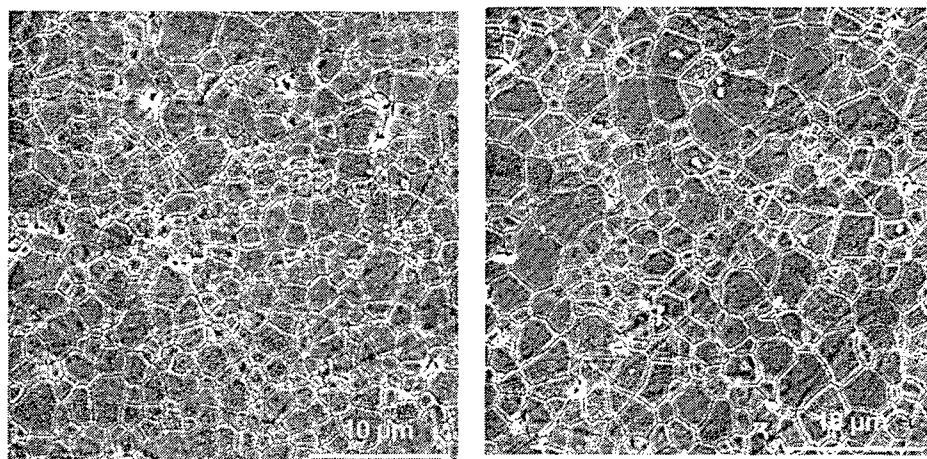
Fig. 2. Microstructures of La-monazite with La:P = 1 (a) before creep testing; (b) after creep testing (1200 °C, 30 h)
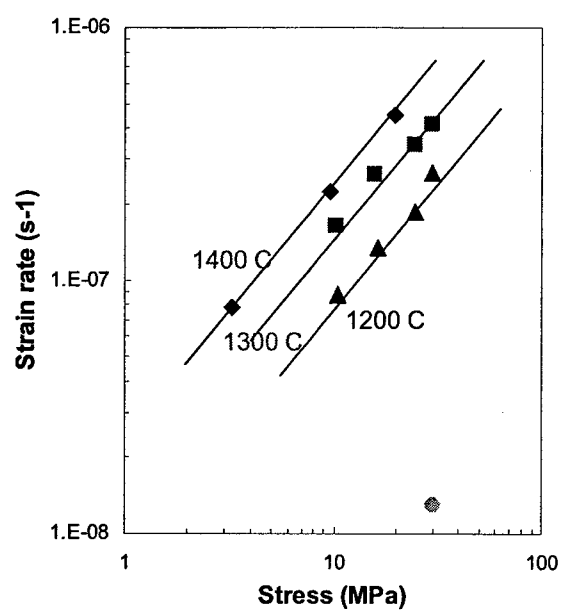
Fig. 3 Quasi-steady-state creep rates for stoichiometric La-monazite
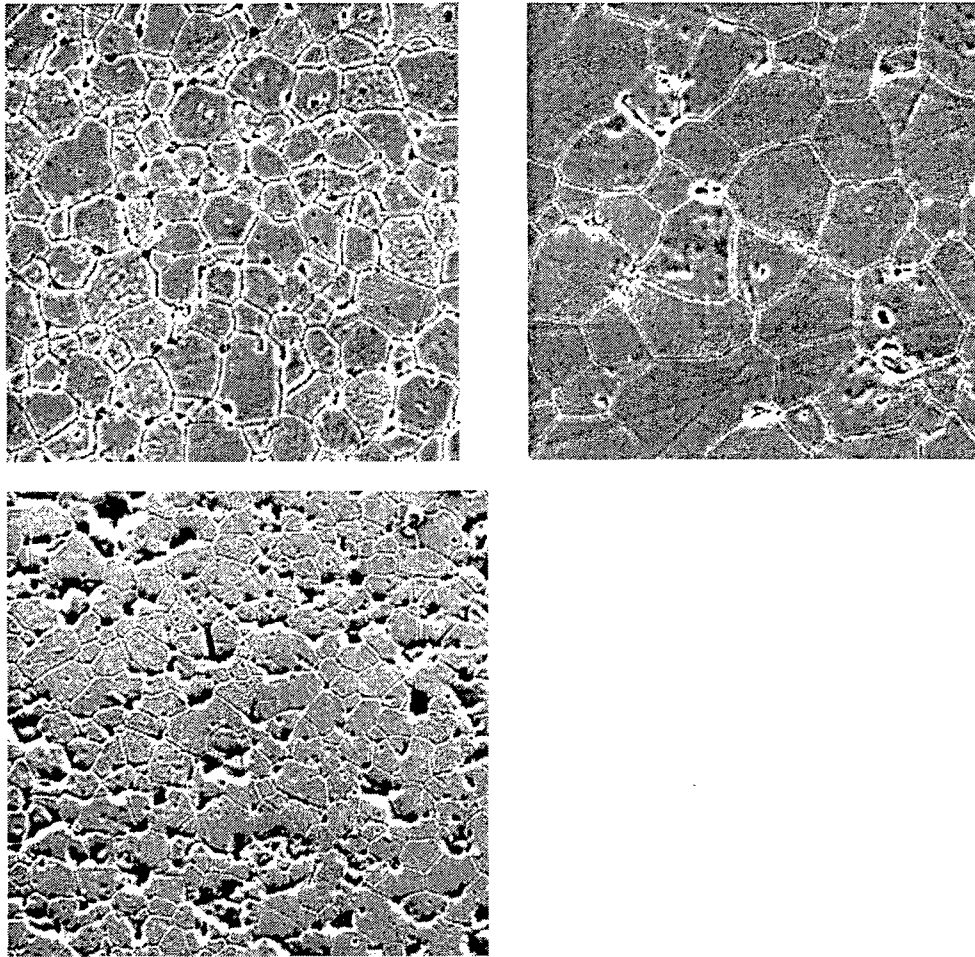
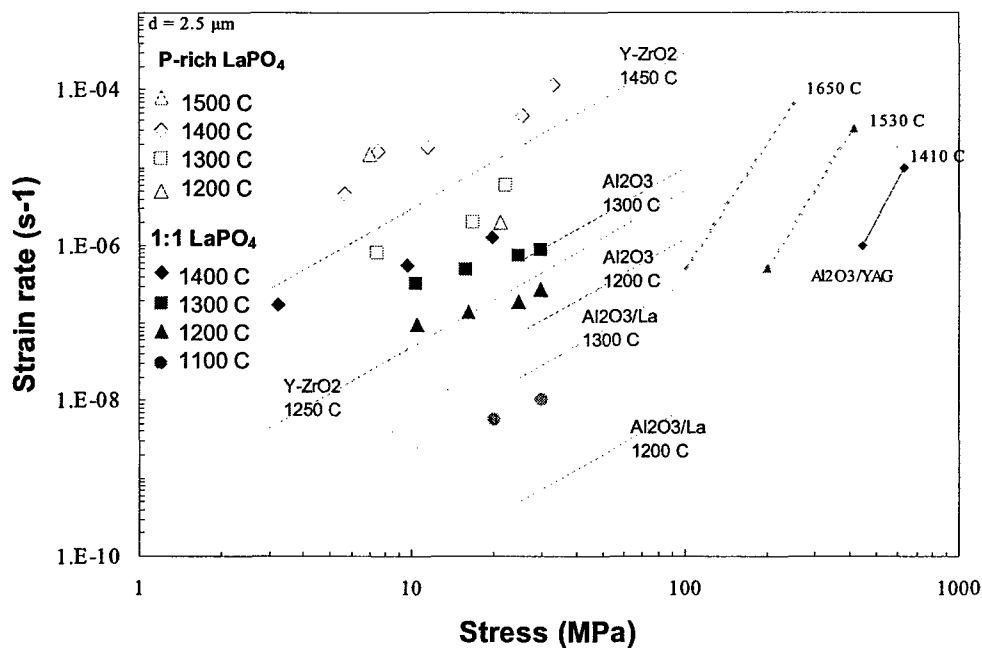Fig. 4. Microstructures of P-rich La-monazite (a) before creep testing; (b) after creep test, 1200 °C, 30 h; and (c) after creep test, 1400 °C, 17 h (stress11.4 MPa, strain 18%)

Fig. 5. Summary of creep rates for two La-monazite materials, one containing excess P and the other with La/P = 1. Creep rates adjusted to grain size of 2.5 mm using Eq. (1) to allow comparison of monazite data (symbols) with creep rates of other oxides (lines). Al_2O_3 data from Cho et al,[31] Y-ZrO$_2$ data from Melendo et al,[32] and Al_2O_3/YAG data from Parthasarathy et al.[33]
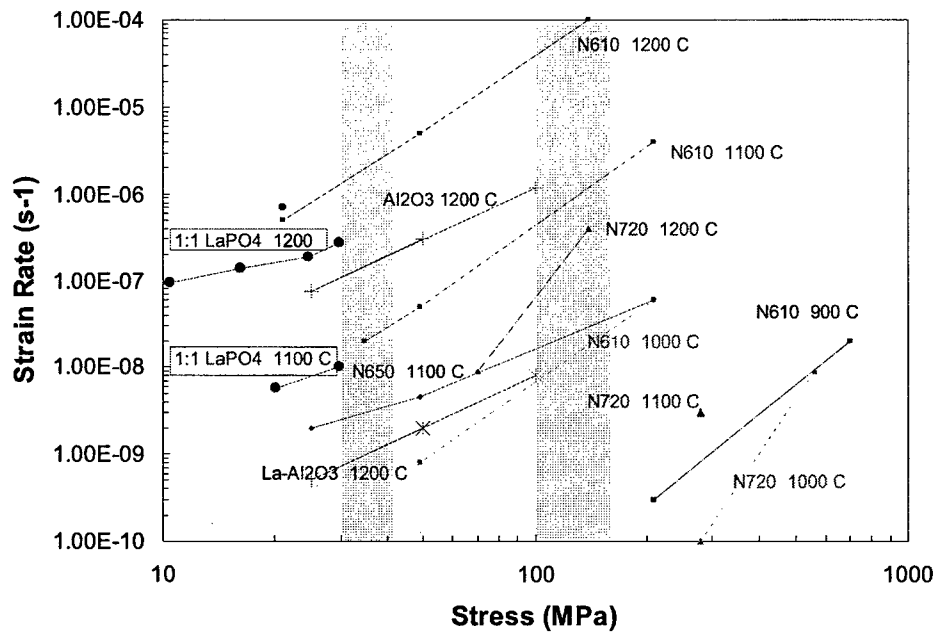
Fig. 6. Comparison of creep rates of La-monazite (La/P = 1) with literature data for various Nextel oxide fibers at temperatures up to 1200 °C (the limit to which these fibers are stable for long periods in composites). Nextel fiber data from Wilson et al.[34-36] (fiber materials are: N610 Al_2O_3, N720 mullite, and N610 doped alumina). Sintered alumina data (2.5 μm grain size), with and without La-doping, from Cho et al.[31] also included for comparison. Shaded bands represent relative elastic stresses in a composite of alumina fibers and monazite matrix or coating under iso-strain conditions (see text).
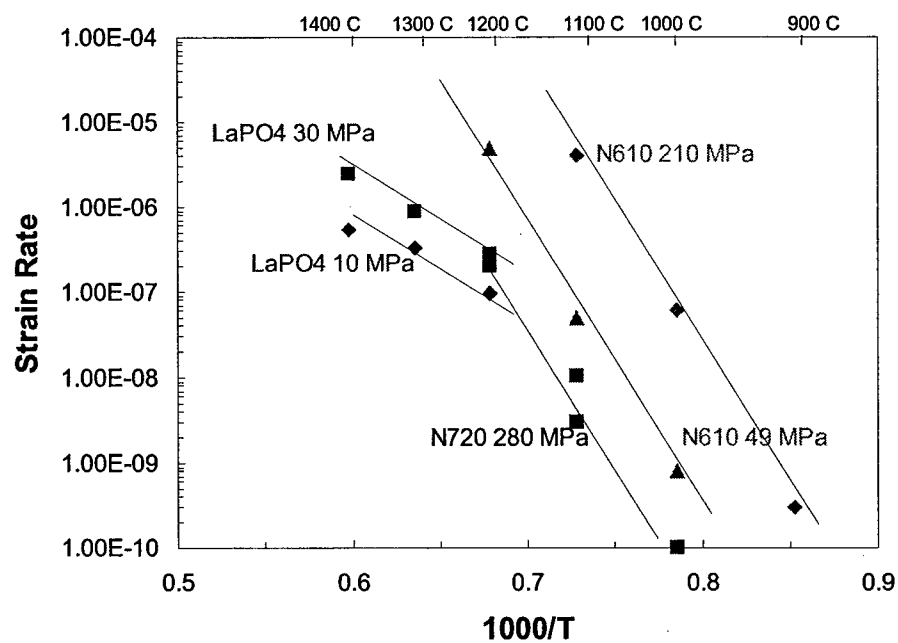
Fig. 7. Comparison of temperature dependence of creep rates of La-monazite (La/P = 1) with literature data for Nextel 610 (alumina) and Nextel 720 (mulllite) fibers.[34-36]

Section 10

Dielectric Properties of La-Monazite

by J. B. Davis, W. Ho, and D. B. Marshall
In preparation for publication as a Communication to the Journal of the American
Ceramic Society

1. INTRODUCTION

Lanthanum orthophosphate ($LaPO_4$, monazite) has a combination of mechanical and
thermal properties that make it of interest for use in various high temperature ceramic
materials, including fiber-reinforced oxide composites, machinable two-phase ceramics,
and thermal insulation systems.[1-6] The weak bonding that has been shown to occur
between $LaPO_4$ and other oxides (including Al_2O_3, ZrO_2, mullite, YAG),[1,7]as well as
relatively low resistance of $LaPO_4$ to plastic deformation,[7-10] enables damage tolerance in
fiber reinforced composites and machinability in two-phase ceramics. It is also a
refractory material, with melting point 2070°C,[11] similar to that of Al_2O_3, and is stable
and compatible in high-temperature air, vacuum, and combustion environments with
many other oxides.[12,13]

Some applications, such as resonators or low-observable structures, also require certain
dielectric properties (high or low dielectric constant, low dielectric loss). There are only
two references in the literature containing measurements of dielectric properties of
$LaPO_4$.[14,15] One of these uses natural monazite containing significant amounts of thorium
and uranium; the other uses a sintered body (2% porosity) prepared from precipitation in
molten urea. Both are restricted to frequencies lower than 10^7 Hz. In this note we report

measurements of the dielectric constant and dielectric loss factor of high purity $LaPO_4$ in the microwave region (8.2 GHz), and compare the results with measurements from less pure $LaPO_4$, from high purity commercial fibers of Al_2O_3, and a composite of Al_2O_3/$LaPO_4$.

2. EXPERIMENTAL

Measurements of room-temperature dielectric constant and loss tangent were obtained using a resonant cavity method at 8.3 GHz. Test samples were rectangular bars ~ 2.5 x 2.5 x 50 mm or rods of similar dimension.

Monolithic $LaPO_4$ test samples were fabricated by hot pressing or sintering powders that were formed by precipitation from aqueous solutions of $LaNO_3$ and phosphoric acid. Several methods were used to prepare three different materials. In one, the precipitate was washed with water, dried and calcined, and hot-pressed at 1200 °C for 1 h. This produced a material with a small excess of phosphorus (<1%), resulting from a tendency for precipitated rhabdophane ($LaPO_4.1/2H_2O$) to contain strongly bound excess phosphorus that is not removed by aqueous washing and remains as a second phase after final processing.[16] Another method involved washing the precipitated rhabdophane with a strong base to remove the excess phosphorus, and testing for the correct stoichiometry using a sensitive technique described elsewhere.[16] After adjusting the La/P ratio to unity (within ~ 500 ppm), the precipitates were dried and heated to form the monazite structure. The calcined powder was then attrition milled to form a uniform distribution of equiaxed particles with diameter less than ~ 100 nm. The particles were dispersed, consolidated by filter pressing, and sintered at 1400 °C for 2h. A third material was

produced by adding ~1% LiF as a sintering aid before filter pressing, then hot pressing at 1100 °C for 1 h. These materials were fully dense, with grain sizes ~ 1 μm in the high purity stoichiometric material, ~5 μm in the material with excess P, and ~2 μm in the material containing Li.

A test sample of commercial alumina fibers (Nextel 610, 3M company) was produced by aligning a bundle of tows (30 tows, each containing 400 fibers of diameter 12 μm) under tension and braiding the bundle with several of the same fiber tows. The fibers are polycrystalline α-Al_2O_3, with grain size ~ 100 nm. A unidirectionally reinforced alumina/monazite composite test sample was produced by filter pressing the high purity powder described above into a similar braided bundle of Nextel 610 fibers and sintering at 1200 °C for 1h. The composite consisted of ~ 50 vol. % fibers, 30 vol. % $LaPO_4$ matrix and the remainder porosity.

3. RESULTS AND DISCUSSION

The dielectric constant and loss tangent measurements are summarized in Table 1. The dielectric constant ε' of the $LaPO_4$ similar to that of alumina, and is not sensitive to the presence of excess P or Li. In contrast, the loss tangent of $LaPO_4$ increases substantially with the addition of Li and excess P, while the value for the high purity material is significantly lower than the value for alumina.

Table 1: Dielectric properties measured at 8.3 GHz

material	ε'	tanδ (x10^{-4})
$LaPO_4$, 1:1, sintered	11.8	5.3
$LaPO_4$ P-rich, HP 1200 °C	11.8	23
LaPO4 + 1% LiF, HP 1100 °C	11.2	13
Nextel 610/$LaPO_4$ composite	9	11
Nextel 610 fibers	8.7	9

Both the dielectric constant and the loss factor of the $Al_2O_3/LaPO_4$ composite are closer to the values of the fibers than to an average of the fibers and matrix. This is consistent with the expected effect of porosity in the matrix, which generally causes a decrease in ε' and increase in loss tangent.

4. CONCLUSIONS

The microwave dielectric constant and loss factor of $LaPO_4$ are similar to those of alumina. Consequently, the addition of $LaPO_4$ to alumina ceramics or alumina-based composites does not cause a significant change in dielectric properties.

ACKNOWLEDGEMENTS

REFERENCES

1. P. E. D. Morgan and D. B. Marshall, "Ceramic Composites of Monazite and Alumina," *J Am Ceram Soc,* **78** 1553-63 (1995).

2. K. A. Keller, T. Mah, T. A. Parthasarathy, E. E. Boakye and M. Cinibulk, "Evaluation of all-oxide composites based on coated Nextel 610 and 650 fibers," *Ceramic Engineering and Science Proceedings,* **22**[3] 667-75 (2001).

3. J. B. Davis, D. B. Marshall and P. E. D. Morgan, "Oxide Composites of Al_2O_3 and $LaPO_4$," *J. European Ceram. Soc.,* **19** 2421-2426 (1999).

4. T. A. Parthasarathy, E. Boakeye, M. K. Cinibulk and M. D. Perry, "Fabrication and Testing of Oxide/Oxide Microcomposites with Monazite and Hibonite as Interlayers," *J. Amer. Ceram. Soc.,* **82**[12] 3575-3583 (1999).

5. J. B. Davis, D. B. Marshall, P. E. D. Morgan and R. M. Housley, "Machinable Ceramics Containing Rare-Earth Phosphates," *J. Am. Ceram. Soc.,* **81**[8] 2169-75 (1998).

6. Davis JB, Marshall DB, Oka KS, Housley RH, Morgan PED: Ceramic Composites for Thermal Protection Systems. *Composites: Part A* 1999, **30:** 483-488 .

7. Davis, J. B., Hay, R. S., Marshall, D. B., Morgan, P.E.D., and Sayir, A., "The Influence of Interfacial Roughness on Fiber Sliding in Oxide Composites with La-Monazite Interphases," J. Am. Ceram. Soc., 86[2] 305-316 (2003)

8. Hay, R. S. and Marshall, D. B., "Deformation Twinning in Monazite," Acta Mat. **51**[18] 5235-5254 (2003)

9. R. S. Hay, "Monazite and Scheelite Deformation Mechanisms," *Ceram. Eng. Sci. Proc.* 21**, 203–18 (2000).**

10. R. S. Hay, "(120) and (122) Monazite Deformation Twins," *Acta Mater.* **51**, 5255–62 (2003).

11. Y. Hikichi and T. Nomura, "Melting Temperatures of Monazite and Xenotime," *J. Am. Cer. Soc.,* **70**[10] C252-C253 (1987).

12. D. B. Marshall, P. E. D. Morgan, R. M. Housley and J. T. Cheung, "High temperature Stability of the Al_2O_3-$LaPO_4$ System," *J. Am. Ceram. Soc.,* **81**[4] 951-56 (1998).

13. J. B. Davis, D. B. Marshall, O. Sudre, and E. Opila, "High temperature stability of $LaPO_4$ in Water Vapor, Vacuum, and CO environments," in preparation for J. Am. Ceram. Soc.

14. B. Narisimha, R. N. P. Choudhary and K. V. Rao, "Dielectric Properties of LaPO$_4$ Ceramics," J. Mat. Sci., **23** 1416-18 (1988)

15. M. M. Abdel-Aal, M. A. Ahmed, and L. Ateya, "Temperature and Frequency Dependence of Dielectric Constant and Conductivity of Natural Egyptian Monazite," J. Phys. Soc. Japan **65**[10] 3351-56 (1996)

16. 30. Davis, J. B., Sudre, O., Marshall, D. B., Morgan, P.E.D., and Housley, R., "The Synthesis and Processing of La-monazite" in preparation for J. Am. Ceram. Soc.

Section 11

Directionally Solidified Structures of LaPO$_4$/Al$_2$O$_3$

by A. Sayir, and D. B. Marshall and J. B. Davis
Paper in preparation for publication the Journal of the American Ceramic Society

1. INTRODUCTION

In the search for ultra-high-temperature materials that are stable in oxidizing environments, directionally solidified eutectic oxides stand out. They are both thermodynamically stable in oxidizing environment and microstructurally stable very close to their melting point. Moreover, the two-phase interlocking microstructures provide constraint and barriers to deformation and creep, with the result that their strength and creep resistance at very high temperatures can be higher than that of either of the constituent phases alone. Various eutectic materials based on Al$_2$O$_3$, ZrO$_2$, Y$_3$Al$_5$O$_{12}$ (YAG), Er$_3$Al$_5$O$_{12}$ and GdAlO$_3$ have shown high strength and creep resistance at temperatures several hundred degrees centigrade above those attainable for conventional polycrystalline oxides.[1-10]

One drawback of directionally solidified structures fabricated to date is that they are brittle. In all cases there is strong bonding at the interface between the two phases; and both individual phases are brittle, so that a crack is able to grow through the body without interacting with the microstructure, similar to the case in glass or in single-phase ceramics. An example in an Al$_2$O$_3$/YAG directionally solidified material is shown in Fig. 1, where a crack formed by loading a Vickers diamond indenter onto the surface is clearly unaffected by the boundary between the Al$_2$O$_3$ and YAG.

This paper describes a preliminary study to assess the feasibility of creating toughened directionally solidified materials (eutectic or non-eutectic) by introducing a phase that interacts with a growing crack to deflect it or to create secondary cracking that impedes

its growth. The approach is based on use of $LaPO_4$ as one of the phases(specifically $Al_2O_3/LaPO_4$), which is known to form a sufficiently weak interface with other oxides that debonding occurs whenever a crack approaches an interface from within the phosphate.[11] This mechanism has been demonstrated in fiber reinforced composites based on alumina and mullite fibers.[12-15] In that case, the useful temperature for the composite is limited by microstructural stability of the fibers, whereas in the directionally solidified system this limitation would not exist. Some of the results point to the possibility of materials with a layered crystal structure and highly anisotropic fracture properties serving the same purpose,[16,19] specifically La-hexaluminate, $LaAl_{11}O_{18}$, which has very low fracture toughness on the basal plane.

For the growth of directionally solidified multiphase materials, systems with low vapor pressures near and above the melting point are preferred. In this regard the growth of $Al_2O_3/LaPO_4$ is expected to be difficult, because of the relatively high volatility of P_2O_5. This is indeed found to be the case. Nevertheless, some encouraging results are found.

2. EXPERIMENTS AND RESULTS

Test samples in the form of rods ~200 to300 μm in diameter were grown at NASA Glenn by a laser-heated float zone technique,[7,8] in air, using source rods produced from mixtures of Al_2O_3 and $LaPO_4$ powders. Some evaporation of P was evident during the experiments. Several rates (ranging over a factor of 3)were used for pulling the rods from the melt in an attempt to reduce the time available for loss of phosphorus. The alumina used in the source rods was commercial high purity powder (Sumitomo AKP-50). The $LaPO_4$ powder was produced by precipitation from aqueous solutions of $LaNO_3$ and phosphoric acid. The precipitates were washed, dried and calcined, redispersed and attrition milled, mixed with the alumina powder and ball milled. By varying the washing procedure the $LaPO_4$ can be made with varying small amounts excess of phosphorus (<1%).

The test samples were sectioned , polished, and in some cases thermally etched , then analyzed by scanning electron microscopy (SEM) and EDS. A range of different microstructures and phase mixtures were observed, containing various mixtures of Al_2O_3, $LaAlO_3$, $LaAl_{11}O_{18}$, and $LaPO_4$. In SEM images, both secondary and backscattered, these phases appear with three distinct and easily identified brightness levels: the darkest being Al_2O_3, the intermediate grey level being $LaAl_{11}O_{18}$, and the lightest being $LaAlO_3$ and $LaPO_4$. The last two require EDS analysis to identify them as their image intensity levels are indistinguishable.

At the faster pulling rates the directionally solidified microstructure consisted of mostly Al_2O_3 and $LaPO_4$. A polished axial cross section from the feed rod through melt boundary and into the solidified microstructure is shown in Fig. 2. EDS analysis indicated that the lighter phase in the directional microstructure is $LaPO_4$ and the darker phase is Al_2O_3. Some large scale porosity is evident in regions that had melted, especially near the melt boundary. Some of this may be coarsening of fine scale porosity in the feed rod, although some may be due to evaporation.

Higher magnification images from the directional microstructure are shown in Fig. 3. A second finer scale microstructure is evident in Fig. 3b within the $LaPO_4$ phase. This is most likely alumina, although the size is too small for direct analysis by EDS in the SEM. (EDS analysis of the $LaPO_4$ regions showed a small amount of aluminum which could originate from the fine-scale dark phase or from the surrounding coarser Al_2O_3 phase. After heat treating at 1400 °C for 1h, there was no change to the coarser microstructure (Fig. 3c), whereas the fine-scale dark phase within the $LaPO_4$ showed some coarsening (Fig. 3d). The thermal grooving of the surface evident in Fig. 3c indicates that all of the connected regions of alumina are single crystal, whereas the $LaPO_4$ regions are polycrystalline with grain size less than 1 μm.

After the heat treatment leading to Figs. 3c and 3d, a Vickers diamond indenter was loaded on the surface to generate localized cracks. Interactions of these cracks with the microstructure are shown in Fig. 4. A clear tendency is evident for the cracks to follow

the $LaPO_4$ phase and to cause debonding at the interface between the $LaPO_4$ and Al_2O_3 when the crack impinges upon the boundary from within the $LaPO_4$, even when the incident angle is high.

Further along the solidified rod from the melt boundary of Fig.2, where steady state conditions prevailed, the microstructure was more directional as shown in Fig. 5 and quite uniform over large distances. Examples of phase analysis by EDS within the lighter phase are shown in Figs. 5b to e. Most of these regions are $LaPO_4$, although substantial amounts of $LaAlO_3$ are also present.

At the other end of the rod near the seed, where the steady state velocity had not been reached, the phosphorus loss was greater and the microstructure consisted mostly of Al_2O_3 and $LaAl_{11}O_{18}$, with a small amount of $LaPO_4$ within the $LaAl_{11}O_{18}$ phase (Fig. 6). The $LaPO_4$ was always in thin parallel plates, presumably aligned with the basal plane of the $LaAl_{11}O_{18}$. The $LaAl_{11}O_{18}$ /$LaPO_4$ regions showed very anisotropic fracture properties (Fig. 6a) with crack deflection and propagation along the thin $LaPO_4$ plates.

Similar microstructures with smaller relative amounts of $LaPO_4$ were observed in other rods produced at lower pulling velocity (Fig. 7). In this case highly anisotropic fracture behavior was seen in the $LaAl_{11}O_{18}$ phase. suggesting that this phase could also possibly be used to provide toughening.

3. CONCLUSIONS

Directionally solidified materials consisting of various combinations of Al_2O_3, $LaPO_4$, $LaAl_{11}O_{18}$ and $LaAlO_3$ have been formed in air from feed material of sintered Al_2O_3/$LaPO_4$. The phases present are dependent on the rate of formation: slower rates allow evaporation of P and formation of $LaAl_{11}O_{18}$ and $LaAlO_3$, whereas faster rates minimize loss of P and allow formation of microstructures consisting mostly of Al_2O_3/$LaPO_4$. The formation of controlled directionally solidified microstructures in this

system will most likely require controlled atmosphere over the molten material to minimize evaporation of P.

Preliminary observations of indentation cracking in directionally solidified $Al_2O_3/LaPO_4$ material indicates that debonding and deflection of cracks occurs at the boundaries between the Al_2O_3 and $LaPO_4$, as required for toughening. In materials containing $LaAl_{11}O_{18}$ and Al_2O_3 highly anisotropic fracture behavior was seen in the $LaAl_{11}O_{18}$ phase. The results suggest that further development of this system may be worthwhile.

ACKNOWLEDGEMENTS

REFERENCES

1. T. A. Parthasarathy, T. Mah and L. E. Matson, "Deformation Behavior of an Al_2O_3-$Y_3Al_5O_{12}$ Eutectic Composite in Comparison with Sapphire and YAG," J. Am. Ceram. Soc., **76**[1] 29-32 (1993)

2. Mah, T.; Parthasarathy, T.A.; Petry, M.D.; Matson, L.E. "Processing microstructure, and properties of Al_2O_3-$Y_3 Al_5O_{12}$ (YAG) eutectic fibers," Ceramic Engineering and Science Proceedings 14 [7-8] 622-638 (1993)

3. Harada Y., Suzukit., Hirano K. and Waku Y., "Ultra-high temperature compressive creep behavior of an in-situ Al_2O_3 single-crystal/YAG eutectic composite," J. European Ceram. Soc., 24[8] 2215-2222 (2004)

4. Waku Y., Sakata S., Mitani A., Shimizu K. and Hasebe M., "Temperature dependence of flexural strength and microstructure of $Al_2O_3/Y_3Al_5O_{12}$ /ZrO_2 ternary melt growth composites," J. Mat. Sci., 37 [14] 2975-2982 (2002)

5. Ochiai S., Ueda T., Sato K., Hojo M., Waku Y., Nakagawa N., Sakata S., Mitani A. and Takahashi T., "Deformation and fracture behavior of an Al_2O_3/YAG composite from room temperature to 2023 K" Composites Sci. and Tech , , 61[14] 2117-2128 (2001).

6. Waku, Y., Nakagawa, N., Ohtsubo, H., Mitani, A. and Shimizu, K., "Fracture and deformation behaviour of melt growth composites at very high temperatures," J. Mat. Sci. 36[7] 1585-94 (2001)

7. A. Sayir, "Directional Solidification of Eutectic Ceramics"; pp 197-211 in Computer Aided Design of High Temperature Materials. Eds A. Pechenik, R. Kalia and P. Vashishta. Oxford, Oxford University Press, 1999.

8. A. Sayir and S. C. Farmer, "Directionally Solidified Mullite Fibers," *Mat. Res. Soc. Proc.,* **365** 11-21 (1995).

9. A. Sayir and S. C. Farmer, "The Effect of the Microstructure on Mechanical Properties of Directionally Solidified Al2O3/ZrO2(Y2O3) Eutectic," *Acta Mater.,* **48**[18-19] 4691-97 (2000).

10. A. Sayir and L. E. Matson, "Growth and Characterization of Directionally Solidified Al2O3/Y3Al5O12 (YAG) Eutectic Fibers," *Proc. of the 2nd Ann. HITEMP Rev,* **83** 1-14 (1991).

11. P. E. D. Morgan and D. B. Marshall, "Ceramic Composites of Monazite and Alumina," *J Am Ceram Soc,* **78** 1553-63 (1995).

12. J. B. Davis, D. B. Marshall and P. E. D. Morgan, "Oxide Composites of Al_2O_3 and $LaPO_4$," *J. European Ceram. Soc.,* **19** 2421-2426 (1999).

13. J. B. Davis, D. B. Marshall and P. E. D. Morgan, "Monazite Containing Oxide-Oxide Composites," *J. Eur. Ceram. Soc.,* **20**[5] 583 - 587 (2000).

14. K. A. Keller, T.-I. Mah, E. E. Boakye and T. A. Parthasarathy, "Gel-Casting and Reaction Bonding of Oxide-Oxide Minicomposites with Monazite Interphase," *Ceramic Engineering and Science Proceedings,* **21**[4] 525-534 (2000).

15. T. A. Parthasarathy, E. Boakeye, M. K. Cinibulk and M. D. Perry, "Fabrication and Testing of Oxide/Oxide Microcomposites with Monazite and Hibonite as Interlayers," *J. Amer. Ceram. Soc.,* **82**[12] 3575-3583 (1999).

16. Morgan, P.E.D., and Marshall, D.B., "Functional Interfaces in Oxide-Oxide Composites," J. Mat. Sci. Eng. A162, 15-25 (1993).

16. Cinibulk MK, " Hexaluminates as a Cleavable Fiber-Matrix Interphase: Synthesis, Texture Development, and Phase Compatibility." *J. Eur. Cer. Soc.* 2000, **20:** 569-582 .

17. Cinibulk MK, " Effect of Divalent Cations on the Synthesis of Citrate-Gel-Derived Lanthanum Hexaluminate Powders and Films." *J. Mater. Res.* 1999, **14:** 3581-3593 .

18. Saruhan B, Schneider H, Komarneni S, Abothu IR, "Electrostatically deposited surface seeding and promotion of crystallization of sol-gel derived La $Al_{11}O_{18}$ coating on oxide fibers." *J. Eur. Ceram. Soc.* 1999, **19:** 2427-2435.
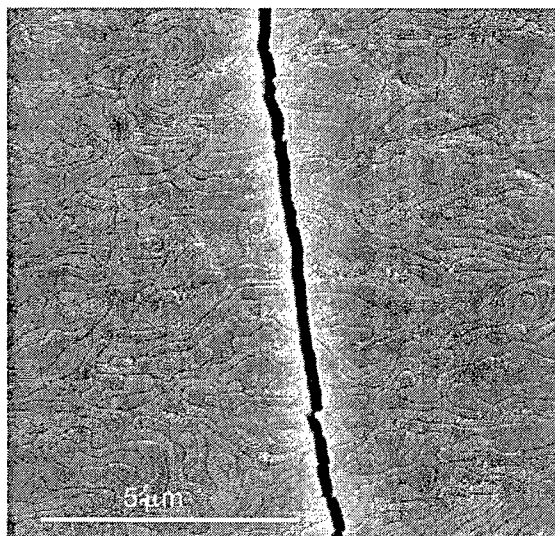
Fig. 1. Crack produced by loading a Vickers indenter on the polished/etched surface of a directionally solidified Al_2O_3/YAG material (SEM micrograph). Etch marks on surface show boundaries between the two interconnected Al_2O_3 and YAG phases.

Fig. 2. Polished cross section from feed rod (bottom) through melt boundary to solidified microstructure (top). Darker phase Al_2O_3, lighter phase $LaPO_4$.
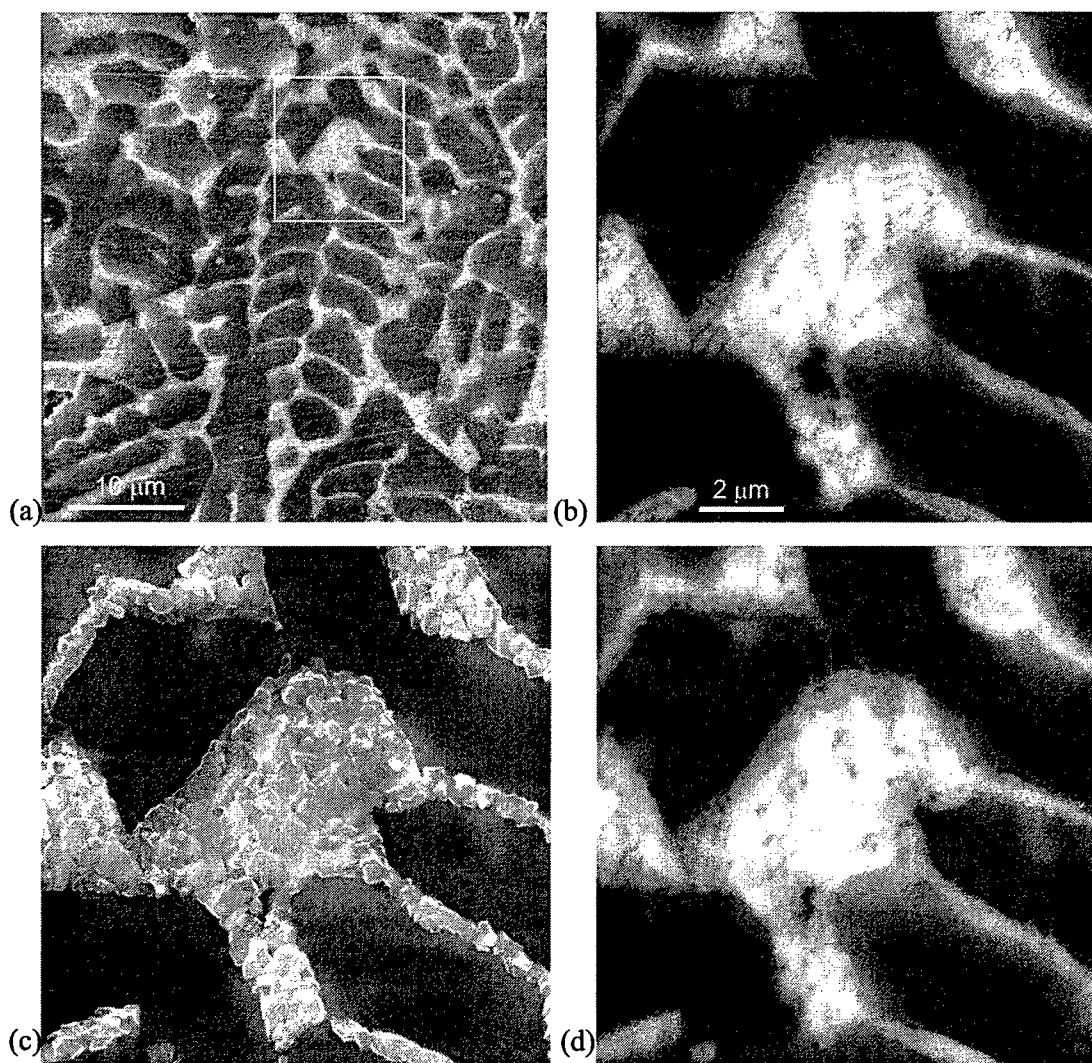
Fig. 3. Higher magnification from region outlined by white square in Fig. 2: (a) secondary electron image; (b) backscattered electron image from region marked in (a); (c) and (d) secondary and backscattered electron images from same area as (b) after being heat treated at 1400 °C for 1 h. Darker phase Al_2O_3, lighter phase $LaPO_4$.

(a)

(b)

(c)
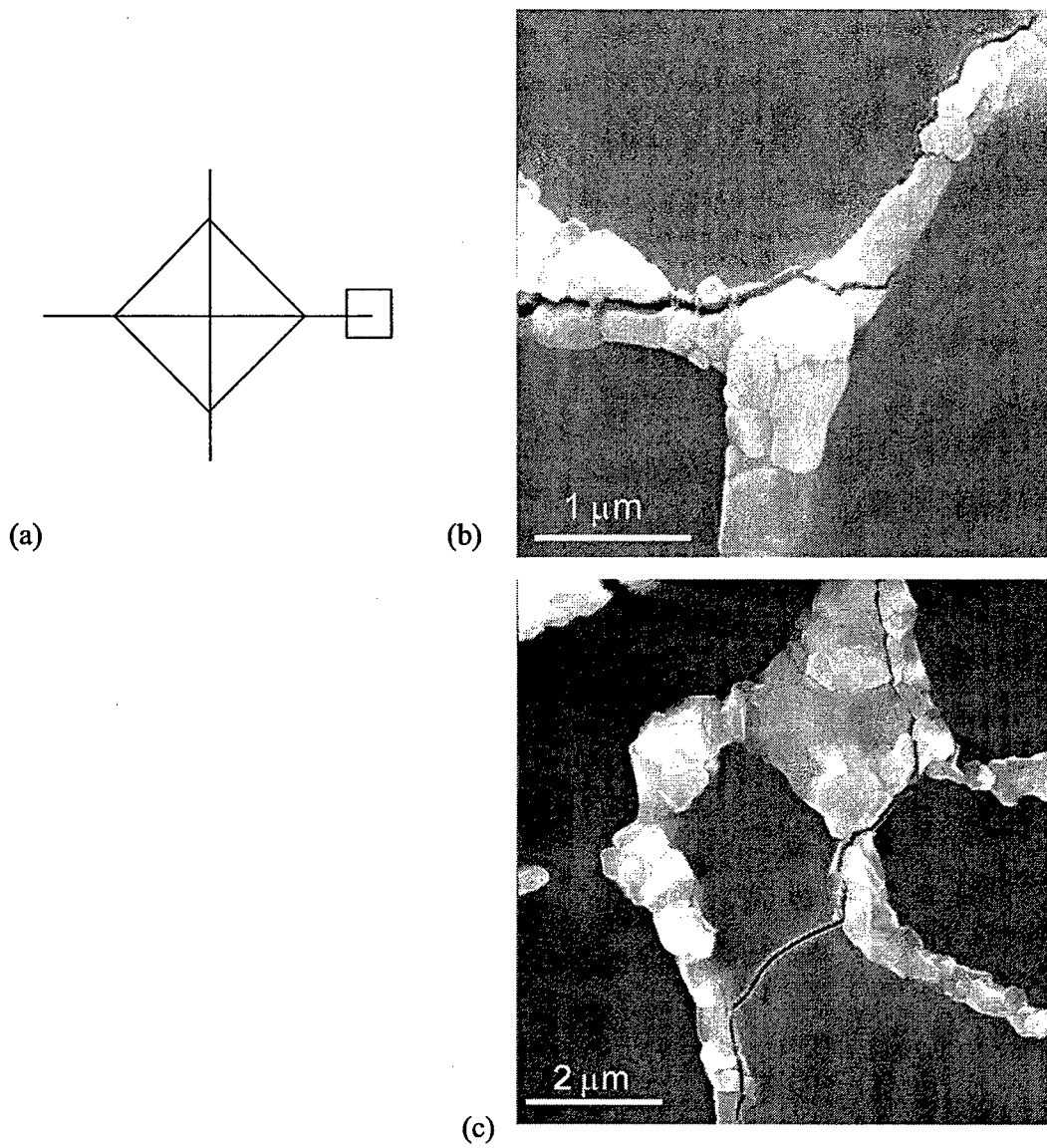
Fig. 4. Indentation induced cracking in same region as Fig. 3: (a) schematic showing location of indentation relative to micrographs in (b) and (c). Darker phase Al_2O_3, lighter phase $LaPO_4$.
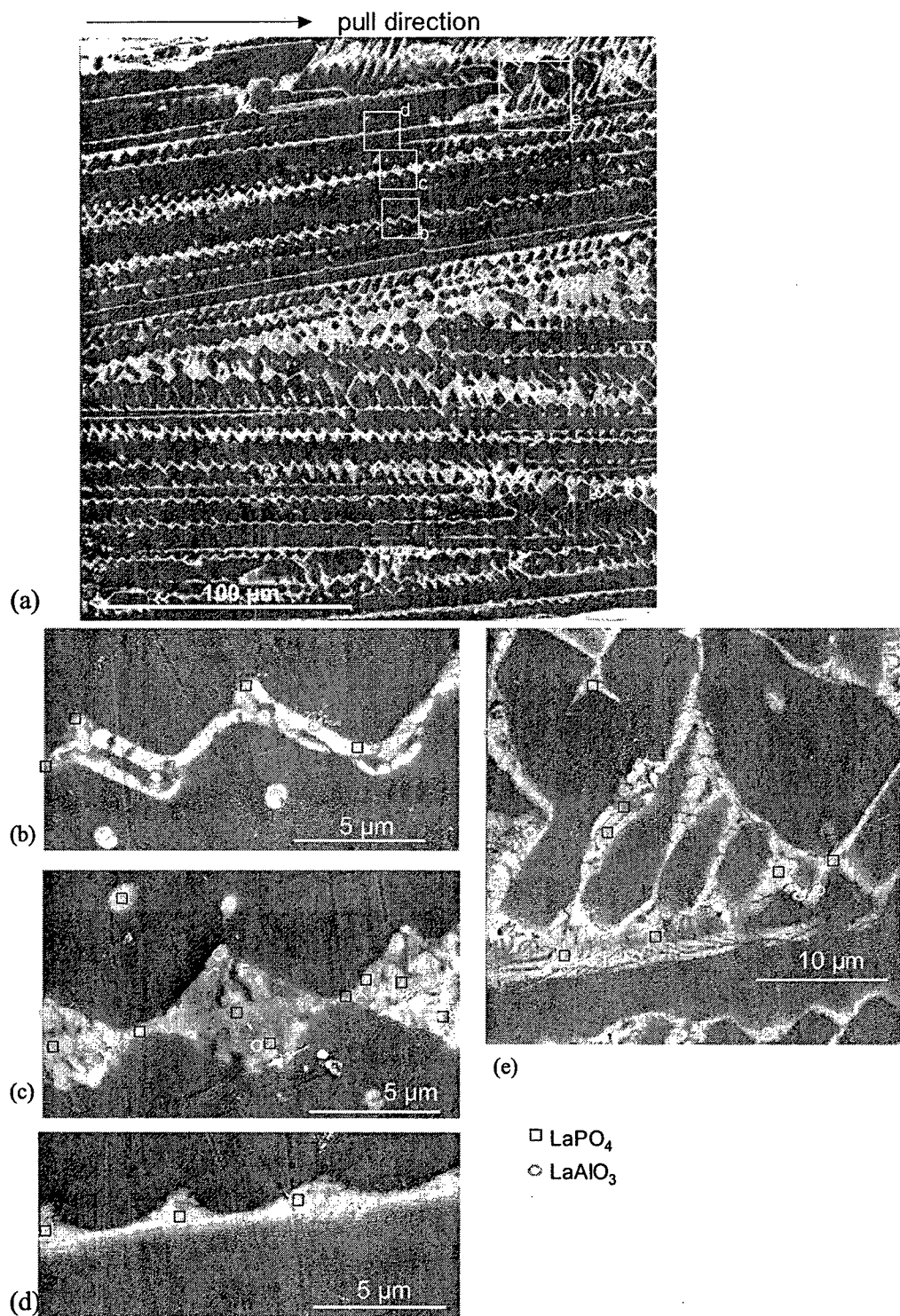
Fig. 5. (a) Typical microstructure from same rod as Fig. 2, but further along the directionally solidified region. (b)-(e) Higher magnification of areas marked in (a) showing results of EDS analysis: darker phase is Al_2O_3, lighter phase is $LaPO_4$ or $LaAlO_3$
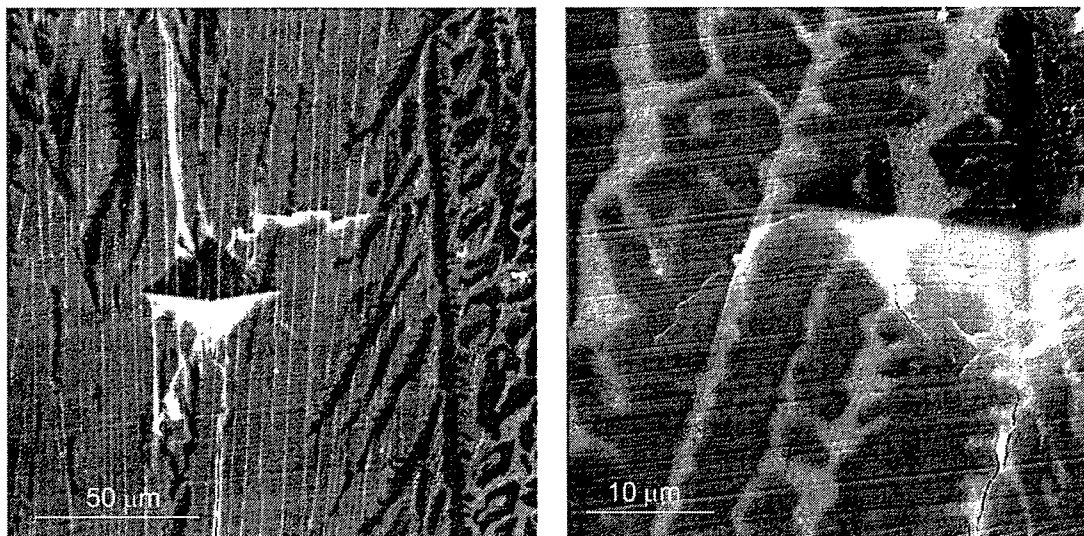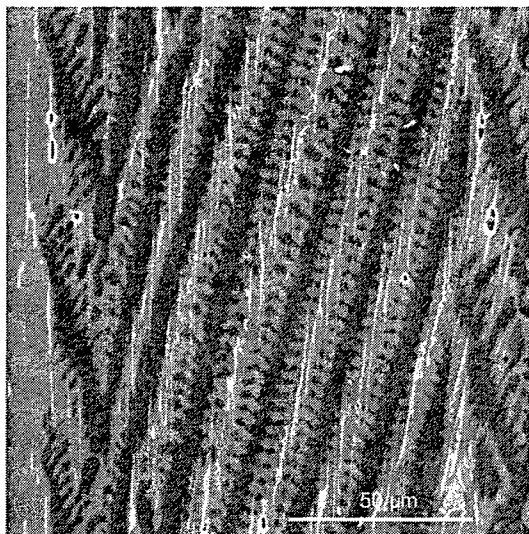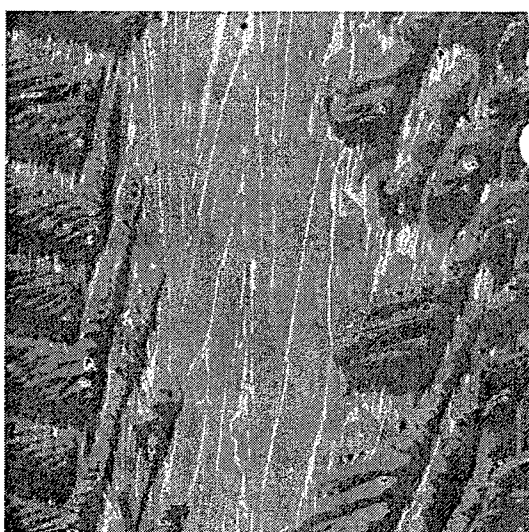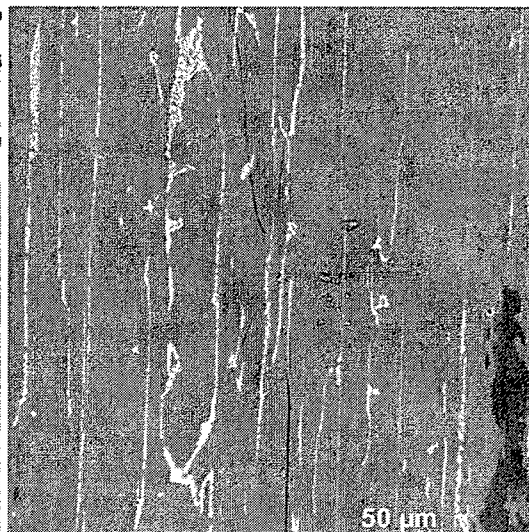
Fig. 6. Indentation cracking in directionally solidified region containing Al_2O_3 (darkest phase), $LaAl_{11}O_{18}$ (intermediate grey) and $LaPO_4$ (light).

Fig. 7. (a) and (b): directionally solidified microstructures containing Al_2O_3 (darkest phase), $LaAl_{11}O_{18}$ (intermediate grey) and $LaAlO_3$ (light). (c) Cracks produced by Vickers indenter (indentation only faintly visible in center of micrograph).

Ceramics: Transformation Toughening

Tetragonal zirconia (ZrO_2) undergoes a martensitic transformation to the monoclinic phase, accompanied by $\sim 9°$ shear and 4% volume increase. With suitable microstructural design, the fracture toughness of brittle ceramics containing zirconia can be increased by up to an order of magnitude by a mechanism that involves activation of this transformation locally near the tips of cracks. The toughening mechanism, which is similar to that occurring in TRIP steels, was first reported by Garvie et al. (1975). Although the toughness achieved in these ceramics remains well below that typical of ductile metals, the increase is sufficient to allow their use in a wide variety of applications that benefit from the superior hardness, stiffness, or chemical resistance of the ceramic, but would otherwise be precluded by the risk of failure by fracture.

1. Constrained Transformation

Upon cooling from high temperature, pure zirconia undergoes two phase transformations, from cubic (c) to tetragonal (t) crystal structure at $\sim 2367°C$ and from tetragonal to monoclinic (m) structure at $\sim 1170°C$. The t–m transformation is martensitic and is accompanied by a large shear strain and volume increase. In many practical cases the net shear strain is reduced or eliminated by twinning or by the formation of several variants. Both transformation temperatures can be reduced by alloying with other oxides (e.g., MgO, Y_2O_3, CaO, Ce_2O_3, or other rare-earth oxides) that form solid solutions with ZrO_2.

The t–m transformation temperature can also be reduced by mechanical constraint that opposes the accompanying shape and volume changes. The thermodynamics of the phase transformation for a particle of ZrO_2 embedded in an elastic matrix then involves a balance of two terms: a decrease in chemical free energy accompanying the transformation and an increase in elastic strain energy in both the particle and the matrix. The magnitude of the former increases with decreasing temperature, while the latter is, to first order, independent of temperature. If the magnitude of the strain energy term is sufficiently large, the transformation can be suppressed to cryogenic temperatures. The strain energy can be increased or decreased by the action of a remotely applied stress field (the interaction energy in the analyses of Eshelby (1957)) and the transformation temperature correspondingly changed.

Experimental observations indicate the existence of a size effect in the t–m transformation, which is key to designing toughened microstructures. For a given system of embedded ZrO_2 particles at a given temperature, there exists a critical particle size above which all particles transform spontaneously to the monoclinic phase, and below which the tetragonal phase is stable. The critical particle size decreases with decreasing temperature. Since both of the energy terms mentioned above scale with volume, the existence of a size effect requires either an additional energy term that scales differently with size, or that the transformation be controlled by a nucleation barrier.

Several possibilities exist for energy terms that scale with particle surface area (localized strain energy associated with terminations of twins, as observed in monoclinic particles, and differences in interfacial energies between the matrix and the t or m phases). However, evidence exists for nucleation control in some cases that is dependent on strain concentrations associated either with second phase particles or with the shape of the ZrO_2 particle itself. In the absence of definitive experiments to distinguish these possibilities, the critical conditions for the onset of the t–m transformation remain the least well understood aspect of the transformation and of the associated theoretical predictions of transformation toughening.

Although the martensitic t–m transformation is reversible, hysteresis is observed during temperature cycling, i.e., the martensitic start temperature (M_s) for the forward transformation is lower than the temperature for the reverse transformation (A_s). Hysteresis is also usually observed in experiments involving isothermal stress-induced transformation. Among the potential causes of hysteresis is the formation of microcracks around transformed particles (stabilization by relief of strain energy) or the effect of nucleation steps in the forward and reverse directions.

2. Toughening Mechanism

Transformation toughening requires a microstructure containing stabilized t-ZrO_2 particles with M_s below ambient temperature. The toughening involves the formation of a zone surrounding a growing crack in which the t–m transformation is induced by the concentrated stresses near the crack tip (Fig. 1). The transformation strains give rise to closure stresses on the crack, or, in terms of the fracture mechanics formulation, a negative stress intensity factor, K_T, which superimposes on the remotely applied stress intensity factor, K_a, thus opposing further crack growth. In this way the measured fracture toughness is increased by a crack shielding mechanism, while the fundamental brittle bond rupture processes at the crack tip are unchanged.

The contribution of the transform strain to toughening is dependent on the location of the transformed particle relative to the crack tip. For example, in the case of a net dilatational transformation strain, a particle located ahead of the crack (at $\theta < 60°$ in Fig. 1(b)) causes additional tensile stresses ahead of the crack tip (and thus reduced toughening), while a particle behind the crack tip (at $\theta > 60°$ in Fig. 1(b))
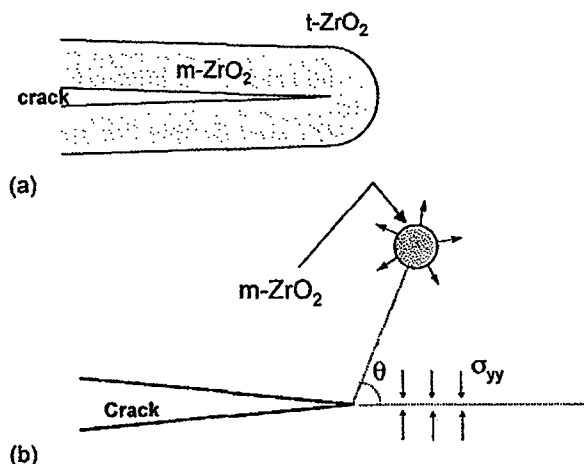
1

(a)

(b)

Figure 1
Schematics of transformation toughening: (a) well developed transformation zone surrounding crack; (b) effect of individual transformed particle on stresses ahead of crack tip.

Figure 2
Measured strengths and toughnesses for several series of transformation-toughened ceramics (adapted from Swain 1985).

3. Microstructures and Properties of Transformation-toughened Ceramics

While many transformation-toughened microstructures have been investigated, those developed commercially are of three distinct types.

(i) Partially stabilized zirconia (PSZ) consists of coherent t-ZrO$_2$ precipitates in a matrix of cubic zirconia. The precipitated microstructure is developed
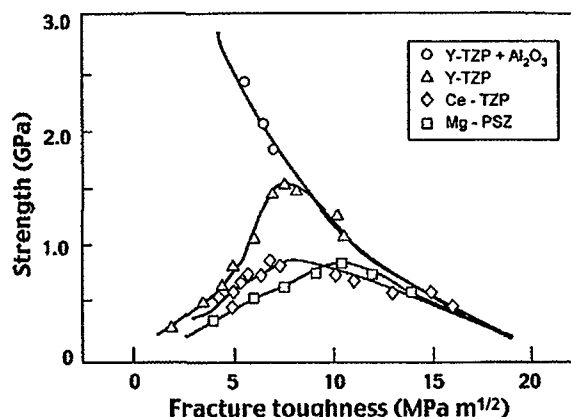
causes compressive stress. This implies that, to achieve effective toughening, the reverse m–t transformation should not occur upon removal of the crack-tip stress field, so that a wake of transformed material develops as the crack grows, as indicated in Fig. 1(a). A second implication is that the toughening effect for a preexisting crack will initially increase as the crack grows and the wake develops, before approaching a steady state condition (i.e., R-curve behavior).

The boundary of the transformation zone is determined by the critical stress required to induce the t–m transformation. This stress and, thus, the zone width and the degree of toughening are sensitive to temperature as well as microstructure. The optimum toughening is achieved when the critical stress is small, i.e., when the ambient temperature is above but close to the M_s temperature. This requirement also defines one of the limitations on the application of this toughening mechanism since, although large toughness increases are possible, the mechanism is effective only over a small range of temperatures.

by adding a stabilizing solute (MgO, CaO, or Y$_2$O$_3$) at concentrations smaller than needed for full stabilization of the cubic phase, sintering at high temperature ($\sim$ 1600–1800 °C) in the cubic phase field, generally resulting in large c-ZrO$_2$ grains ($\sim$ 35–100 μm), and heat treating during cooling in the temperature range $\sim$ 1100–1500 °C to nucleate and grow the precipitates. In Mg–PSZ the precipitates are oblate spheroids with optimum dimensions $\sim$ 50 × 200 nm.

(ii) Tetragonal zirconia polycrystals (TZP) consist of a matrix of fine-grained (0.1–1 μm), predominantly single-phase t-ZrO$_2$ with additions of Y$_2$O$_3$, Ce$_2$O$_3$, or other rare-earth oxides. Sintering is carried out in the single phase t-ZrO$_2$ field at temperatures in the range $\sim$ 1300–1500 °C for alloys containing 1.5–3.5 mol.% Y$_2$O$_3$.

(iii) Zirconia-toughened ceramics (ZTC) consist of t-ZrO$_2$ particles dispersed (usually intergranularly) in a matrix of another ceramic such as alumina (Al$_2$O$_3$) or mullite (3Al$_2$O$_3$.2SiO$_2$). A small amount of Y$_2$O$_3$ is usually added to the ZrO$_2$ particles to stabilize the t-phase. The critical particle size is usually between $\sim$ 0.5 and 1 μm depending on the amount of Y$_2$O$_3$ additive and the matrix.

Zirconia-toughened materials have the highest strengths (> 2 GPa) and toughnesses (> 15 MPa m$^{1/2}$) of any polycrystalline ceramics. However, the highest strengths and toughnesses are not found in the same materials (Fig. 2). In each of the systems described above, for given stabilizing solute content, can be varied by adjusting the heat treatment to change the critical stress for transformation, and in most cases the strength is maximum at an intermediate toughness. In the materials with the highest toughness (Mg–PSZ and Ce–TZP) the critical stress for transformation is $\sim$ 500 MPa and trans-

2

formation zones with widths up to about 1 mm have been observed around well-developed cracks. However, the transformation stress apparently places an upper limit on the strength of the material, for even in the absence of pre-existing cracks, bands of transformation induced by the applied stress lead to failure. The materials with the highest strengths (Y–TZP and zirconia-toughened alumina) have lower toughnesses ($\sim$ 5–8 MPa m$^{1/2}$) and correspondingly smaller zone widths ($<$ 10 μm).

Additional improvements in properties can be gained by surface grinding. The t–m transformation is induced within a layer near the surface by localized grinding stresses, resulting in a layer of residual compressive stress. The compressive stress inhibits crack initiation and can improve strength, wear resistance, and thermal shock resistance.

Figure 3
Components of transformation-toughened zirconia (Mg–PSZ and Y–TZP).

4. Theoretical Understanding of Transformation Toughening

A weight-function method has been used to calculate the reduction in stress intensity factor, K_T, (i.e., the toughness increase) in terms of the distribution of transformation strains surrounding the crack (McMeeking and Evans 1982). When the transformation strain, e^T, and volume fraction, v_t, of transformed particles are uniform within the zone, K_T is given by

$$K_T = \eta E^* e^T v_t h^{1/2} \qquad (1)$$

where E^* is an effective elastic constant, h is a characteristic dimension of the transformed zone, and η is a parameter (with values in the range $\sim$ 0.22 to 1) that depends on the nature of the transformation strains and the shape of the zone near the crack tip. An equivalent result has been derived from a fracture mechanics energy balance analysis. The result in Eqn. (1) can be generalized by linear superposition to include effects of nonuniform strain distributions and volume fractions within the transformation zone, which can arise from statistical distributions of M_s temperatures or subcritical transformations.

Experimental measurements indicate that transformation strains generally are nonuniform. Moreover, since v_t usually decreases monotonically with distance from the crack, the toughening is larger (by a factor of two or more) than it would be for a uniform zone with the same average transformation strain (or v_t).

In general, the shape of the frontal boundary of the transformation zone and the net transformation strain cannot be predicted *a priori*: both are affected by microstructural characteristics and autocatalytic transformation effects that vary in different systems. Observations indicate that the frontal zone boundary
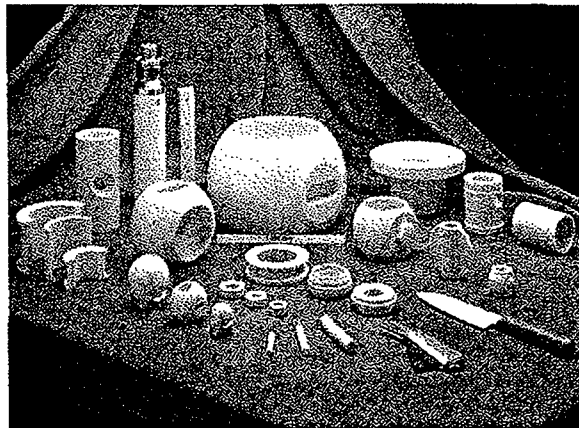
in Mg–PSZ is similar to that defined by a critical hydrostatic stress, while the net strain is close to hydrostatic dilation (i.e., shear strains relieved by twinning). In contrast, the frontal zone in Ce–TZP materials extends in a wedge shape ahead of the crack for a distance about ten times further than in Mg–PSZ.

5. Applications

Transformation-toughened zirconia has found widespread industrial application as an engineering ceramic, mostly making use of its resistance to wear, chemical inertness, low friction, high hardness and stiffness, and relatively high thermal expansion coefficient (which is closer to metals than those of most other ceramics). Applications of Mg–PSZ include: tooling for the metal forming industry (hot and cold forming dies, can-closure rollers, capstans, draw plugs, and plungers); food processing (homogenizing-pump parts); mineral, gas, and oil treatment (bearings, valves, vortex finders, orifice inserts, spigots, and spools); and the paper, chemical, and manufacturing industries (autoclave nozzles, glue transfer rollers, battery component tooling, and valves). Y–TZP is used for biological applications such as hip-ball replacements, industrial cutters, knives, and scissors, as well as golf club inserts. Zirconia-toughened alumina is used for its higher hardness and stiffness in cutting tool tips, high-performance seals and wear parts in engines, and in the mining industry. Typical components made of Mg–PSZ and Y–TZP are shown in Fig. 3.

Bibliography

Eshelby J D 1957 Determination of the elastic field of an ellipsoidal inclusion and related problems. *Proc. R. Soc. London A* **241**, 376–96

Evans A G, Cannon R M 1986 Toughening of brittle solids by martensitic transformations. *Acta Metall.* **34**, 761–800

Garvie R C, Hannink R H J, Pascoe R T 1975 "Ceramic steel?" *Nature* **258**, 703–4

Green D J, Hannink R H J, Swain M V 1989 *Transformation Toughening of Ceramics*. CRC Press, Boca Ratton, FL

Hannink R H J, Kelly P M, Muddle B C 2000 Transformation toughening in zirconia-containing ceramics. *J. Am. Ceram. Soc.* **83**, 461–87

Heuer A H, Lange F F, Swain M V, Evans A G 1986 Transformation toughening: an overview. *J. Am. Ceram. Soc.* **69**, i–iv, (entire issue devoted to papers on transformation toughening)

Kelly P M, Rose L R F 2001 The martensitic transformation in ceramics—its role in transformation toughening. *Progr. Mater. Sci.* in press

Marshall D B, Shaw M, Dauskardt R H, Ritchie R O, Heuer A H, Ready M 1990 Crack tip transformation zones in toughened zirconia. *J. Am. Ceram. Soc.* **73**, 2659–66

McMeeking R M, Evans A G 1982 Mechanics of transformation toughening in brittle materials. *J. Am. Ceram. Soc.* **65**, 242–6

Swain M V 1985 Inelastic deformation of Mg-PSZ and its significance for strength–toughness relationship of zirconia-toughened ceramics. *Acta Metall.* **33**, 2083–91

D. B. Marshall and R. H. J. Hannink

Ceramics for future power generation technology: fiber reinforced oxide composites

D.B. Marshall*, J.B. Davis

Rockwell Science Center, 1049 Camino Dos Rios, Thousand Oaks, CA 91360, USA

Abstract

Major advances have been made during the past 2 years in the development of fiber-reinforced oxide composites for long-life combustion components. These include demonstration of long-term stability of mullite-based porous-matrix composites at 1200°C, development of fiber coating and slurry infiltration methods to produce composites with weakly bonded La-monazite interphases, and development of new alumina-based fibers. © 2001 Elsevier Science Ltd. All rights reserved.

Keywords: Ceramics; Power generation technology; Fiber-reinforced oxide composites; Long-life combustion components; Alumina-based fibers; Porus matrix; Weak interface; La-monazite

1. Introduction

The need for high temperature ceramic composites for the power generation industry (both land-based and transportation) to achieve significant gains in efficiency and reductions in NO_x emissions is well established. Typical components include combustors, exhaust components, high temperature ducts, thermal insulation, heat exchangers and hot gas filters. Engine and burner rig testing during the past few years have demonstrated encouraging progress, the result of 20 years of world-wide research. However, the testing has also shown that the long-term survival of SiC-containing composites, the materials which have received the vast majority of attention to date, can be limited by recession of the matrix by volatility of SiO_2 scale in combustion environments containing water vapor [1,2], contrary to previous expectations that oxidation embrittlement would be life-limiting. The undesirable need for environmental barrier coatings to protect these composites adds motivation to develop oxide composite systems that are inherently stable in oxidizing environments.

However, oxide composites introduce a new set of limitations: their development is relatively immature, having received widespread attention only during the past 5 years; the available fibers are not as microstructurally stable or creep resistant as non-oxide fibers at high

temperatures; processing methods for infiltration of the matrix into fiber preforms have not been developed to the degree of sophistication available for chemical vapor infiltration, melt infiltration and polymer precursor infiltration of SiC; and until recently, weakly bonded interphases, a key ingredient needed for damage tolerance (cf. carbon or BN in SiC-based composites) were not available or even identified. During the period covered by this review, 1999 and 2000, key advances have been made towards overcoming each of these limitations. See Refs. [3,4,59] for reviews of developments before 1999.

Three approaches have been taken to design microstructures of oxide composites that are damage tolerant. All aim to prevent damage (cracking) in the matrix from crossing to the fibers, thereby allowing the dissipation of stress concentrations while retaining the high strengths of the fibers. Two of these are analogous to the conventional approach taken with SiC-based composites, based on fiber coatings that bond weakly, if at all, to the surface of the fibers, or coatings that are inherently weak (e.g., layered or porous). The third relies on the weakness and low stiffness of a porous matrix itself to prevent damage from extending into the fibers, even though the interface between the fibers and matrix might be strongly bonded. Tough composites that show wood-like fracture have now been demonstrated using all three approaches. The key remaining challenges are to optimize high temperature properties, demonstrate long-term stability in high-temperature combustion environments, and develop robust economical manufacturing methods.

*Corresponding author. Tel.: +1-805-373-4170.
E-mail address: dbmarsha@rsc.rockwell.com (D.B. Marshall).

2. Fiber developments

The major constraint on further development of oxide composites in the near future will be the temperature limit imposed by the microstructural stability of the fibers, both during processing of the matrix and during use. The highest performance fibers that are now available in adequate quantities and at reasonable cost are fine-grained high-purity alumina (Nextel 610™) and alumina/mullite (Nextel 720™) fibers produced by the 3M company. The creep, grain growth and strength characteristics of these fibers are now well documented [**5,6]. The Nextel 610 fibers have the higher strengths (~3.3 GPa, cf. 2.1 GPa) and are expected to be more corrosion resistant in certain environments, whereas the Nextel 720 fibers are more creep resistant and stable to higher temperatures. Based on data presently available, the anticipated maximum temperatures for extended use are about 1100°C for the Nextel 610 and 1200°C for the Nextel 720 (but dependent on stress levels and lifetimes).

A promising approach for improving the creep resistance of the alumina fibers has been exploited in a new fiber (Nextel 650™) from 3M [**7]. These fibers contain ~1% Y_2O_3 as well as ~10% ZrO_2, based on studies showing that doping of grain boundaries in bulk polycrystalline alumina with Y or La leads to large reductions in creep and grain growth [8]. Improvements were achieved in the creep resistance compared with Nextel 610™, although the creep rates remain higher than those of the mullite-containing Nextel 720™ fibers. Most of the properties of the new fibers fall between those of Nextel 610™ and Nextel 720™. Some interesting questions remain on the role of the ZrO_2 in changing the properties and in the relative amounts of Y_2O_3 in the grain boundaries and in solid solution in the ZrO_2.

Further increases in temperature capabilities of polycrystalline oxide fibers are possible with multi-phase microstructures designed to resist creep and grain growth or with other systems such as YAG. However, large increases will be difficult, for the fine grain sizes required to achieve high strengths lead to relatively rapid creep and grain growth. Laboratory-scale fabrication of polycrystalline mullite fibers with promising, but very preliminary property data have been reported [9]. Several groups are developing directionally solidified alumina/YAG eutectic fibers, which if they could be produced in small sizes and large quantities would provide very large increases in temperature capabilities and expand the options for matrix processing [10–13].

3. Weak (porous) matrix composites

The effectiveness of the porous matrix concept in allowing damage-tolerant composites without the presence of fiber coatings was previously demonstrated [14,15]. For up-to-date accounts of the design and mechanical properties of such composites see Refs. [**16,*17]. The optimum strength for the matrix in such composites involves a trade-off of properties: the matrix strength must be low enough to prevent damage in the matrix from extending into the fibers and to prevent transfer of stress between a broken fiber and its neighbors, whereas a low matrix strength leads to poor off-axis properties, compressive strength, and erosion/abrasion resistance. The major challenge is to ensure the high temperature stability of the optimum microstructure.

The earliest work on porous matrix composites used silica-based matrices [18], which place a restrictive limit on high temperature stability. Recent measurements from a composite produced by GEAE (Gen IV™), consisting of stacked layers of woven alumina fibers (Nextel 610) in an alumino-silicate matrix, indicate a significant loss in properties and embrittlement at 950°C [19]. The high temperature tensile strengths were reduced compared with room temperature values by 15 and 50% for unnotched and notched test specimens, while observations of fracture morphologies indicated a large reduction in the degree of uncorrelated fiber fracture and pullout. Significant notch sensitivity was observed even at room temperature (30% reduction in net-section strength). Large improvements were seen in another alumino-silicate matrix composite with more stable mullite fibers (Nextel 720), with no effect of notches on net section strength at temperatures up to 1100°C, and small effect at 1200°C (~20% reduction) [20]. However, under creep conditions the effect of notches was stronger (~40% reduction in net section strength at 1100°C) [21], while long-term aging at temperatures of 1100°C and above caused significant reductions in room temperature strengths (60% reduction at 1200°C) [22].

A major advance for porous matrix composites came with the development of a mullite-based matrix consisting of relatively large (~1 μm) mullite powder particles, which are resistant to sintering, forming a continuous network bonded together with smaller alumina particles (~0.2 μm), which sinter more readily [14,15]. Zirconia has also been used as the more readily sintered phase [23]. With a processing temperature (1200°C) close to the limit of the most refractory oxide fibers presently available (Nextel 720), these or related matrix compositions appear to offer the most promising prospects for long-term stability.

Recent high temperature aging experiments with a 2-D woven mullite-alumina composite (formed from multiple layers of fabric) [*24] have demonstrated that room-temperature tensile properties were not degraded after aging for 1000 h at temperatures up to 1200°C in air, as shown in Fig. 1. The 0/90° strengths and failure strains were unchanged (Fig. 1), while the ±45° strength, Young's modulus, and matrix hardness all increased after aging at the highest temperature. The increases indicate that the mullite/alumina matrix underwent some degree of sintering during the aging period. Under the same conditions, the previously mentioned alumino-silicate composites suffered strength loss of more than 60%.
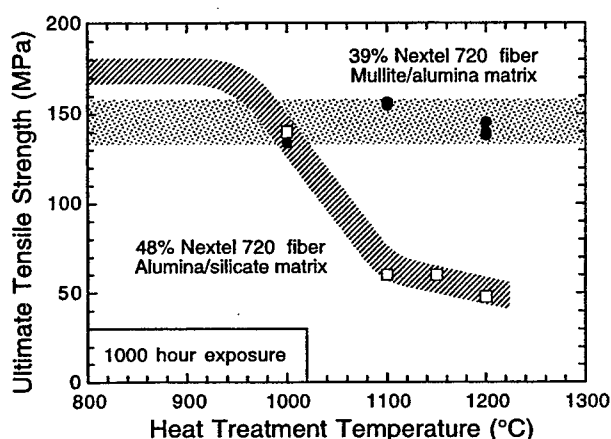
Fig. 1. Strengths of porous matrix composites after high temperature aging in air (from Ref. [**16]).

Detailed measurements are now available for the room temperature in-plane tensile properties of a 2-D composite consisting of Nextel 610 fibers (stacked layers of woven fabric) in a porous mullite-alumina matrix (both 0/90 and 45°) [**16,*25]. Measurements of notch sensitivity using center-hole tension tests indicate some loss of net-section strength in the presence of notches, but much less than for a fully notch-sensitive material. Effects of hole size on strength were rationalized by comparing with stress distributions predicted using non-linear continuum and shear band models: a size-scale dependence in the failure condition is implied. The trends are similar to those observed in conventional weak-interface composites.

Systematic studies have now been done to vary the strength and density of the matrix of the mullite-based composite and measure the effect on the mechanical properties [*17,*26]. These involved further processing with multiple cycles of reinfiltration and heat treatment using an alumina precursor ($Al_2(OH)_5Cl$). Bonding of the particle network by evaporation–condensation in reactive atmosphere has also been used to strengthen the matrix without decreasing the porosity [23]. As the matrix was strengthened and densified there was a trend to increase the tensile strength in the ±45° direction, decrease the strength in the 0/90° direction, and decrease the degree of uncorrelated fiber fracture and pullout lengths on the fracture surface.

4. Weak interface developments

Since the discovery that rare-earth phosphates (most notably La-monazite) bond sufficiently weakly with other oxides to allow debonding of fibers [27], other mixed oxide compounds have been proposed and tested for the same purpose (tungstates, vanadates, niobates [9,28,29]). Nevertheless, La-monazite, which is the most refractory of

all the proposed compounds, has attracted the most attention.

Further studies of debonding and sliding at the $LaPO_4$–Al_2O_3 interface have confirmed the weak bonding [30,*31], but have also indicated a possibly important role of plastic deformation in the monazite itself to accommodate interfacial roughness [*31]. Both La-monazite and $CaWO_4$ (scheelite) have been shown to deform relatively easily at room temperature by twinning and dislocation motion [*32]. Connections may exist between this and the unique resistance of monazite to amorphizaton from radiation damage, which makes it the prime candidate for long-term storage of actinide wastes [33].

The effectiveness of monazite interface coatings in providing a phase-compatible debond layer has now been confirmed from tensile strength testing in a variety of specimen configurations (using uncoated control specimens for comparisons): coatings and coating/matrix combinations on individual sapphire fibers [*31,34]; individual tows of Nextel 610 alumina fibers coated with monazite and infiltrated with alumina matrix [35]; and unidirectional composites of Nextel™ fibers (610, 650 and 720) with monazite coatings and alumina matrix [**36]. In the last case the matrix, although porous, was sufficiently strong that very little fragmentation of the matrix took place during fracture. Clear evidence was found on the fracture surfaces for the role of the weak interface rather than a weak matrix in allowing extensive debonding and pullout of fibers. After heat treatment at 1100 and 1200°C, the strengths of composites with monazite coatings were all higher than those of the corresponding control specimens, the largest differences being seen after 1200°C treatment (e.g., strength of 200 MPa for coated Nextel 610 composite after 5 h at 1200°C compared with 45 MPa for uncoated control composite).

Although an effective method has been developed for producing thin coatings of monazite on fiber tows (see Section 6), a method for coating fibers in a woven fabric has not been demonstrated. An approach that circumvents the need for a separate coating step has been developed on the basis of observations that monazite deposits preferentially between adjacent fibers in tows or fabrics after infiltration with solution precursors and heat treatment [*37]. Infiltration of a slurry consisting of alumina powder in a solution precursor for monazite results in a two-phase (porous) matrix of alumina and monazite, with a continuous layer of monazite around all of the fibers. Composites formed by infiltrating fabrics of Nextel 610 and 720 in this manner, followed by stacking, pressing and sintering, have shown damage-tolerant behavior and absence of notch sensitivity when tested at room temperature and at 1000°C (Fig. 2) [*37–39]. Although this behavior may be partly due to the porous nature of the matrix, a significant difference in notch sensitivity is seen between this and the porous matrix composites described in the previous section, thus implying an additional effect of the weak interface.
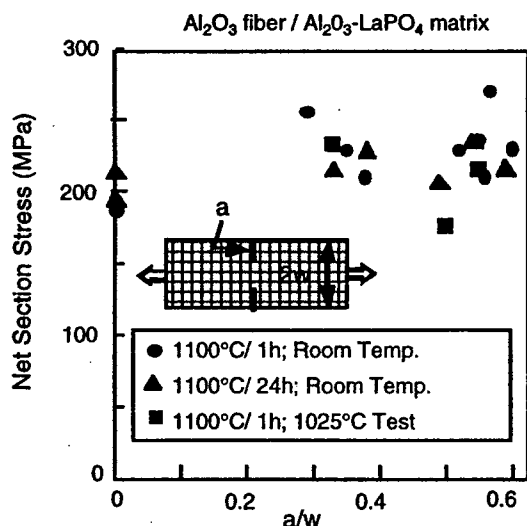
Fig. 2. Effect of notch depth and heat-treatment conditions on net-section strengths measured at room temperature and at 1025°C. Monazite/alumina matrix, Nextel™ 610 fibers. Specimen width: w=13 mm.

Several studies have shown that infiltration of Nextel fiber tows and fabrics with solution precursors, followed by heat treatment to form monazite, often leads to strength degradation [40–**44]. Many combinations of precursor chemistry, fiber composition, temperature, and time have been assessed, with strength measurements being obtained both from individual fibers with thin monazite coatings of ~100 nm thickness (see Section 6 for coating method) [**42–**44] and from infiltrated fiber tows that form mini-composites [40,**41]. Although the detailed mechanisms of degradation in most cases are not known, it is clear that the mechanisms involve the precursor chemistry rather than the monazite itself, since degradation does not occur with coatings formed from aqueous slurries of rhabdophane particles (hydrated monazite) and in minicomposites formed by infiltration with slurries of monazite particles. Indeed, in these cases the strengths after heat treatment are often higher than strengths of uncoated control specimens. Strength loss is also avoided in some cases when fiber tows are infiltrated with slurries consisting of alumina particles in solution precursors as described above, possibly a result of the alumina acting as an internal buffer. Many observations are consistent with a hypothesis that trapped gases remaining from the precursors can build up high pressures in dense coatings during heat treatment and react with the fiber surface [**44].

5. Layered and porous interphases

Some of the earliest attempts to produce damage-tolerant oxide composites were based on forming weak fiber coatings, either by the introduction of porosity or by use of layered crystal structures such as β-alumina/magneto-

plumbites with intrinsically weak cleavage planes, analogous to mica. These approaches have not proven as effective as either the porous matrix approach or the weakly bonded interface materials described in the previous sections [34]. Nevertheless, some useful progress has been made in demonstrating composite properties, refining coating methods, and in defining the relative merits of porosity being concentrated at an interface or distributed throughout the matrix.

Porous interphases are most commonly produced by mixing fugitive carbon with the fiber coating material. Zirconia, rare-earth aluminates, and zircon have been investigated recently [*45–48]. Composites have been produced by hot pressing sapphire fibers with porous zirconia coatings in an alumina matrix [*45,46]. Although the composites had relatively low strengths (~100–130 MPa for 0/90 cross-ply), they were not degraded after cycling at 1200°C (>1300 cycles) and aging at temperatures that would severely degrade composites with polycrystalline oxide fibers (100 h at 1400°C).

Several groups have produced composites with a thin continuous gap between the fibers and matrix by using a fugitive carbon coating on the fibers [*49–52]. Useful insight into the merit of the approach is provided in Ref. [*49], where comparisons with uncoated control specimens indicated that the gap was effective in enabling fiber pullout in composites of Nextel 720 fibers in a dense calcium alumino-silicate (CAS) matrix, whereas the gap had no effect in a composite with a porous matrix of mullite-alumina. Although the starting strengths were low in this study (~130 MPa), there was no degradation in the porous matrix composite after 500 h at 1150°C and a small loss (~20%) in the CAS matrix composite after aging for 500 h at 1000°C.

The use of layered crystal structures presents several challenges: (i) to form the desired phase at a sufficiently low temperature that the fibers are not degraded during processing; (ii) to orient the weak basal planes of the crystals parallel to the fiber surface; and (iii) to control the roughness of the fracture in the coating to allow constrained sliding of the fibers. Progress has been made in lowering the formation temperature for refractory hexaluminates as low as 1000°C using sol–gel and doping techniques [*53–57]. However, although textured coatings have been grown on single-crystal YAG plates at 1200°C, there is a suggestion that on polycrystalline alumina fibers (Nextel 610) there may not be an adequate driving force for grain growth and texturing at this temperature (which is the limit to which these fibers may be exposed during processing) [*53].

6. Fiber coating methods

Although chemical and physical vapor methods have been used to deposit coatings of monazites and hexaluminates [29], the deposition of stoichiometric multicom-

ponent oxide coatings by such methods is difficult. Solution precursor, sol–gel, or slurry methods potentially allow better control of stoichiometry, although it is more difficult to obtain uniform bridge-free coatings on individual fibers in tows or woven preforms.

A technique that minimizes the bridging problem involves passing the fiber tows through a coating solution or slurry covered with a layer of immiscible liquid that displaces excess coating solution from between the fibers as they are withdrawn [58]. This method has proven effective for depositing thin coatings of monazite (~50–100 nm thickness) on Nextel 610 and 720 fiber tows using a variety of different solution precursors and slurries [**42–**44]. It has also been used to deposit porous coatings using a fugitive carbon phase (La-hexaluminate, YAG and zircon) [47,48].

7. Matrix processing methods

The composites described above were processed using a variety of liquid-based infiltration methods (slurry, sol–gel, precursor) to infiltrate the matrix material into fiber tows or woven fabrics at, or near room temperature, followed by sintering to strengthen the matrix. A challenge remains to develop more versatile methods capable of infiltrating high volume fractions of matrix into fiber preforms. An innovative method was described in Ref. [23] for producing tapes with very high particle packing and shear thinning characteristics that allow infiltration by simple stacking of fabrics and tapes followed by application of shear displacements by vibration.

8. Conclusions

Several types of oxide composite now appear capable of providing sustained use at temperatures as high as 1200°C. While considerable testing in combustion environments with realistic gas flow rates and compositions is still needed to prove their viability, and further improvements in properties and processing methods are desirable, there is now an opportunity to explore innovative combustion component designs that avoid limitations of metallic systems. Applications of monazite-based composites in thermal protection systems for space re-entry vehicles are already progressing rapidly in this direction [**41]. Sub-component testing in wind tunnel, arc jet, and impact environments at temperatures up to 1300°C, have shown large gains compared with conventional silica-based systems.

Acknowledgements

References

Papers of particular interest, published within the annual period of review, have been highlighted as:
* of special interest;
** of outstanding interest.

[1] Robinson RC, Smialek JL. SiC recession caused by SiO$_2$ scale volatility under combustion conditions: I. Experimental results and empirical model. J Am Ceram Soc 1999;82:1817–25.

[2] Opila EJ, Smialek JL, Robinson RC, Fox DS, Jacobson NS. SiC recession caused by SiO$_2$ scale volatility under combustion conditions: II. Thermodynamics and gaseous diffusion model. J Am Ceram Soc 1999;82:1826–34.

[3] Cox BN, Zok FW. Advances in ceramic composites reinforced by continuous fibers. Curr Opin Solid State Mater Sci 1996;1:666–73.

[4] Evans AG, Marshall DB, Zok F, Levi C. Recent advances in oxide-oxide composite technology. Adv Composite Mater 1999;8:17–23.

[**5] Hay RS, Boakeye E, Petry MD, Berta Y, Von Lehmden K, Welch J. Grain growth and tensile strength of 3-M Nextel 720TM after thermal exposure. Ceram Eng Sci Proc 1999;20:165–72, Tensile strength and grain growth of 3M Nextel 720™ fibers measured after heat-treatment from 1000 to 1500°C for 20 min to 300 h. Possible mechanisms for strength degradation are discussed.

[6] Petry MD, Mah T. Effect of thermal exposures on the strengths of Nextel 550 and 720 filaments. J Am Ceram Soc 1999;82:2801–7, More strength and grain growth data for Nextel 720 and Nextel 550 as a function of aging temperature and environment, with and without carbon coatings.

[**7] Wilson DM, Visser LR. Nextel 650 ceramic oxide fiber. New alumina-based fiber for high temperature composite reinforcement. Ceram Eng Sci Proc 2000;21:363–73, Properties of new polycrystalline alumina fiber doped with Y$_2$O$_3$ and ZrO$_2$ to improve microstructural stability and creep resistance.

[8] Bruley J, Cho J, Chan HM, Harmer MP, Rickman JM. Scanning transmission electron microscopy analysis of grain boundaries in creep-resistant yttrium- and lanthanum-doped alumina microstructures. J Am Ceram Soc 1999;81:2865–70.

[9] Lewis MH, York S, Freeman C, Alexander IC, Al-Dawery I, butler EG, Doleman PA. Oxide CMCs, novel fibres, coatings and fabrication procedures. Ceram Eng Sci Proc 2000;21:535–47, Laboratory scale polycrystalline mullite fibers with very preliminary property measurement. Compatibility tests of LaPO$_4$, NdPO$_4$ and LaVO$_4$ interphases.

[10] Mah TI, Parthasarathy TA, Kerans RJ. Processing, microstructure, and strength of Alumina-YAG eutectic polycrystals. J Am Ceram Soc 2000;83:2088–90.

[11] Sayir A. editor, Directional Solidification of eutectic ceramics. In: Pechenik A, Kalia RK, Vashita P, editors. Computer Aided Design of High-Temperature Materials, New York: Oxford University Press, 1999: 197–211.

[12] Yoshikawa A, Epelbaum BM, Fukuda T, Suzuki K, Waku Y. Growth of Al2O3/Y3Al5O12 eutectic fiber by micro-pulling-down method and its high temperature strength and thermal stability. Jpn J Appl Phys 1999;38:L55–8.

[13] Yoshikawa A, Hasegawa K, Fukuda T, Suzuki K, Waku Y. Growth and diameter control of Al2O31Y3Al5O12 eutectic fiber by micro-pulling-down method and its high temperature strength and thermal stability. Ceram Eng Sci Proc 1999;20:275–82.

[14] Lange FF, Tu W-C, Evans AG. Processing of damage-tolerant, oxidation-resistant ceramic-matrix composites by a precursor infiltration and pyrolysis method. Mater Sci Eng 1995;A195:145–50.

[15] Levi CG, Yang JY, Dalgleish BJ, Zok FW, Evans AG. Processing

and performance of an all-oxide ceramic composite. J Am Ceram Soc 1998;81:2077–86.

[**16] Zok FW, Levi CG. Mechanical properties of porous-matrix composites. Adv Eng Mater 2001;3:15–23, Review of porous matrix composites, covering mechanics considerations in the design of the composite microstructures, a survey of mechanical properties under tensile loading in various directions as well as in the presence of notches and holes, and assessment of prospects for long-term stability.

[*17] Levi CG, Zok FW, Yang JY, Mattoni M, Lofvander JPA. Microstructural design of stable porous matrices for all-oxide ceramic composite. Z Metallkde 1999;90:1037–47, The principles guiding the microstructural design of porous matrix composites using two particulate oxide constituents, in different size scales and with distinctly different sintering kinetics are are reviewed. The effects of multiple reinfiltration with an alumina precursor ($Al_2(OH)_5Cl$) on microstructure and tensile properties are described.

[18] Harrison MG, Millard ML, Szweda A. Fiber Reinforced Ceramic Matrix Composite Member and method for Making. US Patent No. 5 306 554; UK Patent No. 2 230 259 (1994).

[19] Kramb VA, John R, Zawada LP. Notched fracture behavior of an oxide/oxide ceramic-matrix composite. J Am Ceram Soc 1999;82:3087–96, Tensile test data from Gen IV (N610) at room temperature and 950°C: shows some notch sensitivity at RT (66% net section strength) and large notch sensitivity at 950°C (30% net section strength). Observations of damage from fracture surfaces and polished sections indicate embrittlement at 950°C.

[20] Buchanan DJ, John R, Zawada LP. Notched fracture behavior of oxide-oxide Nextel 720/AS composite. Ceram Eng Sci Proc 2000;21:567–74, Tensile test data showing no effect of notches on net section strength of Nextel 710/alumino-silicate matrix composite at temperatures up to 1100°C, and small effect at 1200°C (~20% reduction).

[21] John R, Buchanan DJ, Zawada LP. Creep deformation and rupture behavior of a notched oxide-oxide Nextel 720/AS composite. Ceram Eng Sci Proc 2000;21:567–74, Tensile creep data from the same composites as in Ref. [20].

[22] Jurf RA, Butner SC. Advances in oxide-oxide CMC. J Eng Gas Turbines Power 2000;122:202–5, Tensile strengths of Nextel 710/alumino-silicate matrix composite after long-term aging at temperatures up to 1200°C.

[23] Haslam JJ, Berroth KE, Lange FF. Processing and properties of an all-oxide composite with a porous matrix. J Eur Ceram Soc 2000;20:607–18, Formation of mullite-zirconia matrix composite using a vibro-impregnation process with tape freezing followed by sintering without shrinkage in a reactive atmosphere.

[*24] Carelli E, Fujita H, Yang J, Zok FW. On the mechanical properties of a porous-matrix ceramic composite following thermal aging, J. Am. Ceram. Soc. (in press). Effect of long-term aging at temperatures up to 1200°C on properties of Nextel 720/mullite-alumina matrix composite.

[*25] Heathcote JA, Gong XY, Yang JY, Ramamurty U, Zok FW. In-plane mechanical properties of an all-oxide ceramic composite. J Am Ceram Soc 1999;82:2721–30, Detailed measurements of room temperature tensile properties of 2-D composite consisting of Nextel 610 fibers in porous mullite-alumina matrix (both 0/90 and 45°). Notch sensitivity is assessed using center-hole tension tests: some loss of strength is observed in the presence of notches, but much less than for a fully notch sensitive material. Effects of hole size on strength were rationalized by comparing with stress distributions predicted using non-linear continuum and shear band models.

[*26] Mattoni M, Yang JY, Levi CG, Zok FW. Effects of a precursor-derived alumina on the mechanical properties of a porous-matrix, all-oxide ceramic composite, Mater. Sci. Eng. (2000) in press. Measurements of changes in properties of porous matrix compo-

site (mullite alumina) with systematically varied density and strength of the matrix.

[27] Morgan PED, Marshall DB. Ceramic composites of monazite and alumina. J Am Ceram Soc 1995;78:1553–63.

[28] Goettler RW, Sambasivan S, Dravid V, Kim S. Interfaces in oxide fiber — oxide matrix ceramic composites. In: Pechenik A, Kalia RH, Vashita P, eds. Computer Aided Design of High-Temperature Materials, New York: Oxford University Press, 1999: 333–349. $CaWO_4$ & $ErTaO_4$ interphases: strengths of Scheelite-coated N6100 fibers after 1100°C/1 h — no strength loss. However strength loss in composites made with Al_2O_3 polymer

[29] Lewis MH, Tye A, Butler EG, Doleman PA. Oxide CMCs: interphase synthesis and novel fibre development. J Eur Ceram Soc 2000;20:639–44, Deposition of rare-earth vanadates and phosphates from colloidal precursors or by magnetron sputtering. Thermal stability with reference to potential fibres and matrices.

[30] Marshall DB, Waldrop JR, Morgan PED. Thermal grooving at the interface between alumina and monazite. Acta Mater 2000;48:4471–4, Atomic force microscopy of monazite alumina interface fracture surfaces.

[*31] Marshall DB, Davis JB, Morgan PED, Waldrop JR, Porter JP. Properties of La-monazite as an interphase in oxide composites. Z Metallkde 1999;90:1048–52, Room temperature deformation of monazite at rough sliding interfaces.

[*32] Hay RS. Monazite and scheelite deformation mechanisms. Ceram Eng Sci Proc 2000;21:203–28, TEM observations showing dislocations and twins in materials deformed at room temperature.

[33] Meldrum A, Boatner LA, Ewing RC. A comparison of radiation effects in crystalline ABO_4-type phosphates and silicates. Mineral Mag 2000;64:185–94, Radiation damage was monitored as a function of temperature in situ in a transmission electron microscope. The critical temperature, above which the recrystallization processes are faster than damage accumulation and amorphization cannot be induced, was only 35°C for $LaPO_4$, much lower than for other phosphates and silicates.

[34] Parthasarathy TA, Boakeye E, Cinibulk MK, Perry MD. Fabrication and testing of oxide/oxide microcomposites with monazite and hibonite as interlayers. J Am Ceram Soc 1999;82:3575–83, Strengths of single fiber composites: sapphire+$LaPO_4$+10 μm Al_2O_3 Also hibonite ($CaAl_{12}O_{19}$).

[35] Keller KA, Mah T-I, Boakye EE, Parthasarathy TA. Gel-casting and reaction bonding of oxide-oxide minicomposites with monazite interphase. Ceram Eng Sci Proc 2000;21:525–34.

[**36] Keller KA, Mah T, Parthasarathy TA, Boakye EE, Cinibulk M. Evaluation of all-oxide composites based on coated Nextel 610 and 650 fibers. Ceramic Engineering and Science Proceedings 2001, in press. Unidirectional composites of Nextel™ fibers (610, 650 and 720) with monazite coatings and alumina matrix: after heat treatments at 1100 and 1200°C, the strengths of composites with monazite coatings were all higher than those of the corresponding control specimens, the largest differences being seen after 1200°C treatment (e.g., 200 MPa for coated Nextel 610 composite after 5 h at 1200°C, 45 MPa for uncoated control composite).

[*37] Davis JB, Marshall DB, Morgan PED. Monazite containing oxide-oxide composites. J Eur Ceram Soc 2000;20:583–7, Properties of composite formed by infiltrating Nextel™ 610 fiber preform with slurry of alumina in solution precursor for monazite.

[*38] Davis JB, Marshall DB, Morgan PED. Oxide composites of Al_2O_3 and $LaPO_4$. J Eur Ceram Soc 1999;19:2421–6, Fracture observations from composite formed by infiltrating NextelTM 610 fiber preform with slurry of alumina in solution precursor for monazite and from composite with sapphire fibers and fully dense monazite matrix.

[39] Morgan PED, Marshall DB, Davis JB, Housley RM. The weak interface between monazites and refractory ceramic oxides. In: Pechenik A, Kalia RK Vashishta P, eds. Computer Aided Design

of High-Temperature Materials, New York: Oxford University Press, 1999: 229–243.

[40] Davis JB, Marshall DB, Oka KS, Housley RH, Morgan PED. Ceramic composites for thermal protection systems. Composites: Part A 1999;30:483–8.

[**41] Davis JB, Marshall DB, Morgan PED, Oka KS, Barney AO, Hogenson PA. Damage tolerant thermal protection systems, in: Proc Space 2000, American Institute of Aeronautics and Astronautics, Long Beach, CA, 2000. Infiltration and heat treatment of fiber tows and fabrics with monazite slurries and solution precursors. Strength degradation observed for solution precursors. Highest strengths were achieved by infiltration with aqueous slurries of monazite powder, giving composites with a porous monazite matrix. Retained strengths higher than uncoated control specimen

[**42] Boakye E, Hay RS, Petry MD. Continuous coating of oxide fiber tows using liquid precursors: monazite coatings on Nextel 720. J Am Ceram Soc 1999;82:2321–31, Seven different aqueous or ethanolic precursors were used to coat monazite on Nextel 720 fiber tows using the immiscible liquid displacement method to minimize bridging of coating between filaments. Coatings were cured in-line at 1200–1400°C. Tensile strengths measured from individual coated fibers showed significant degradation.

[*43] Hay RS, Boakye E, Petry MD. Effect of coating deposition temperature on monazite coated fiber. J Eur Ceram Soc 2000;20:589–97, Further studies as in previous reference and microstructural analysis. Tensile strengths of coated fibers decreased with increasing deposition temperature and with time at temperature after deposition. Possible reasons for the strength decrease are discussed.

[**44] Boakye EE, Petry MD, Hay RS, Douglas LM. Monazite coatings on Nextel 720, 610, and Tyranno-SA fibert tows: effects of precursors on fiber strength. Ceram Eng Sci Proc 2000;21:229–36, Further studies as in previous two references, with three different precursors and curing in-line at temperatures between 900 and 1300°C. Fibers with coatings formed from colloidal rhabdophane particles showed higher strengths than uncoated fibers after 100 h at 1200°C. Discussion of potential effects of gaseous species and coating porosity.

[*45] Holmquist M, Lundberg R, Sudre O, Razzell AG, Molliex L, Benoit J, Adlerborn J. Alumina/alumina composite with a porous zirconia interphase — processing, properties and component testing. J Eur Ceram Soc 2000;20:599–606, Composite consisting of sapphire fibers with porous zirconia coating in an alumina matrix. Moderate strength (100–130 MPa), but retained composite properties at high temperatures and after aging (1000 h at 1400°C). Combustor tiles were manufactured and successfully tested in a rig at temperatures>1260°C and up to 46 cycles.

[46] Holmquist M, Adlerborn J, Razzell T, Sudre O, Molliex L. Processing and properties of oxide matrix/oxide fibre composite. Br Ceram Trans 2000;99:266–9.

[47] Cinibulk MK, Parthasarathy TA, Keller KA, Mah T-I. Porous rare-earth aluminate fiber coatings for oxide-oxide composites. Ceram Eng Sci Proc 2000;21:219–28, Strengths of tows and minicomposites with porous coatings of La-hexaluminate and

YAG with fugitive carbon phase and with black glass matrix. La-hexaluminate coatings degrade tow strengths (40%) but help protect the fibers from reaction with the matrix. YAG coatings did not degrade the tow strengths.

[48] Boakye E, Hay RS, Petry MD, Parthasarathy TA. Sol–gel synthesis of zircon-carbon precursors and coatings of Nextel 720TM fiber tows. Ceram Eng Sci Proc 1999;20:165–72, A zircon–carbon precursor was continuously coated on Nextel 720TM fibers using a sol–gel method. Zircon formation was retarded by the presence of carbon.

[*49] Keller KA, Mah TI, Parthasarathy TA et al. Fugitive interfacial carbon coatings for oxide/oxide composites. J Am Ceram Soc 2000;83:329–36, Comparison of effect of interface gap in composites with dense and porous matrices.

[50] Peters PWM, Daniels B, Clemens F et al. Mechanical characterisation of mullite-based ceramic matrix composites at test temperatures up to 1200°C. J Eur Ceram Soc 2000;20:531–5, Nextel 610 fibre-reinforced mullite-based matrix with a 0.1-μm thick carbon coating on fibers. Tensile strength decreased rapidly at temperatures above 800°C.

[51] Halverson HG, Curtin WA. Stress-rupture of Nextel 610/alumina yttria composites. Ceram Eng Sci Proc 2000;21:559–66, HT strength, stress-rupture, and creep of composite with porous matrix/interface: large decreases in rupture stress at 1050°C.

[52] Mackin TJ, Roberts MC. Evaluation of damage evolution in ceramic-matrix composites using thermoelastic stress analysis. J Am Ceram Soc 2000;83:337–43, Thermoelastic stress analysis from several composites, including Al_2O_3/Al_2O_3 (c-coating on fibers). The Al_2O_3/Al_2O_3 composite showed notch insensitivity similar to other composites.

[*53] Cinibulk MK. Hexaluminates as a cleavable fiber-matrix interphase: synthesis, texture development, and phase compatibility. J Eur Cer Soc 2000;20:569–82, Review of current state of research on hexaluminates as a potential cleavable oxide fiber-matrix interphase.

[54] Cinibulk MK. Effect of divalent cations on the synthesis of citrate-gel-derived lanthanum hexaluminate powders and films. J Mater Res 1999;14:3581–93, Achieved improved [0001] texture of thin films. However, degree of basal texture achieved at sufficiently low temp to coat polycrystalline fibers is very low.

[55] Callender RL, Barron AR. Facile synthesis of aluminum containing mixed metal oxides using doped carboxylate-alumoxane nanoparticles. J Am Ceram Soc 2000;83:1777–89.

[56] Callender RL, Barron AR. A new route to hexaluminate ceramics via a novel transmetalation reaction. Ceram Eng Sci Proc 1999;20:27–34.

[57] Saruhan B, Schneider H, Komarneni S, Abothu IR. Electrostatically deposited surface seeding and promotion of crystallization of sol–gel derived La Al11O18 coating on oxide fibers. J Eur Ceram Soc 1999;19:2427–35.

[58] Hay RS, Hermes EE. Sol–gel coatings on continuous ceramic fibers. Ceram Eng Sci Proc 1990;11:1526–38.

[59] Kerans RJ, Hay RS. Parthasarathy TA. Structural ceramic composites. Current Opinion in Solid State & Materials Science 1999;4:445–51.